

Electron Localization and Dynamics
in $\text{Ln} - \text{LnX}_3$ and $\text{LnX}_2 - \text{LnX}_3 - \text{AX}$ Melts :
An Optical Reflectivity, Absorption and ESR Study
(Ln: Ce, Nd, Eu; X: Cl, I; A: alkali metal)

Zur Erlangung des akademischen Grades eines
DOKTORS DER NATURWISSENSCHAFTEN

(Dr. rer. nat.)

von der Fakultät für Chemie

der

Universität Karlsruhe (TH)

angenommene

DISSERTATION

von

M.Sc. Osamu Terakado

aus Ibaraki, Japan

Dekan: Prof. Dr. M. Metzler

1. Gutachter: Prof. Dr. W. Freyland

2. Gutachter: Prof. Dr. M. Kappes

Tag der mündlichen Prüfung: 12. Juli 2002

Contents

Abstract, Zusammenfassung	1
1. Introduction	5
2. Some basic spectroscopic concepts and properties of the present systems	11
2.1 Optical properties of light absorbing media	11
2.1.1 Absorption and reflection of light	11
2.1.2 Lorentz oscillator model and Drude model for free charge in metal	13
2.1.3 Oscillator strength	14
2.2 Electron Spin Resonance	14
2.2.1 Zeeman effect and Bloch equations	15
2.2.2 Spin Hamiltonian	16
2.3 Electronic transitions and optical properties of rare earth ions	18
2.3.1 Intra 4f transitions	18
2.3.2 Nephelauxetic effect	19
2.3.3 Hypersensitive transitions	19
2.3.4 Theoretical treatment of f-f transition intensities, Judd-Ofelt theory	20
2.3.5 f-d transitions	21
2.3.6 Charge transfer bands	22
2.4 Classical Classification of mixed valence solid compounds	22
3. Experimental section	25
3.1 Preparation of chemicals	25
3.1.1 General remarks on chemical reactivity of the present systems	25
3.1.2 Preparation of rare earth metal and rare earth halides	25
3.1.3 Recrystallisation of alkali halides	27
3.1.4 Preparation of $\text{LnX}_2\text{-LnX}_3 - (\text{LiX-KX})_{\text{eut}}$ mixtures	27
3.2 Spectroscopic techniques	28
3.2.1 UV-VIS Spectrometer	28
3.2.2 High temperature reflectivity set-up	28

3.2.3 Optical absorption cell	31
3.2.4 High temperature ESR set-up	32
3.3 Experimental procedures	34
3.3.1 Reflectivity measurement	34
3.3.2 Absorption measurement	35
3.3.3 ESR measurement	36
4. Experimental details and problems, Data Analysis and Error Discussion	37
4.1 Reflectivity measurements	37
4.1.1 Evaluation of apparent reflectivity	37
4.1.2 Experimental problems and principal restrictions	40
4.1.2.1 Film formation	41
4.1.2.2 Analysis of film spectra	44
4.1.2.3 Metal dissolution in rare earth halide – alkali halide mixtures	46
4.2 Absorption measurements	48
4.2.1 Analysis of absorption measurements	48
4.2.2 Experimental problems in absorption measurements of $\text{LnX}_2\text{-LnX}_3\text{-}(\text{LiX-KX})_{\text{eut}}$ melts	49
4.3. Error analysis of optical measurements	50
4.3.1 Instrumental error sources	50
4.3.2 Error in absorption measurements	51
4.3.3 Error in reflectivity measurements	52
4.4 ESR measurements	53
5 Results	55
5.1 Reflectivity measurements	55
5.1.1 $\text{Nd}_x(\text{NdCl}_3)_{1-x}$ melts	56
5.1.2 $\text{Ce}_x(\text{CeCl}_3)_y\text{-}(\text{LiCl-KCl})_{\text{eut}, 1-x-y}$ melts	57
5.2 Absorption measurements of $(\text{LnCl}_2)_x(\text{LnCl}_3)_y\text{-}(\text{LiCl-KCl})_{\text{eut}, 1-x-y}$ melts	58
5.2.1 $(\text{NdCl}_2)_x(\text{NdCl}_3)_y\text{-}(\text{LiCl-KCl})_{\text{eut}, 1-x-y}$ melts	58
5.2.2 $(\text{EuCl}_2)_x(\text{EuCl}_3)_y\text{-}(\text{LiCl-KCl})_{\text{eut}, 1-x-y}$ melts	61
5.3 Absorption measurements of $(\text{LnI}_2)_x(\text{LnI}_3)_y\text{-}(\text{LiI-KI})_{\text{eut}, 1-x-y}$ melts	62

5.4 Absorption measurements of $(\text{LnI}_2)_x(\text{LnI}_3)_{1-x}$ melts	64
5.4.1 $(\text{NdI}_2)_x(\text{NdI}_3)_{1-x}$ melts	65
5.4.2 $(\text{CeI}_2)_x(\text{CeI}_3)_{1-x}$ melts	68
5.5 ESR measurement of a $(\text{NdCl}_2)_{0.02}(\text{NdCl}_3)_{0.02}-(\text{LiCl-KCl})_{\text{eut}, 0.96}$ melt	71
6 Discussion	75
6.1 Microscopic structure of LnX_3 , LnX_2 and $\text{LnX}_3\text{-MX}$ solids and melts	76
6.2 Optical absorption in pure rare earth metal trihalides	79
6.2.1 Electronic structure of ionic liquids and Charge transfer band	79
6.2.2 Intra 4f transition	83
6.3 Electron localization and VIS-IR spectra in M-MX and Ln-LnX ₃ melts	84
6.3.1 F-center and Mollwo Ivey rule	84
6.3.2 F-centers in $(\text{CeI}_2)_x(\text{CeI}_3)_{1-x}$ melts?	86
6.3.3 Optical properties of the Nd and Eu systems	86
6.3.3.1 Interpretation of optical spectra of $(\text{NdI}_2)_x(\text{NdI}_3)_{1-x}$ mixtures	87
6.3.3.2 Two-site Small Polaron Model	89
6.3.3.3 Optical properties of small polaron model	91
6.3.3.4 Analysis of absorption spectra of $(\text{NdI}_2)_x(\text{NdI}_3)_{1-x}$ melts	92
6.3.3.5 Hypersensitive transition and spectral change in NdI_2 containing melts	94
6.3.3.6 Comparison with the neodymium chloride systems and the role of eutectic melt	95
6.3.3.7 Europium chloride melts	96
6.4 Intervalence charge transfer and electron dynamics	97
6.4.1 Hopping conduction and Electronic mobility	97
6.4.2 ESR relaxation time in $(\text{NdCl}_2)_x(\text{NdCl}_3)_y-(\text{LiCl-KCl})_{\text{eut}, 1-x-y}$ melts	99
Appendix	102
Appendix 1. Phase diagrams and literature data of selected compounds	102
Appendix 2. Optical absorption study of InCl_x melts	107
Manufacturer list	111

References **112**

Abstract

In the present work optical absorption, reflectivity and ESR measurements have been performed for rare earth metal - rare earth metal halide ($\text{Ln} - \text{LnX}_3$) melts and their mixtures with alkali halide eutectic melts at high temperature. One of the main difficulties in the spectroscopic experiments was that the construction of proper cells was strongly limited due to the extremely corrosive properties and oxygen sensitivity of these melts at high temperature. For the reflectivity measurements a special vacuum tight cell has been developed which consists of melt reservoir from molybdenum and a quartz window not in contact with the melt. However, difficulties arose from transport reactions through the vapour phase. Absorption and ESR measurements have been carried out for the less corrosive mixtures in alkali halide and rare earth iodide melts with equipment which had been developed for the high temperature measurements of alkali – alkali halide melts (M-MX). The ESR cell was modified to allow the measurements for the rare earth halide melts.

The main focus in this study is to investigate for the first time spectroscopically the different electronic transport properties within the series of the fluid $\text{Ln} - \text{LnX}_3$ systems. The electrical conductivity of the lighter rare earth elements, La or Ce, increases monotonously with increasing metal concentration, similar to the M-MX melts, while the heavier metal systems like Nd have non-metallic character for all metal concentrations. In the former case electron localization similar to the F-centers in M-MX systems is suspected. On the other hand, as supposed in the literature, the electronic transport in the neodymium systems can be explained by an intervalence charge transfer (IVCT) or electron hopping between two different oxidation states, which can be regarded as “subhalide” system. Further evidence from spectroscopic studies has not been reported so far.

The essential results of the present study can be summarised as follows:

- In Ce - systems no evidence of the formation of F-center like electronic defects has been found through optical and ESR measurements up to the concentration of $(\text{CeI}_2)_{0.24}(\text{CeI}_3)_{0.76}$.
- The optical spectra of $\text{NdI}_2 - \text{NdI}_3$ as well as $\text{Nd} - \text{NdCl}_3$ melts are characterised by a broad absorption band (~ 1 eV) around 1.6 eV and 1.5 eV, respectively, which shows characteristic features of IVCT bands. In eutectic MX melts the excitation between Nd^{2+} and Nd^{3+} states

shifts to ~ 2.5 eV which is presumably due to the weak complex formation of mixed valent ions.

- Through the fitting of optical spectra with a simple two-site model for the polaron hopping the activation energy ($E_A \sim 0.4$ eV) and the electronic conductivity ($\sigma_h \sim 1 \Omega^{-1} \text{ cm}^{-1}$) are determined. These values are in good agreement with the results of the recent electrical conductivity measurement within the experimental errors.
- ESR spectra of mixed valent neodymium chlorides in eutectic alkali halide melts have been measured at different temperatures up to 420 °C. They are characterised by a broad band with max. 10^3 Gauss. The correlation time evaluated from the microcrystalline model is of the order of 10^{-12} s. This value is in good agreement with the electron hopping rate which is estimated from the optical data through the two-site model.

Zusammenfassung

Die vorliegende Arbeit berichtet über Hoch-Temperatur Messungen der optischen Absorption und Reflexion sowie über ESR-Untersuchungen an Seltenerdmetall – Seltenerdmetall Halogenid ($\text{Ln} - \text{LnX}_3$) Schmelzen und deren Mischungen mit flüssigen eutektischen Alkali-Halogeniden. Eine der Hauptschwierigkeiten der spektroskopischen Experimente war bedingt durch die extreme Korrosivität und Sauerstoffempfindlichkeit der fluiden Proben bei hohen Temperaturen, was die Konstruktion geeigneter Messzellen stark beschränkte. Für die Reflexionsmessungen wurde eine optische Küvette aus Molybdän und Quarz neu entwickelt, die einen vakuumdichten Verschluss der Probe garantierte und den direkten Kontakt der Schmelze mit dem optischen Fenster ausschloss. Dennoch traten Schwierigkeiten auf durch Transportreaktionen über die Dampfphase. An den weniger korrosiven Mischungen mit Alkali Halogenid Schmelzen und den Seltenerdmetall Halogeniden wurden optische Absorptions- und ESR-Untersuchungen durchgeführt. Hierbei konnte von vorhandenen Messplätzen für Hoch-Temperatur Experimente ausgegangen werden. Die ESR-Messzelle musste modifiziert werden, so dass sie den besonderen Anforderungen der Seltenerdsysteme genügt.

Hauptzielsetzung dieser Arbeit war, das stark unterschiedliche elektronische Transportverhalten innerhalb der Reihe der fluiden $\text{Ln} - \text{LnX}_3$ Systeme erstmals spektroskopisch aufzuklären. Während die elektronische Leitfähigkeit der Systeme der leichteren seltenen Erdelemente wie La und Ce mit zunehmender Metalldotierung analog den M-MX Schmelzen steil zunimmt, verhalten sich die schweren Metalle wie Nd für alle Zusammensetzungen der $\text{Ln} - \text{LnX}_3$ Mischungen nichtmetallisch. Im ersten Falle kann vermutet werden, dass eine elektronische Lokalisierung ähnlich den Farbzentren in M-MX Schmelzen vorliegt. Im Gegensatz dazu wird in der Literatur angenommen, dass der elektronische Transport in den Neodym- Systemen durch einen „*Intervalence Charge transfer*“ (IVCT) zu erklären ist und dass Subhalogenide existieren. Bisher gibt es keine spektroskopischen Untersuchungen zu dieser Problematik in der Literatur.

Die wesentlichen Ergebnisse lassen sich wie folgt zusammenfassen:

- Die Messungen der optischen Absorption wie auch der ESR in den Ce-Systemen geben bis zu hohen Konzentration entsprechend der Zusammensetzung $(\text{CeI}_2)_{0.24}(\text{CeI}_3)_{0.76}$ keinerlei Hinweis für die Bildung von F-Zentren Zuständen in diesen Schmelzen.

- Die optischen Spektren der flüssigen Mischungen von NdI_2 - NdI_3 sowie Nd - NdCl_3 sind durch eine breite Bande (~ 1 eV) bei 1,6 eV bzw. 1,5 eV gekennzeichnet. Sie zeigt die Merkmale einer IVCT Bande. In eutektischen MX Schmelzen ist dieser Übergang zwischen Nd^{2+} und Nd^{3+} Zuständen zu höheren Energien ($\sim 2,5$ eV) verschoben, was auf eine schwächere Kopplung der gemischtvalenten Ionen zurückgeführt werden kann.
- Durch die Anpassung der optischen Spektren mit einem einfachen Zwei-Platz Modell für das „*polaron hopping*“ wurden die Aktivierungsenergie ($E_A \sim 0,4$ eV) und die Größe der elektronischen Leitfähigkeit ($\sigma_h \sim 1 \Omega^{-1} \text{ cm}^{-1}$) bestimmt. Diese Werte stimmen innerhalb der Fehler quantitativ mit den Ergebnissen neuerer Leitfähigkeitsmessung überein.
- ESR Spektren von gemischtvalenten Neodymchloriden in eutektischen Alkalihalogenid Schmelzen wurden bei verschiedenen Temperaturen bis 420 °C erhalten. Sie sind gekennzeichnet durch eine hohe Linienbreite von max. 10^3 Gauss. Die daraus mit Hilfe des „*microcrystalline Modells*“ abgeschätzten Korrelationszeiten des Elektrons liegen bei $\tau_c \sim 10^{-12}$ s. Dieser Wert stimmt gut überein mit dem nach dem Zwei-Platz Modell aus den optischen Spektren erhaltenen Wert für die Elektronenhüpftrate.

1. Introduction

Among the various types of solutions (Fig. 1.1) mixtures of metallic and non-metallic components have attracted some fundamental interests in physical chemistry and condensed matter physics. The electrical conductivity of these mixtures can vary over more than 10 orders of magnitude between the limits of insulating to metallic states [Kittel88]. On the one hand, the difference between metallic and non-metallic states is discussed within the framework of band theory for crystalline compounds [Kittel88, Ashcroft76]. On the other hand, this problem of electronic structure is less understood for disordered solids or fluid systems. Extensive studies have been performed over several decades e.g. for metal - NH_3 solutions [Thompson76], metal - rare gas mixtures [Micklitz85], metal - molten salt solutions [Warren85, Freyland94, 95] or alkali metal fluids above the critical point [Hensel90]. Among the numerous interested properties of these systems, the phenomenon of metal - nonmetal transition is the most striking feature [Mott90]. In general, a small number of excess electrons released from the metal form localised states, while for higher metal concentration electrons are itinerant. Thus, investigations on the role of electron localisation are especially important to understand the electronic structure of these metal solutions.

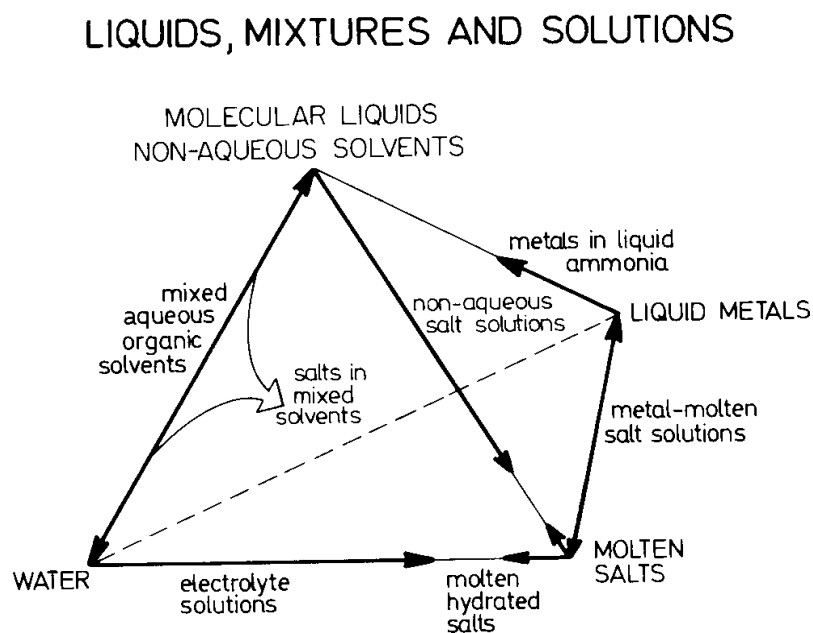


Fig. 1.1 Classification of liquids and mixtures according to the intermolecular forces [Marcus77].

In the case of metal – molten salt solutions the investigations are severely restricted because of the highly corrosive properties of these melts. From the pioneering work of Bredig's group, mainly on electrical conductivity and phase diagram studies, these systems can be divided roughly into the following two groups [Bredig64]:

1. Systems whose physical properties change continuously to metallic states, e.g. alkali-alkali halide (M-MX) melts.
2. Systems, where the metal exists in different stable oxidation states in the melt, leading to the formation of “subhalides” or metal complexes.

Recent experimental progress gives some insight into electron localization and dynamics especially for M-MX melts [Freyland95]. Various kinds of experiments, e.g. electronic conductivity, NMR and ESR as well as spectroscopic measurements for M-MX melts lead to the following scenario for their electronic structures with variation of the metal concentration [Warren84, Haarberg88, Nattland93, Blanckenhagen94, Schindelbeck96]. Excess electrons released from doped metal localise strongly in a cavity of defect anion sites, forming species similar to the F-centre in alkali halides crystals. This is characterised by a dark blue colour with an optical excitation of ~ 1.3 eV for K-KCl melts. A dynamic equilibrium exists between such localized species and mobile electrons where the latter have a mobility of the order of $10^{-1} \text{ cm}^2 \text{ V}^{-1} \text{ s}^{-1}$ which is two orders of magnitude larger than that typical of the ions and is two orders of magnitude smaller than electronic mobilities of alkali metals at the corresponding temperature. With increasing metal concentration an equilibrium between F-centers and spin-paired electrons, so called bipolarons, has to be considered whose existence has been confirmed thorough ESR experiments [Schindelbeck95, 96]. The electronic conductivity increases steeply and metallic characteristics prevail near a metal mole fraction of $x_M \sim 0.2$ [Nattland86]. Theoretical studies, e.g. *ab initio* molecular dynamic simulations of the Car-Parrinello type, support this picture [Silvestrelli96, Koslowski97].

Representative examples of the class 2 type of melts are indium – indium halide melts and refractory metal halides like the Ta(IV)-Ta(V) redox system in an alkali halide melt. The electrical conductivity of these systems does not exhibit metallic conductivity dissimilar to type 1 melts. This is correlated with the existence of several stable oxidation states between metal and salt (non-metallic) states, for instance, In(I) being stable in a mixture of metallic In and non-metallic InI_3 . From NMR and optical studies for the In- InX_3 systems [Ichikawa79, Warren83] a dynamic equilibrium between In(I) and In(III) results via short-lived fluctuations

to the paramagnetic In(II) state by single-electron hopping. Solutions of refractory metal halides in molten salts have been investigated electrochemically and spectroscopically by various groups over decades [Bachtler94, 95, Stöhr98, 99 and references therein]. For the example of TaX₅ melts it has been observed that a parabolic dependence of the electronic conductivity on the composition close to the Ta(IV)/Ta(V) equilibrium occurs with a maximum conductivity of 0.1 Ω⁻¹ cm⁻¹ and a thermal activation energy of 0.3-0.7 eV. Furthermore, an optical excitation has been observed at 1.6 eV which shows a considerably higher oscillator strength compared to that of intraband transitions, e.g. d-d excitations. The authors have concluded that these features are consistent with the optical properties of small polarons frequently encountered in solid state mixed valence compounds, see below. As a consequence, the dominant conduction mechanism in this type of melts is considered to be mixed ionic-electronic transport whereby hopping of electrons between the cation sites with different oxidation states occurs.

With respect to these distinct characteristics of electron localization in molten salt solutions the rare earth – rare earth halide (Ln-LnX₃) systems are of special interest. This is clearly seen from the different behaviour of the electrical conductivity for distinct rare earth, as shown in Fig. 1.2. For lighter rare earth metals, La and Ce, the conductivity exhibits a steep increase with increasing metal concentration, which is similar to alkali-alkali halide melts. On the other hand, the Nd system shows a weak but clear maximum at approximately 23 mole % Nd. In addition, a maximum deviation from additivity of the conductivity of mixtures of NdI₃ and NdI₂ occurs at 16.7 mol % Nd, corresponding to 50 mole % NdI₂, i.e. [Nd²⁺] : [Nd³⁺] = 1 : 1. From this finding Bredig considered the following chemical equilibriums:



He suggested that the equilibrium (1.2) is far to the left in La and Ce systems [Bredig64]. In analogy to the alkali-alkali halide melts it is expected that the excess electrons localize in F-center like states in La and Ce melts. On the other hand, in the Nd system the equilibrium (1.2) is on the right side and the electrical conduction is dominated by electron hopping between divalent and trivalent Nd cations. However, this conjecture is only based on the different concentration dependence of the conductivities and further experimental evidence, e.g. by spectroscopic methods, has not been reported so far.

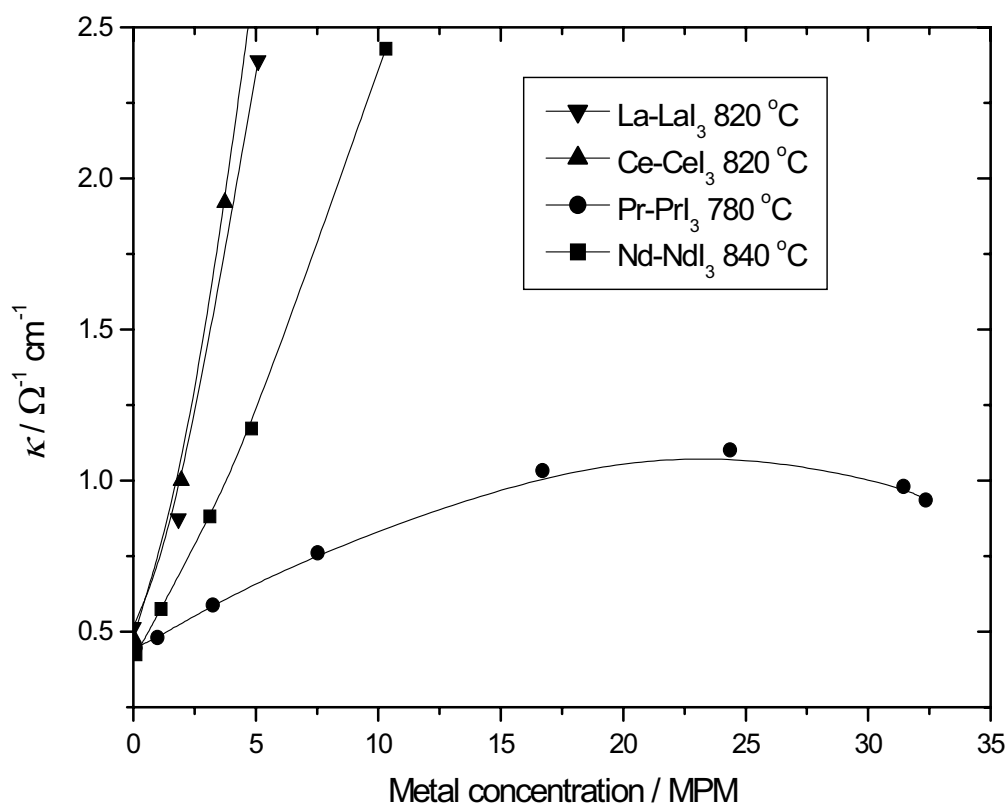


Fig. 1.2 Specific conductivity of Ln-LnX₃ melts around 800 °C as a function of metal concentration [Bredig64].

$$\text{MPM (mole \% metal)} = \left\{ \frac{\text{mole of metal}}{\text{mole of metal} + \text{mole of salts}} \right\} \times 100.$$

In solid-state physics and chemistry this problem is related with the valence stability of rare earth ions. As is well known in inorganic chemistry, the majority of rare earth compounds has the oxidation state of three (equilibrium (1.1)). This trend holds also for the halide compounds. Several reduced halides with LnX_n (n<3) are, however, known to exist. Especially, a number of di-iodide compounds exist because of the less electronegative character of the iodide ion [Haschke79, Meyer88]. Among them lanthanum, cerium and praseodymium di-iodides show metallic character¹. Both theoretical and experimental studies, e.g. electrical conductivity [Corbett64], magnetic susceptibility [Burrow87] and photoelectron spectroscopy measurements [Stöwe97], show that the electronic structure of such compounds, LaI₂ or CeI₂, can be described as Ln³⁺·e⁻·(I⁻)₂, where the excess electrons occupy the 5d

¹ In addition, solid NdI₂ shows a high-pressure modification from salt-like to metallic character [Beck76, 92] – see also section 6.3.3.1.

conduction band. Hence, starting from the systems of the lighter rare earth metals with metallic character, the 5d character changes to that of the localised 4f electron for heavier rare earth metal systems.

In the latter case rare earth ions exist with different oxidation states which is analogous to the type 2 melts above. Such a compound can be discussed in terms of “Mixed Valence Compounds” whose classification will be presented in the next chapter. For solid rare earth halides extensive studies have been carried out especially with emphasis on the structural characterisation. Lange performed the synthesis of mixed valent europium halide crystals and showed that the optical properties can be described by small polaron theory where an electron is transferred by thermally activated processes and by the optical excitation between rare earth ion sites with different oxidation states in equilibrium (1.2) [Lange92].

The main focus in the present study is to characterise the different electronic structures and transport properties of Ln-LnX₃ melts. Though optical measurements can give a relatively direct information on the electronic structure of these systems, the experiments have not been performed so far for the Ln-LnX₃ melts because of their extremely corrosive properties in contact with the optical window materials. The chemical properties of the melts will be surveyed in the experimental section. In the present work both absorption and reflectivity measurements have been carried out in order to get further insight to the electronic properties of these melts. Moreover, a first attempt of ESR measurements has been performed for a few rare earth halide - alkali halide mixtures. The results will be discussed in the light of the existing literature data for both type 1 and 2 melts and solid LnX_n compounds.

Besides the fundamental aspects sketched above, the electronic properties of Ln-LnX₃ melts are of some technological interest with respect to the following new applications: electrowinning and electrorefining of rare earth metals in molten salt matrix [Yamamura98], electrochemical synthesis of rare earth alloys [Xie93], recycling of spent fuel from fast nuclear reactors [Iizuka97]. Moreover, the investigation of rare earth ions in glass or gas phases is currently intensively investigated for the application of efficient laser materials or discharge lamps [Boghosian96].

2. Some basic spectroscopic concepts and properties of the present systems

2.1 Optical properties of light absorbing media

In this section some optical properties and basic spectroscopic definitions are introduced which are used in the following sections. Detailed descriptions are found in many textbooks, e.g. [Atkins90, Hecht87, Grosse79, Wooten72].

2.1.1 Absorption and reflection of light

The interaction of light (electric field \mathbf{E} and magnetic field \mathbf{B}) with the medium is described within the linear approximation through the polarisation, \mathbf{P} , free current density, \mathbf{J} , and magnetisation, \mathbf{M} , as

$$\mathbf{P} = \chi_e \epsilon_0 \mathbf{E}, \quad \mathbf{M} = \chi_m \mu_0 \mathbf{H}, \quad \mathbf{J} = \sigma \mathbf{E}, \quad (2.1)$$

where χ_e is the electric susceptibility, χ_m is the magnetic susceptibility, ϵ_0 and μ_0 is, respectively, permittivity and permeability of vacuum and σ is the electrical conductivity.

In the case of no external charge sources, the wave equation for a plane wave propagating in an energy-absorbing medium is derived from Maxwell equations as:

$$\nabla^2 \mathbf{E} = \mu \mu_0 \epsilon_0 \epsilon \frac{\partial^2 \mathbf{E}}{\partial t^2} + \sigma \mu \mu_0 \frac{\partial \mathbf{E}}{\partial t}, \quad (2.2)$$

where t is time, and ϵ and μ are the relative permittivity (dielectric constant) and the relative permeability of medium, respectively. Anticipating that the wave vector must be complex to describe energy dissipation of the wave, the electric field is written as

$$\mathbf{E} = \mathbf{E}_0 \exp\{i(\mathbf{q} \cdot \mathbf{r} - \omega t)\}, \quad (2.3)$$

where \mathbf{E}_0 is perpendicular to the wave vector \mathbf{q} . A complex refractive index is defined as

$$\mathbf{q} = (\omega / c) \hat{n} = (\omega / c)(n + ik). \quad (2.4)$$

with c = speed of light, n = refractive index, and k = absorption coefficient. Defining a complex dielectric function, $\hat{\epsilon}$, as

$$\hat{\epsilon} \equiv \epsilon_1 + i\epsilon_2 \equiv \hat{n}^2 / \mu, \quad (2.5)$$

where ϵ_1 represents ϵ used before, the relation of real and imaginary part of dielectric constant yields the following expression from eqns. (2.2) - (2.5) and the relation $c = 1/(\mu_0 \epsilon_0)^{1/2}$:

$$\varepsilon_1 = \frac{n^2 - k^2}{\mu}, \quad \varepsilon_2 = \frac{\sigma}{\omega\varepsilon_0} = \frac{2nk}{\mu}. \quad (2.6)$$

Eqn. (2.3) can be now rewritten as

$$\mathbf{E} = \mathbf{E}_0 \exp\left(-\frac{\omega}{c} \mathbf{k} \cdot \mathbf{r}\right) \exp\left\{i\left(\frac{\omega}{c} \mathbf{n} \cdot \mathbf{r} - \omega t\right)\right\}. \quad (2.7)$$

The absorption constant K is defined through Lambert-Beer's Law as

$$\frac{dI}{dr} \equiv -KI, \quad (2.8)$$

where I is the intensity of light. This yields

$$\ln\left(\frac{I_0}{I}\right) = Kd \quad \text{and} \quad A \equiv \log\left(\frac{I_0}{I}\right) = C\varepsilon d, \quad (2.9)$$

where I_0 is the intensity of incident beam and I is that of light going through the absorbing media, d is the optical path length, C is the concentration. A is called absorbance and ε molar extinction coefficient.

Since the intensity of light is proportional to the square of the wave amplitude, the absorption constant is expressed in terms of k or σ for non-magnetic media, i.e. $\mu = 1$, from eqns. (2.6) and (2.8) as:

$$K = 2\omega k/c = 4\pi k/\lambda = \sigma/n\varepsilon_0 c. \quad (2.10)$$

The reflectance of light incoming onto the interface of other medium at normal incident is derived from a consideration of the boundary conditions for \mathbf{E} and \mathbf{H} at the interface. For an electric field

$$E_i + E_r = E_t, \quad (2.11)$$

where the subscript i, r and t means incident, reflection and transmission, respectively. Since magnetic field \mathbf{H} is perpendicular to \mathbf{E} in the sense that $\mathbf{E} \times \mathbf{H}$ is in direction of the wave propagation, the boundary condition for H yields

$$H_i - H_r = H_t. \quad (2.12)$$

In a m -th medium, E and H is related in terms of refractive index and magnetic permeability of the medium by

$$H = \frac{\hat{n}_m}{\sqrt{\mu_m}} E. \quad (2.13)$$

Thus, from (2.11)-(2.13) reflectance wave amplitude becomes

$$\hat{r} \equiv \frac{E_r}{E_i} = \left(\frac{\hat{n}_1}{\sqrt{\mu_1}} - \frac{\hat{n}_2}{\sqrt{\mu_2}} \right) / \left(\frac{\hat{n}_1}{\sqrt{\mu_1}} + \frac{\hat{n}_2}{\sqrt{\mu_2}} \right) \quad (2.14)$$

For non magnetic medium, i.e. $\mu_1 = \mu_2 = 1$, the reflectivity is thus given by

$$R \equiv \hat{r}^* \hat{r} = \frac{(\hat{n}_1 - \hat{n}_2)^2}{(\hat{n}_1 + \hat{n}_2)^2}. \quad (2.15)$$

Accordingly, the measurements of absorption and reflectivity provide the direct information of optical constants, n and k , and consequently dielectric constants.

2.1.2 Lorentz oscillator model and Drude model for free charges in metal

In the above case the medium is treated as a continuum. For the full explanation of the variation of optical constants with frequency it is necessary to consider the reaction between the electrical component of the incident electromagnetic wave and the electrons in the material.

The classical Lorentz model considers an atom with electrons bound to the nucleus in much the same way as a small mass can be bound to a large mass by a spring in the influence of an electric field. From the classical equation of an electron including the damping factor, the frequency dependence of dielectric constants for a non-magnetic material read the following expressions:

$$\varepsilon_1 = 1 + \frac{Ne^2}{\varepsilon_0 m_e} \frac{\omega_0^2 - \omega^2}{(\omega_0^2 - \omega^2)^2 + \Gamma^2 \omega^2}, \quad \varepsilon_2 = \frac{Ne^2}{\varepsilon_0 m_e} \frac{\Gamma \omega}{(\omega_0^2 - \omega^2)^2 + \Gamma^2 \omega^2}, \quad (2.16)$$

where N is the number of density of bounding electrons, ω_0 is the resonance frequency, m_e is the mass of free electron, Γ is the damping constant and e is the charge of electron.

Since the conduction electrons of a metal are not bound to the nucleus, dielectric constants are obtained directly from the Lorentz model by setting the ω_0 zero and considering the damping term as scattering of electron with phonons and lattice defects as follows (Drude model):

$$\varepsilon_1 = 1 - \frac{\sigma_0 \tau}{\varepsilon_0 (1 + \omega^2 \tau^2)}, \quad \varepsilon_2 = \frac{\sigma_0}{\varepsilon_0 \omega (1 + \omega^2 \tau^2)}, \quad (2.17)$$

where τ is the mean free time between collisions and σ_0 is the DC electrical conductivity, i.e. $\sigma_0 = e^2 N \tau / m_e$. The dielectric function can be then converted to the absorption constant through

$$K(\hbar\omega) = \frac{2\hbar\omega}{c} \left[\frac{1}{2} \left(\sqrt{\varepsilon_1^2 + \varepsilon_2^2} - \varepsilon_1 \right) \right]^{1/2}, \quad (2.18)$$

with \hbar = Planck constant divided by 2π . It should be noted that the absorption constant is related with the DC conductivity and number of density, N .

2.1.3 Oscillator strength

For a comparison of experimental and theoretical spectral intensities the oscillator strength, f , is a suitable quantity. It is a dimensionless quantity which relates the transition dipole moment, μ_{fi} , with the integrated intensity of the absorbance, $\int A d\nu$. It is defined by:

$$f \equiv \left(\frac{4\pi m_e \nu_{fi}}{3e^2 \hbar} \right) |\mu_{fi}|^2, \quad (2.19)$$

where ν_{fi} is the frequency of the optical excitation. This is further related with $\int A d\nu$ by:

$$f \equiv \left(\frac{4m_e c \varepsilon_0}{N_A e^2} \right) \int A d\nu, \quad (2.20)$$

where N_A is Avogadro's number. Substitution of the constant values yields the following expression with the consideration of the influence of matrix through its refractive index:

$$f = 4.19 \times 10^{-9} \frac{9n}{(n^2 + 2)^2} \int A d\tilde{\nu}, \quad (2.21)$$

where the integration is carried out with respect to wave number ($\tilde{\nu}$ / cm^{-1}).

In principle, the oscillator strength is 1 for parity allowed transition, and is zero for parity forbidden excitations in three dimensional system. However, in practice for parity allowed transitions the oscillator strength is of the order of 10^{-1} to 1, while that for parity forbidden is 10^{-5} to 10^{-7} because of, for instance, distorted symmetry around electrons due to electron – phonon coupling.

2.2 Electron Spin Resonance

In the following a brief description of the basics of ESR is presented. Details are found in many textbooks, for example [Atherton93, Carrington67, Slichter90].

2.2.1 Zeeman effect and Bloch equations

First we consider a spin system with magnetic moment $\boldsymbol{\mu}$ and the spin momentum $\hbar\mathbf{S}$. These two quantities are related by

$$\boldsymbol{\mu} = -\gamma\hbar\mathbf{S}, \quad (2.22)$$

where γ is the magnetogyric ratio which is given in terms of g-factor, g_e , by:

$$\gamma = g_e e / 2m_e. \quad (2.23)$$

The negative sign in eqn. (2.22) represents that the magnetic moment and the spin are oppositely directed. The interaction energy between the external static magnetic field², \mathbf{B} , and the above magnetic moment is

$$U = -\boldsymbol{\mu} \cdot \mathbf{B}. \quad (2.24)$$

Taking the direction of magnetic field as z , this becomes

$$U = -\mu_z B = \gamma\hbar S_z \cdot B. \quad (2.25)$$

For the spin of $S = 1/2$ there are two corresponding energy levels (Zeeman splitting).

Writing the energy difference as $\hbar\omega_0$, we have

$$\begin{aligned} \hbar\omega_0 &= \gamma\hbar(1/2) \cdot B - (\gamma\hbar(-1/2) \cdot B) \\ \text{or} \quad \omega_0 &= \gamma B. \end{aligned} \quad (2.26)$$

The time variation of the angular momentum is equal to torque acting on the system. For the magnetic moment in a static magnetic field \mathbf{B} this force is $\mathbf{B} \times \boldsymbol{\mu}$, and thus we have

$$d\boldsymbol{\mu} / dt = \gamma \mathbf{B} \times \boldsymbol{\mu}. \quad (2.27)$$

Multiplying by the total number of N spins, the observable macroscopic magnetisation, $\mathbf{M} = N\boldsymbol{\mu}$, is:

$$d\mathbf{M} / dt = \gamma \mathbf{B} \times \mathbf{M}. \quad (2.28)$$

Applying a microwave field with the Larmor frequency, ω_0 (eqn. 2.26), magnetisation in thermal equilibrium is distorted. The corresponding relaxation processes can be described in terms of phenomenological relaxation times T_1 and T_2 . The equations of motion for the magnetisation, Bloch equations, are

¹ The relation between magnetogyric ratio and Bohr magneton μ_B (often used in literatures) is given by $\hbar\gamma_e = g_e\mu_B$.

² As is widely used in literature, the magnetic induction flux density \mathbf{B} is used instead of \mathbf{H} in this section.

$$\frac{dM_x}{dt} = \gamma (\mathbf{B} \times \mathbf{M})_x - \frac{M_x}{T_2}, \quad \frac{dM_y}{dt} = \gamma (\mathbf{B} \times \mathbf{M})_y - \frac{M_y}{T_2}, \quad \frac{dM_z}{dt} = \gamma (\mathbf{B} \times \mathbf{M})_z + \frac{M_0 - M_z}{T_1}. \quad (2.29)$$

Because T_1 represents the decay of magnetization in the direction of the static field, it is called the longitudinal relaxation time and corresponds to the spin – lattice interaction. On the other hand, T_2 characterises the relaxation in the xy-plane, i.e. decay of the phase coherence perpendicular to the magnetic field among spins. This is, therefore, called the transverse relaxation time.

In the case of homogeneous Lorentz curve of the ESR absorption, the relation between T_2 and the width at half height of the absorption peak, $\Delta B_{1/2}$, is

$$T_2 = \frac{2}{\gamma_e \Delta B_{1/2}}. \quad (2.31)$$

In some cases, especially in ESR of solid compounds, a broadening of the width is observed, which cannot be characterised by a Lorentz curve, but by a Gaussian or a combination of Lorentzian and Gaussian. For such inhomogeneous line broadening effects, such as inhomogeneous magnetic fields or interaction between neighbouring molecules play an important role.

2.2.2 Spin Hamiltonian

The fine and hyperfine structures of the ESR spectra are caused by the intrinsic electronic and magnetic interactions of electrons and nuclei. These are determined by the spin hamiltonian which gives the information on the microscopic structure and dynamics of the system. The most important contributions to the spin Hamiltonian for electrons with spin $1/2$ are:

$$\hat{H} = \hat{H}_0 + \hat{H}_Z + \hat{H}_{SO} + \hat{H}_{hf} + \hat{H}_{dip} + \hat{H}_{exch}. \quad (2.33)$$

Each term means:

\hat{H}_0 : Kinetic and potential energy of the system without magnetic interaction.

\hat{H}_Z : Zeeman term, interaction between spin / angular momentum and external static magnetic field, $\hat{H}_Z = \mu_B (\mathbf{L} + g_e \mathbf{S}) \mathbf{B}$ where \mathbf{L} is angular momentum and μ_B is the Bohr magneton.

\hat{H}_{SO} : Spin-Orbit coupling, interaction between electron spin and angular momentum. The angular momentum creates a magnetic field at the position of the electron:

$$\hat{H}_{SO} = \left(\frac{e\hbar}{2m_e^2 c^2} \right) \mathbf{S} \cdot (\mathbf{E} \times \mathbf{p}) = \lambda_{SO} \mathbf{L} \cdot \mathbf{S}, \quad (2.34)$$

where \mathbf{E} is the electric field due to the nucleus and \mathbf{p} is the momentum of electron.

For a spherical symmetrical potential, ϕ , we have

$$(\mathbf{E} \times \mathbf{p}) = \frac{1}{r} \frac{d\phi}{dr} (\mathbf{r} \times \mathbf{p}) = \frac{e\hbar Z}{4\pi\epsilon_0} \langle r^{-3} \rangle \mathbf{L}. \quad (2.35)$$

The mean value of the orbital radius $\langle r \rangle$ is approximately inversely proportional to the nuclear charge, Z . Therefore, the spin – orbit coupling constant is $\lambda_{SO} \propto Z^4$, i.e. the spin – orbit coupling increases drastically with increasing nuclear charge. Especially for rare earth compounds the spin – orbit coupling is the dominant factor for relaxation process.

\hat{H}_{hf} : Hyperfine structure term, interaction between magnetic moment of nuclei and electrons. For s-electrons the direct quantum mechanical interaction is described with so called Fermi contact term

$$\hat{H}_{hf,F} = A \sum_{i,k} \mathbf{S}_i \cdot \mathbf{I}_k. \quad (2.36)$$

Since the hyperfine coupling constant, A , is proportional to the spin density at the nucleus, i.e. $A \propto |\Psi(0)|^2$, NMR and ESR measurements of hyperfine structure give the electron spin density at the nucleus.

For electrons with quantum number of $l > 1$, weak dipolar contributions have to be considered:

$$\hat{H}_{hf,dip} = \frac{\mu_0}{4\pi} \gamma_e \gamma_n \hbar^2 \sum_{i,n} \frac{3(\mathbf{S}_i \mathbf{r}_{in})(\mathbf{I}_n \mathbf{r}_{in})}{r_{in}^5} - \frac{\mathbf{S}_i \mathbf{I}_n}{r_{in}^3}, \quad (2.37)$$

where γ_n and I_k are the magnetogyric ratio and the angular momentum of the nucleus, respectively.

\hat{H}_{dip} : Dipole-dipole interaction between magnetic moment of electron spins. An electron spin produces dipole field according to:

$$\mathbf{B}_{dip} = \frac{\mu_0}{4\pi} \left(\frac{3(\boldsymbol{\mu}_e \mathbf{r}) \mathbf{r}}{r^5} - \frac{\boldsymbol{\mu}_e}{r^3} \right) = \frac{\mu_0}{4\pi} \gamma_e \hbar \left(\frac{\mathbf{S}}{r^3} - \frac{3(\mathbf{S} \mathbf{r}) \mathbf{r}}{r^5} \right). \quad (2.38)$$

The Hamiltonian is thus:

$$\hat{H}_{dip} = \frac{\mu_0}{4\pi} \gamma_e^2 \hbar^2 \sum_{i < j} \left(\frac{\mathbf{S}_i \mathbf{S}_j}{r_{ij}^3} - \frac{3(\mathbf{S}_i \mathbf{r}_{ij})(\mathbf{S}_j \mathbf{r}_{ij})}{r_{ij}^5} \right). \quad (2.39)$$

This interaction plays an important role for the line width in solid state compounds. For liquids, however, this term is often very small and can be neglected because of averaging over different orientations.

\hat{H}_{exch} : Exchange interaction between two electron spins, not a real magnetic interaction but a Coulomb interaction manifested in the Pauli principle,

$$\hat{H}_{exch} = \sum_{i < j} J_{ij} \mathbf{S}_i \mathbf{S}_j. \quad (2.40)$$

This interaction may have a large influence on the line width, but only if a large overlap, J , of wave function exists.

2.3 Electronic transitions and optical properties of rare earth ions

In this section characteristic optical properties of rare earth ions are summarised, which are required to interpret the optical data of the present systems.

2.3.1 Intra 4f transitions

Since these excitations are parity forbidden, intensities of f-f transitions are weak and the oscillator strength is of the order of 10^{-6} . Moreover, these transitions show very sharp peaks and are insensitive to the chemical environments surrounding the ions of interest (“atomic” like states). This is explained by the fact that the 4f orbital is well shielded by the $5s^2$ and $5p^6$ orbitals. Consequently, this insensitive character to the surrounding or ligand has the benefit that the peak positions of f-f transitions can be easily assigned from those of the free ions. Some differences depending on different matrices will be mentioned in the forthcoming sections. Extensive works have been carried out in the various matrices, i.e. crystals [Hüfner78], melts [Smith64], gas phases [Boghossian96]. Readers are referred to the literatures for the details.

2.3.2 Nephelauxetic effect

A slight shift of peak positions of f-f transitions depending on the matrix is known as the “nephelauxetic effect” (cloud-expanding in Greek). The excited levels of transition bands are primarily determined by interelectronic repulsion and spin-orbit coupling. For covalent compounds (such as oxides) the apparent values of the inter-electronic repulsion parameters are smaller than those in aqueous solutions and fluorides. This causes a shift of the peak positions toward lower energy with increasing covalency of the surrounding media. This effect is much weaker in the 4f shell of lanthanide complexes than in the 3d, 4d and 5d shells of ordinary transition group complexes, though it is quite perceptible in Pr^{3+} , Nd^{3+} , Sm^{3+} and Gd^{3+} [Ephraim, Jørgensen64].

A measure of nephelauxetic effect is given by the ratio, $\beta = \nu_{\text{comp}}/\nu_{\text{free}}$ (nephelauxetic ratio), where ν_{comp} and ν_{free} are the transition energy in wave number of a compound of interest and that of the free ion³, respectively, so that the higher value of $1-\beta$ represents the covalent tendency. A detailed discussion of the nephelauxetic effect in rare earths is found in e.g. [Sinha66a, b].

2.3.3 Hypersensitive transitions

The intensities of some f-f transitions are known to depend strongly on both ligand field and structural alterations. These transitions are called „hypersensitive“ transitions and have been the subject of many research efforts. The following experimental facts are known:

1. Intensities increase when the lanthanide is surrounded by a field of decreasing symmetry. If the lanthanide ion lies on a centre of symmetry, the hypersensitive band intensity is almost zero.
2. For isostructural halide compounds, the intensity appears to increase in the order $\text{I}^- > \text{Br}^- > \text{Cl}^- > \text{F}^-$.
3. Hypersensitivity is proportional to the nephelauxetic ratio (see the previous section) and possibly correlated to the Ln-X covalency.
4. A correlation exists between the hypersensitive intensities and the electron donating ability (basicity) of the ligand. The more basic the ligand, the more intense the hypersensitive band is.

³ In literature the peak frequency of aqueous solution, ν_{aqu} , is used instead of ν_{free} .

A number of influences on hypersensitivity have been considered, such as lattice vibrations, electric field gradients, and a dynamic coupling (mixing of the ligand wave functions due to inclusion of unoccupied orbitals), but so far no consistent explanation has been found. Probably a combination of the above effects has to be considered [Boghosian96, Hüfner78].

2.3.4 Theoretical treatment of f-f transition intensities, Judd-Ofelt theory

In the framework of Judd-Ofelt theory, the oscillator strength of f-f transitions (transition from S, L, J state to S', L', J' with Russel-Saunders' notation) is described as follows [Judd62, Ofelt62]:

$$f = \frac{8\pi^2 m_e \tilde{\nu} c}{3h(2J+1)} \left[\frac{(n^2+2)^2}{9n} S_{ed} + nS_{md} \right] \cong 6.38 \times 10^9 \tilde{\nu} \left[\frac{(n^2+2)^2}{9n} S_{ed} + nS_{md} \right], \quad (2.41)$$

where S_{ed} and S_{md} represent the line strength for the induced electric and magnetic transition, n is refractive index of matrix, and $\tilde{\nu}$ is the peak frequency of the transition in wave number (cm^{-1}).

Both S_{ed} and S_{md} are given by:

$$S_{ed} = \sum_{k=2,4,6} \Omega_k \left| \langle S'L'J' \| U^k \| SLJ \rangle \right|^2 \quad \text{and} \quad S_{md} = \sum_{k=2,4,6} \Omega_k \left| \langle S'L'J' \| L + 2S \| SLJ \rangle \right|^2. \quad (2.42)$$

The values of the reduced matrix elements of the unit tensor operator of rare earth ion are known, independent of the hosts. Thus, if there are three experimental data sets of the oscillator strength, it is possible to evaluate the Ω_k ($k=2,4,6$) by using the literature data of U^k . The parameter U^2 is known to be especially sensitive to the environment around the rare earth ion. The others (U^4 and U^6) are generally less sensitive to the chemical environment.

An example of this analysis is found in the literature [Chrissanthopoulos00] where the electronic absorption spectra of Ho^{3+} in GdCl_3 – alkali halide melts were studied. The parameter U^2 varies drastically with the concentration of matrix, reflecting the structural change.

2.3.5 f-d transitions

Fig. 2.1 shows the result of the analysis of the free ion spectra of trivalent and divalent ions. Although the respective relative energy positions in condensed matter are different from those of free ions (e.g. about 30 % lower for solids [Hüfner78]), the general trend is preserved. As can be seen in the figure, the optical excitations from 4f to 5d states occur in the UV range or at higher energy for trivalent rare earth ions. However, a smaller energy separation makes it possible that in the case of rare earth divalent ions the f-d transitions occur in the NIR to VIS range. This is due to the larger 4f orbital radius by the addition of one 4f electron.

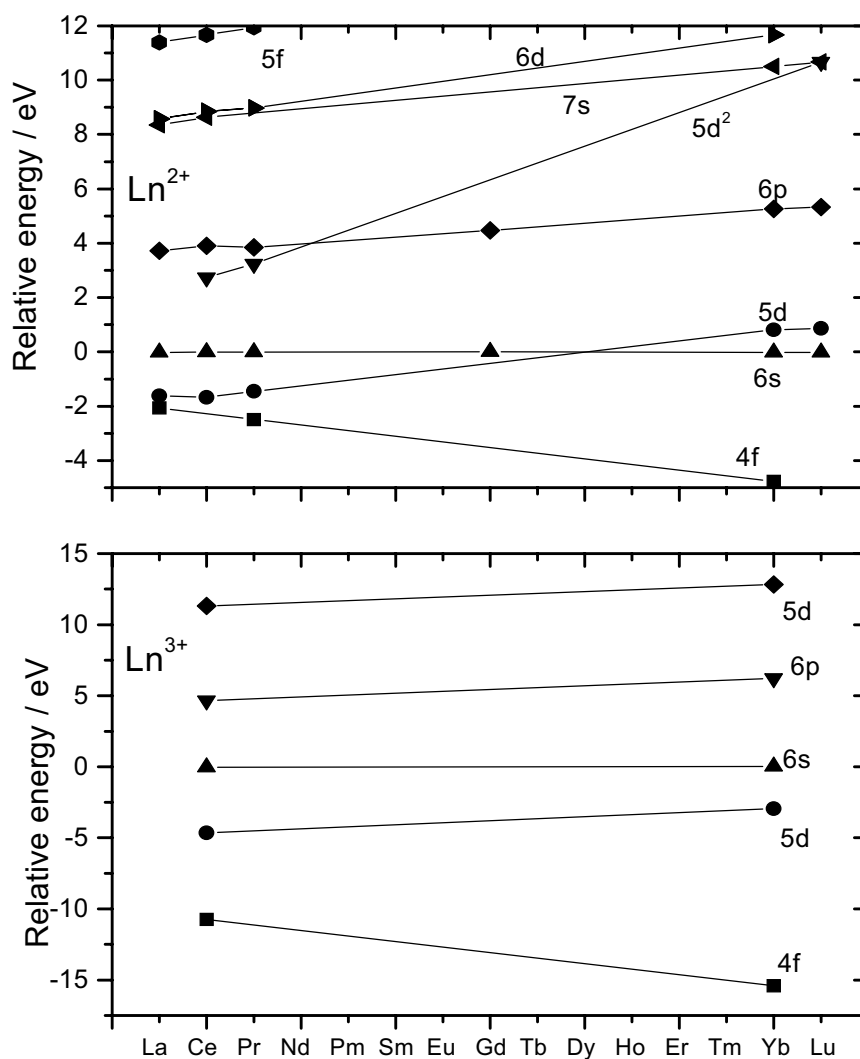


Fig. 2.1 Approximate relative energy position of the ground and excited states for the divalent (upper panel) and trivalent (lower panel) rare earth free ion [Hüfner78].

The f-d excitations are no more parity forbidden, so that their intensities are quite strong with the oscillator strengths of the order of 10^{-1} . In many cases they can obscure the intra 4f transitions.

The excited 5d orbitals are strongly influenced by the surrounding ligand fields, as is well known in optical spectra of transition metal compounds. Both peak positions and intensities of f-d transitions are, therefore, very sensitive to the chemical environments of the rare earth ions of interest.

2.3.6 Charge transfer bands

Another intense optical excitations observed in the rare earth ion systems are charge transfer transitions, e.g. from ligand to rare earth f orbital. Examples are found in absorption measurements of rare earth ions in organic solvents [Ryan66, Keller76]. The difference with respect to f-d transitions is for instance that the energy position does not change among the different alcohol solvents. The detailed treatment of charge transfer bands in the rare earth halide melts will be described in the discussion section.

2.4 Classical Classification of mixed valence solid compounds

As mentioned in the introduction, the elements are expected to exist with different oxidation states in the melts in the heavier rare earth systems of interest here. Such systems may be characterised as “Mixed valence compounds”, whose well known examples are Fe_3O_4 (magnetite) = $\text{Fe}^{2+}\text{Fe}_2^{3+}\text{O}_4$ and Prussian blue, $\text{KFe}^{3+}[\text{Fe}^{2+}(\text{CN})_6]$. In this section the classical classification of mixed valence compounds by Robin and Day [Robin67] is presented.

In such compounds characteristic optical absorptions are found, which cannot be expected from the summation of those of the isolated constituting ions. Robin and Day classified mixed valence compounds by considering the mixing of wave functions of valence sites with different oxidation states A and B (e.g. A: divalent, B: trivalent) with the following ground state wave function:

$$\Psi = \sqrt{1-\alpha^2}\phi_A + \alpha\phi_B \quad \alpha: \text{mixing parameter.}$$

From first order perturbation theory, the potential surface between the sites of interest is classified according to the different value of mixing parameter.

Class I $\alpha \approx 0$

The ions of differing valency are at sites of very different symmetry and ligand field strength. Sites are inequivalent.

Examples: $\text{Cs}_2\text{Au}_2\text{Cl}_6$

Eu_3O_4 : calcium ferrite (CaFe_2O_6) structure

Eu^{3+} : 8 oxygen coordinated

Eu^{2+} : 6 oxygen coordinated

For compounds of this class the optical absorption is a summation of that of isolated or separated ions.

Class II $0 < \alpha < \sqrt{2}/2$

Sites A and B are rather similar, though crystallographically distinguishable. In parallel, delocalization takes place.

Examples: Eu_3S_4 , Na_xWO_3 ($x < 0.3$), Ti_4O_7

The optical properties of these compounds result from a summation of respective ions and, in addition, one or more additional bands can occur.

Class III $\alpha = \sqrt{2}/2$ i.e. $\Psi_{\pm} = 2^{-1/2}(\phi_A \pm \phi_B)$

The two types of ions are in exactly equivalent sites. Delocalization of electron between sites takes place. This class can be further divided into two sub categories depending on the delocalisation of electrons.

(Class IIIA)

Metal Clusters. In this type electrons delocalise within the cluster size.

Example: $\text{Nb}_6\text{Cl}_{12}^{2+}$

(Class IIIB)

Metallic compounds. Electron delocalises throughout the systems.

Examples: Na_xWO_3 ($0.3 < x < 0.9$), SmS at high pressure

In recent studies on mixed valence compounds another category, i.e. Class II-III, has been introduced in order to describe the physical properties of some compounds, for instance, the

Creuz-Taube ion, i.e. $[(\text{NH}_3)_5\text{Ru}(\text{pyrazine})\text{Ru}(\text{NH}_3)_5]^{5+}$ where the electrons are expected to be delocalised throughout the ion but a “residue” of localised states exist (details are found in review articles, e.g. [Demadis01]). Nevertheless, Robin and Day’s classification gives the basic concepts for understanding the systems with different oxidation states.

A schematic potential surface between two metal sites is shown in Fig. 2.2 for class II and III mixed valence compounds. An extra electron delocalises between two metal sites, if the electronic coupling is strong enough (dotted potential surface, class III). On the other hand, an electron is localised at one metal site in the case of the dashed line potential (class II). In this case the electron can only be transferred by thermally activated hopping processes with activation energy, E_{act} , or by optical excitation with excitation energy of E_{opt} . The problem of electron transfer is of fundamental interest in a variety of different scientific fields, e.g. solid state physics, electrochemistry, biology. Extensive researches have been carried out both theoretically and experimentally [Kuznetsov99, Jortner99]. Further details, especially on optical properties, of mixed valence compounds will be discussed in the discussion section.

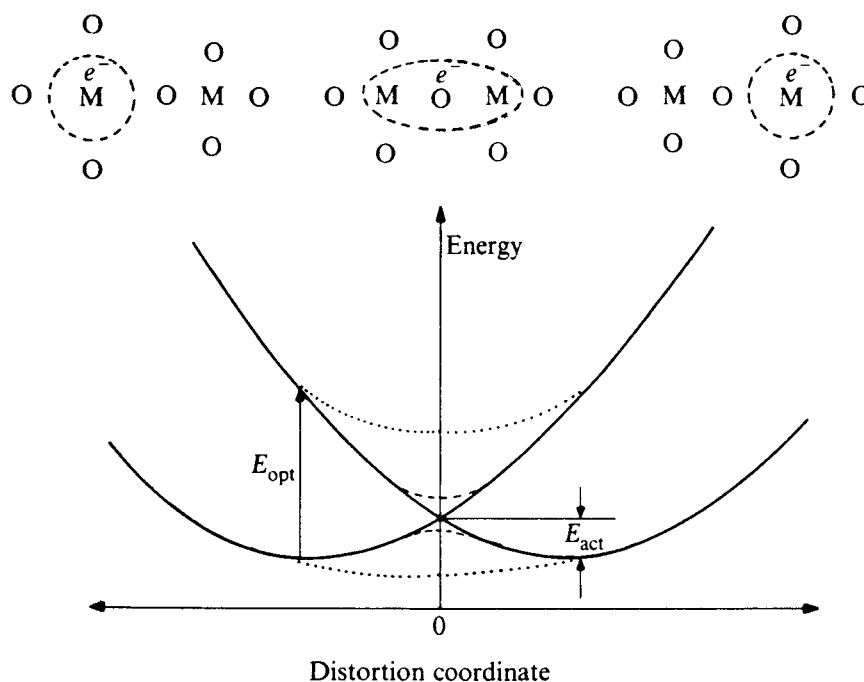


Fig. 2.2 Configuration coordinate diagram for a pair of metal atoms with one extra electron [Cox87]. Dashed line: weak electronic interaction at the crossover point (class II), dotted line: strong coupling between two sites (class III).

3. Experimental section

3.1 Preparation of chemicals

3.1.1 General remarks on chemical reactivity of the present systems

All salts used in this work are extremely hygroscopic. Rare earth metals are easily oxidised in the air atmosphere. Especially the oxidation process is a crucial factor for the present study. Jungmann performed photoemission spectroscopy measurements of solid CeI_2 and LaI_2 under the following experimental conditions: partial pressure of O_2 less than 10 ppm in the glove box, ultrahigh vacuum chamber with $\text{O}_2 < 10^{-10}$ mbar [Jungmann95]. The oxidation process of rare earth dihalides, i.e. $2 \text{LnI}_2 + \text{O}_2 \rightarrow 2\text{LnOI} + \text{I}_2$, could be clearly detected by the disappearance of the Fermi edge within a day. Therefore, in our experiments the materials were handled in an Ar filled glove box (Braun) with the atmosphere of O_2 and H_2O less than 2 ppm and stored in sealed quartz ampoules under vacuum.

The melts of Ln-LnX_3 are known to attack ceramic materials aggressively, yielding their oxihalides [Gmelin82]. The following materials were examined by corrosion tests against Ln-LnX_3 melts: MgO , ZrO_2 , Al_2O_3 , SiO_2 . However, no corrosion resistant ceramic materials have been found up to now. The only possible materials for melt reservoirs are Mo, Ta, W [Gmelin82] and glassy carbon [Jörger98]. Especially tantalum is recommended for synthesis of rare earth dihalides at high temperature [Corbett83].

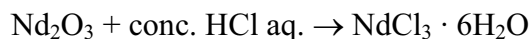
Some measurements were performed with the melt in contact with quartz or sapphire for the less corrosive $\text{LnX}_2\text{-LnX}_3\text{-(LiX-KX)}_{\text{eut}}$ and $\text{LnI}_2\text{-LnI}_3$ melts. Mixtures with alkali halide eutectics have lower melting points compared with pure Ln-LnX_3 mixtures and, therefore, are expected to be less corrosive. Further details of the chemical reactivity of the present systems will be given in chapter 4.

3.1.2 Preparation of rare earth metal and rare earth halides

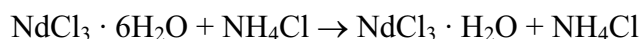
Rare earth metals (99.9 %, Alfa) were cleaned shortly in HNO_3 and then rinsed with acetone in order to get rid of the oxide on the surface [Kvam98]. The remaining oxide on the metal surface was removed mechanically in the glove box.

Rare earth tri-halide salts were synthesised from their oxides (99.9 %, produced in the chemistry department at the University of Lublin, Poland) at the technical university in Wroclaw, Poland with the following scheme [Gaune-Escard94], described here for the NdCl_3 :

1. Chlorination of oxides



2. Dyhydration



The salts were further distilled in a quartz tube ca. 10°C above their melting points (cf. mp of NdCl_3 : 758°C [Bredig64]) with the equipment displayed schematically in Fig. 3.1. Under an inert atmosphere raw salt was introduced in a quartz reservoir. The whole component was then connected to the vacuum pump ($\sim 10^{-5}$ mbar) and after evacuation the distillation was started. Because of the reactivity of rare earth trihalide melts with quartz which results in the formation of oxyhalide at high temperature, the distillation temperature should not exceed 920°C in the case of NdCl_3 . Volatile impurities were trapped at cold end of the quartz tube or cold trap (liquid nitrogen temperature). The distilled halides were transferred over the gap of the quartz reservoir. The typical distillation took 3 hrs. At the residue part (left side of quartz reservoir) oxyhalide was formed in spite of careful temperature control. The distilled NdCl_3 was carefully separated from the quartz reservoir under Ar atmosphere and stored in a glass ampoule which was sealed under vacuum, as described before.

In the case of neodymium triiodide the salt was prepared by direct reaction of the metal with iodine vapour by modified method of Druding and Corbett at the university described above [Druding61, Bogacz99, Rycerz02], namely from iodine gas (POCH Gliwice, Poland, reagent grade) and Nd metal which was obtained by metallothermic reduction of NdCl_3 (99.99%, Wroclaw) with Ca (99.999%). The details are described in the literatures cited above.

The dihalides were synthesised by reacting the proper amounts of metal and trihalide in Ta or Mo crucibles at ca. 900°C for 4 hrs.

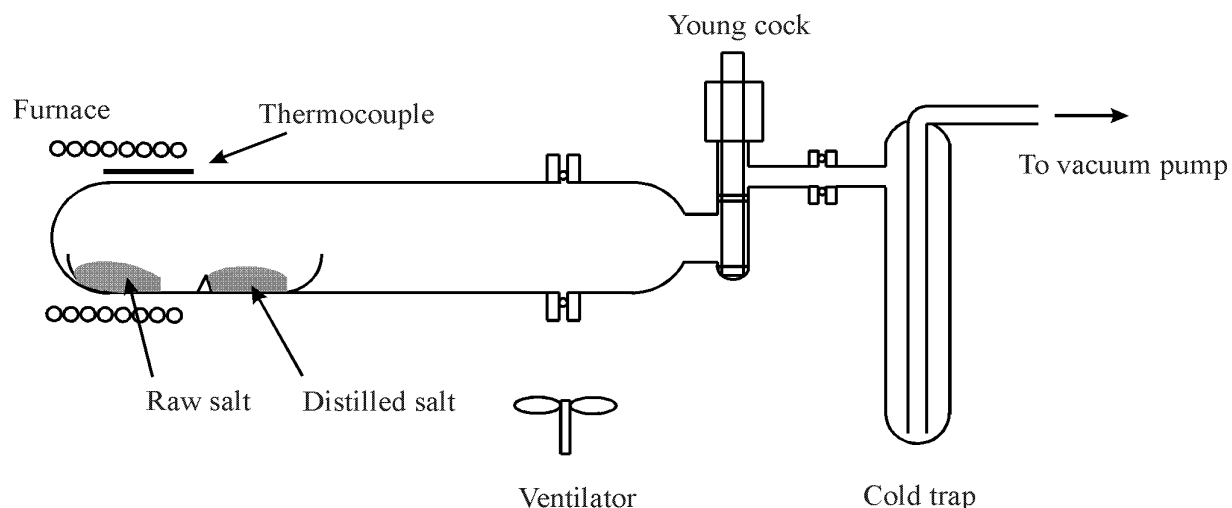


Fig. 3.1 Distillation apparatus for rare earth trihalides

3.1.3 Recrystallisation of alkali halides

LiX and KX were dried and recrystallised in a furnace that was connected to a glove box and, therefore, not exposed to the air atmosphere. The purity of the salts is as follows:

LiCl: 99.99 % (Aldrich), KCl: 99.999 % (Alfa), LiI: 99.999 % (Alfa), KI: 99.99 % (Alfa).

Each salt in a glassy carbon crucible (Deutsche Carbon) was first heated to 400 °C under vacuum. After several hours argon gas was introduced inside the furnace and heated slowly up to ca. 50 °C above the melting point of each salt. Finally the furnace was cooled with the rate of 1.5 K/h and the melt crystallised. After this treatment impurities which had gathered at the surface of the crystal could be easily removed mechanically.

3.1.4 Preparation of $\text{LnX}_2\text{-LnX}_3$ – (LiX-KX) eutectic mixtures

The mixtures of $\text{LnX}_2\text{-LnX}_3$ in LiX-KX eutectic were prepared by melting the proper amounts of salt mixtures in quartz ampoules ca. 50 °C above the liquidus line¹ for about one hour. After cleaning with ethanol all quartz ampoules were heated in air at ca. 1000 °C for several hours. They were brought to the glove box at high temperature (ca. 300 °C) not to

¹ Liquidus line of $\text{LnX}_3\text{-(LiX-KX)}_{\text{eut}}$. For their phase diagrams, see Appendix 1. There are no phase diagram studies existing for the $\text{LnX}_2\text{-LnX}_3\text{-(LiX-KX)}_{\text{eut}}$ systems, so that the melting point depression can only be estimated from the colligative properties of the mixture.

absorb water. After the proper amount of salts was introduced into the tube, it was closed with a Young stop cock, then sealed after evacuation and heated with a furnace. The polycrystalline mixture was then brought again into the glove box, and finely powdered with a mortar. A slight corrosion of the ampoules was found for higher compositions of rare earth dichlorides, whose product was identified by XRD measurement as silicon oxichloride [Hayashi01].

3.2 Spectroscopic techniques

3.2.1 UV-VIS Spectrometer

The reflectivity and absorption spectra were measured with a Cary-AVIV 17 H spectrophotometer (AVIV) in the wavelength range from 250 to 2500 nm, corresponding to 5 to 0.5 eV. The spectrometer and spectra recording system are constructed in a way especially suitable for high temperature measurements. Detailed descriptions are found in [Freyland84, Nattland93, Blanckenhagen97].

The arrangement of the optical component is as follows:

Halogen lamp → Sample → Monochromater → Detector.

This has the advantage that all black body radiation does not come into the detector [Gruen64]. As a light source, a 250 Watt tungsten halogen lamp was used for VIS and NIR range, and a 110 Watt deuterium lamp for UV range. The monochromater is a prism-diffraction grating double monochromater for the wavelength from 185 to 3000 nm with the best resolution of 0.1 nm in the VIS range and 0.3 nm in the IR range. Two kinds of detectors were used, namely a photomultiplier tube (250 – 870 nm) and a PbS detector (870 - 2500 nm). The whole spectrum recording was controlled with a personal computer.

3.2.2 High temperature reflectivity set-up

As mentioned above, only Mo, Ta, or glassy carbon can be considered as suitable materials for the sample reservoir due to highly corrosive properties of the rare earth metal – rare earth halide melts. A cell compartment for reflectivity measurements has been specially constructed in order to avoid the direct contact of melts and window materials. The schematic cell construction is shown in Fig 3.2. In the present study quartz was chosen as a window

material, since it has a lower thermal conductivity than that of sapphire. The quartz rod (diameter 20 mm, length 80 mm, QGTH) was mounted onto the Mo reservoir (Plansee) apart from the melt and sealed with a graphite ring (Goodfellow) by squeezing with Mo screws and a high temperature resistant ATS stainless steel flange (TEW). Before this sealing graphite was pressed in a form to fit the sealing part. If the screws are not pressed uniformly and symmetrically or if the window material is strongly attacked by the vapour phase, then leakage occurs. This can be easily observed by condensation of the salts at the heat shields after the measurements because of their relatively high vapour pressure. A mechanically polished Mo mirror was put on the bottom of the reservoir to enhance the reflection. A small furnace was set close to the end of the window helping to avoid the precipitation of the melts. The temperature was controlled with two PID temperature controllers (Eurotherm), one for the main furnace and the other for the additional heating element.

The calibration of temperature was performed by inserting the thermocouples directly through a boring of the quartz window, which was sealed with glue at the cold end of quartz. This cold end of the window was directly sealed to the flange of the vacuum chamber containing the reflectivity cell by O-ring (See Fig.3.3). This has the advantage to eliminate the multiple reflections of the light beam. Since the O-ring works up to the temperature of ~ 160 °C, the flange was water cooled.

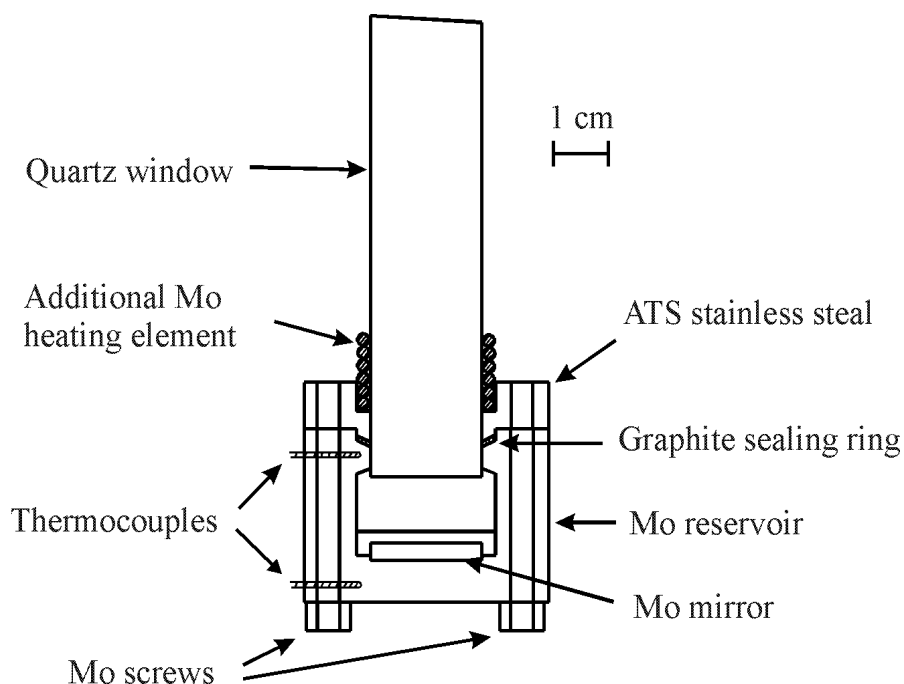


Fig. 3.2 Construction of reflectivity cell

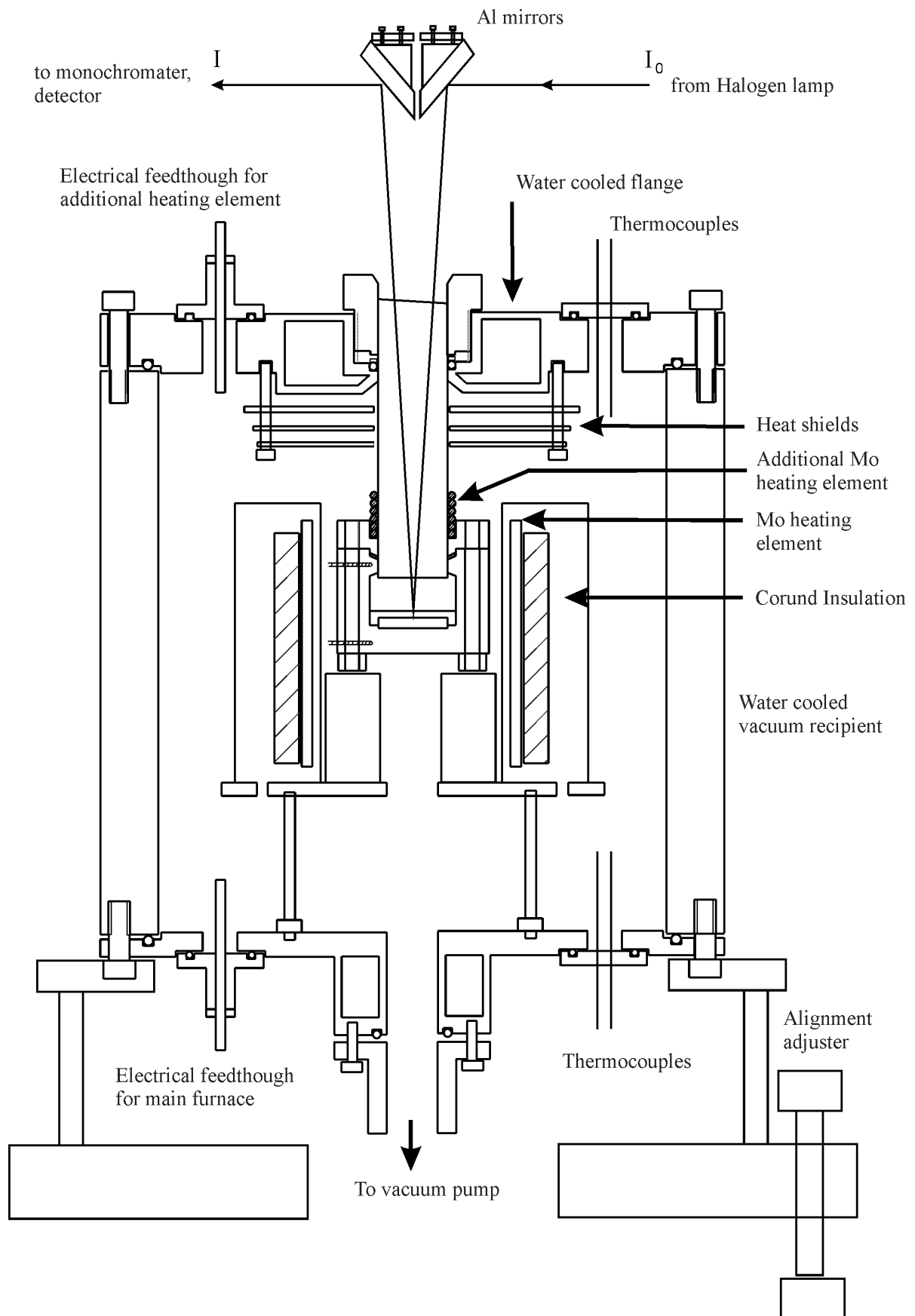


Fig. 3.3 Vacuum chamber for reflectivity measurement

In order to avoid the reflected light from the upper interface of the window coming into the detector, it was inclined ca. 2° to the horizontal, as shown in Fig. 3.2. The influence of the geometry and the contributions from the various interfaces has been calibrated by measuring the reflectivity of the empty cell. The details are given in the data analysis section. Extinction, $\log_{10}(I_0/I_r)$, was recorded as a function of energy, where I_0 is incident beam and I_r is the reflected beam. The overall arrangement of the reflectivity cell inside the vacuum chamber and its alignment in the spectrometer compartment are shown in Fig. 3.3.

3.2.3 Optical absorption cell

Absorption measurements were carried out in an optical cell with sapphire windows for the less corrosive melts, i.e. the $\text{LnX}_2\text{-LnX}_3\text{-(LiX-KX)}_{\text{cut}}$ and $\text{LnI}_2\text{-LnI}_3$ systems. The detailed construction of the cell is displayed in Fig. 3.4 [Freyland84, Bachtler94]. The liquid sample was contained between two optically polished circular sapphire windows, which were sealed by a Ta wire of 50-150 μm diameter (Alfa) or a graphite ring of 100 μm thickness (Goodfellow). The two windows are pressed against each other inside high temperature resistant ATS steel frames, which lead to a final optical path length of ~ 10 and 70 μm . The optical path length was determined at the end of the experiment by determining the sealing ring thickness either by an interference microscope (Carl Zeiss) or by a micrometer screw with an accuracy of $\sim \pm 1 \mu\text{m}$. Temperature was measured through two thermocouples which were attached to the metal frame. The same high temperature vacuum furnace has been used for the absorption measurement as that shown in Fig. 3.3. Two quartz disks served as a window material at the chamber for the incident and outgoing beam.

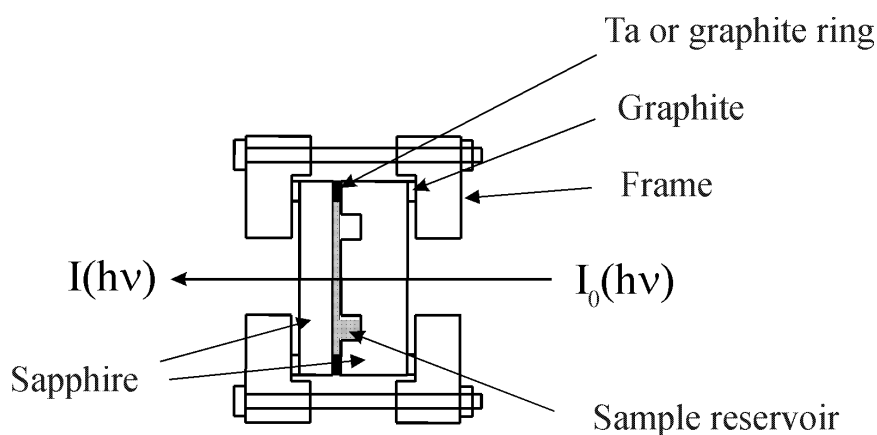


Fig. 3.4 Absorption measurement cell

3.2.4 High temperature ESR set-up

ESR measurements were performed for $\text{LnX}_2\text{-LnX}_3 - (\text{LiX-KX})$ eutectic mixtures with a Bruker B418s X-band (~ 9.3 GHz) spectrometer (Bruker).

The equipment for high temperature measurements was taken over for the present study, which had been specially constructed and developed for the measurements of the alkali metal – alkali halide melts. The details are described in [Schindelbeck95, 96, Poh01]. The schematic diagram is shown in Fig. 3.5.

The sample was put in a quartz capillary of 1.5 mm diameter which fitted into the boring of the sapphire compartment. This construction has the following advantages: 1. Sapphire has a better thermal conductivity than that of quartz, 2. The sample could be sealed vacuum tightly. As shown in Fig. 3.5, the cell part was heated by 44 Watt carbon dioxide laser beam (Melles Griot, $\lambda = 10.6 \mu\text{m}$) from the bottom, focused by the ZnSe lens. Although conventional resistance furnaces (e.g. Pt non-inductive heating element) can also provide the heating of the ESR sample, this technique has the large risk of evaporation of metals or metal oxides from the corresponding heating element and, in particular, the cavity quality factor is strongly reduced. In this respect the heating method with a CO_2 laser has an advantage especially for the ESR measurements of melts where the electrical conductivity is rather high and the quality factor is, consequently, rather low.

In order to avoid the precipitation of the sample at the upper part of quartz capillary, two Mo resistance furnaces outside the cavity were used. Argon gas flow heated with a Mo furnace below the cavity helped the further heating. Another role of the argon gas flow is to protect the metal parts at high temperature from oxidation.

Temperature was measured by a pyrometer focused on the sapphire via the Mo mirror. The temperature gradient along the sapphire was calibrated with an array of thermocouples in an independent experimental run.

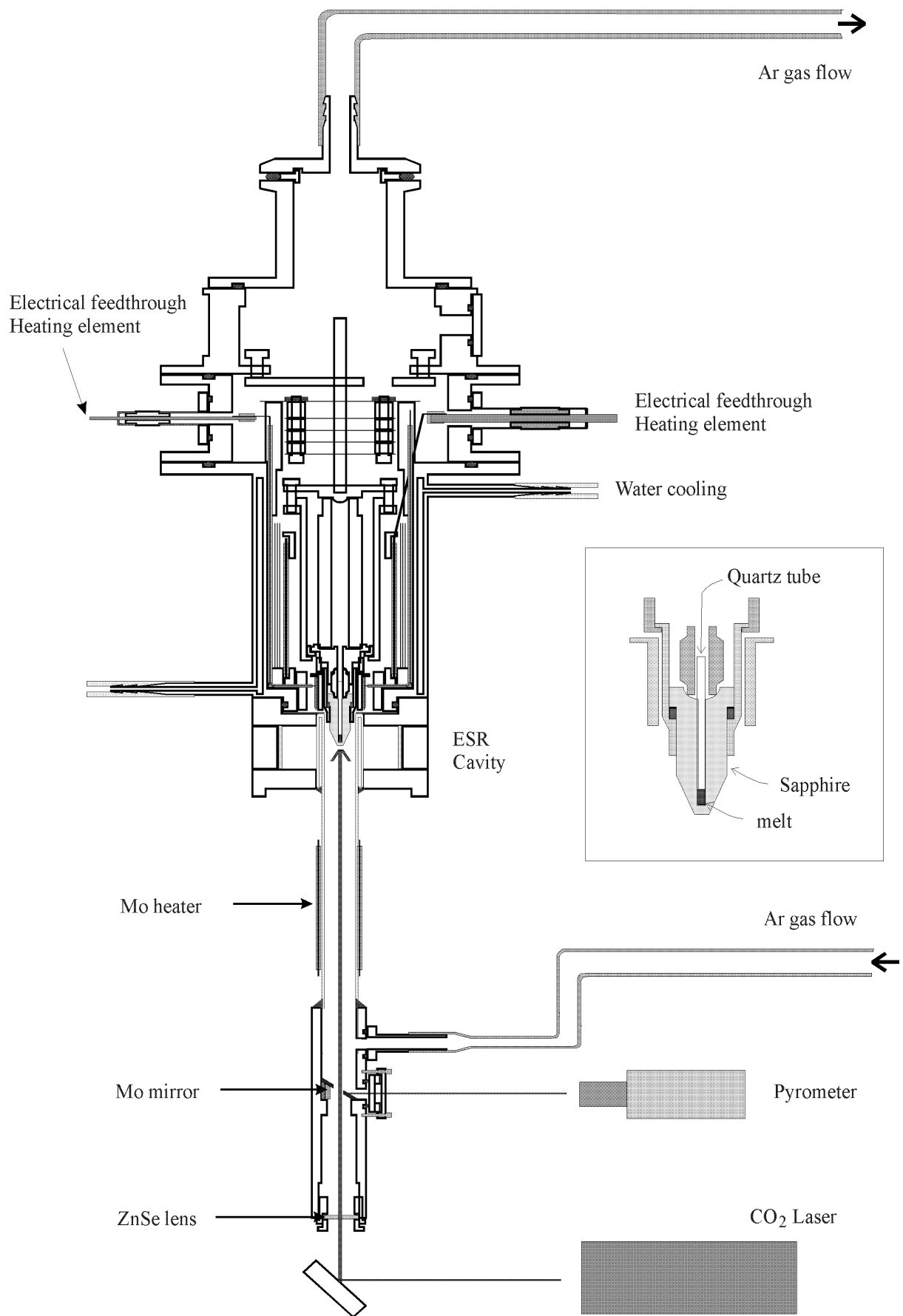


Fig. 3.5 High temperature ESR cavity, sample heating and sample cell construction

3.3 Experimental procedures

3.3.1 Reflectivity measurement

Sample preparation and Cell mounting

Metal parts, which have direct contact with melt, were first cleaned with the mixture of ethanol, benzene and acetone. After drying they were further cleaned by heating in an induction furnace (Hüttinger) up to ~ 1300 °C under vacuum of 10^{-5} mbar, and then transferred to the glove box. Proper amounts of salt and metal were weighed there and filled into the cell. The cell was sealed with Mo cover and heated up to ~ 50 °C above the melting point of the sample for more than 2 hrs under vacuum. This reaction process was done in a furnace inside the glove box.

The quartz window was also cleaned with an alcohol mixture, then heated in air at ~ 1000 °C for several hours. It was cooled down to ~ 300 °C and brought into the glove box immediately.

The window and cell filled with solid sample were carefully mounted by screwing the Mo screws with a torque wrench (torque up to 40 N/m). The position of quartz surface was always kept around 17 mm above the solid sample.

The sealed cell was brought outside the glove box, then the additional heating element was attached and the quartz window was connected to the upper flange of the vacuum chamber. Finally the cell with the upper flange was carefully mounted into the chamber. Electrical contact between the cell and heating element was always checked during the mounting.

Measurement

The additional furnace was heated up to 300 °C in order to produce a definite temperature gradient between sample and window, and subsequently the heating of the main furnace followed. A typical heating rate was 720 K/h. The temperature profile was measured with six Ni-Cr thermocouples, three are set around the additional furnace, two are put into the molybdenum reservoir through borings, one is close to the main furnace. Before the melting point of the sample, the optical alignment was adjusted, which was fixed throughout the measurement run. Then the extinction spectrum, $E(\hbar\omega)=\log_{10}(I_0/I)$, was recorded in the range

$0.5 \leq \hbar\omega / \text{eV} \leq 5$. During the experimental run, the temperature of the window in the cell was always kept above the temperature of the sample compartment (typically 20 °C higher) in order to avoid the condensation of the melt at the window. This condition was maintained on cooling the sample.

3.3.2 Absorption measurement

Preparation

Every cell part was cleaned first with alcohol in an ultrasonic bath. Sapphire windows were further cleaned in the same way as the quartz windows for reflectivity measurements. Ta sealing rings of 50-150 μm diameter were cleaned with acetone carefully, then introduced into the glove box. On the other hand, graphite rings (100 μm thickness) were brought to the glove box without any cleaning treatment.

The weighed salt was carefully introduced into the sample reservoir inside one sapphire window. The salts should be finely powdered and the reservoir part of the cell was completely filled with salts. Otherwise the optical film could not be filled with melt completely. Sealing was done with Mo screws which were tightened symmetrically by a torque wrench in steps of 5 N/m up to 35 N/m.

The chamber was heated at 1000 °C under a vacuum of $\sim 10^{-4}$ mbar prior to measurement in order to get rid of impurities.

Measurement

When the vacuum became better than 2×10^{-5} mbar near the vacuum pump, the furnace was heated to 250 °C. Temperature was measured with Ni-Cr thermocouples at three places (one near the heating element, two thermocouples are attached to the holes of the metal frame). Below the melting point of the sample, an absorption spectrum of the sapphire windows was recorded which was used as a reference spectrum. A typical heating/cooling rate was 600 K/h. In order to examine the temperature gradient along the cell, the temperature of the thermocouples and the extinction at fixed wavelength were recorded as a function of time. At the freezing point of the melt, the extinction shows a sudden jump. In this way the

thermocouples were calibrated for pure or eutectic salts with the corresponding freezing temperatures.

3.3.3 ESR measurement

The cleaning treatment of the quartz capillary was performed in the same way as mentioned above for the optical cell. The capillary with sample powder was evacuated and sealed with hydrogen flame. The outer surface of the glass was cleaned with ethanol, then put into the sapphire cell which had been cleaned with alcohol mixture and heating treatment at ~ 1000 °C. Cell, heat shields and flange were carefully assembled and then introduced into the ESR cavity. Alignment of the cell with respect to the cavity can be monitored by the symmetry of the microwave mode curve. Improper laser radiation alignment causes a large temperature gradient along the sapphire. Prior to each measurement run it was controlled in the following way. A sheet of paper was set on the cavity and the laser spot was controlled with very weak laser radiation. By controlling the Mo mirror adjuster and ZnSe lens, the laser spot should be centered exactly in the middle of the cavity.

Temperature parameters for the CO₂ laser and PID controller were determined from an independent calibration measurement.

Typical experimental settings for recording the ESR spectra have been:

Attenuation of microwave: 25 dB, Modulation amplitude: 5 G, Sweep rate: 1.6 G/s.

4. Experimental details and problems, Data analysis and Error discussion

4.1 Reflectivity measurements

4.1.1 Evaluation of apparent reflectivity

One of the problems in reflectivity measurements is the disturbance by a rather large number of interfaces where the light passes between spectrometer and sample melt. In order to carry out the calibration, the following approximation has been used which considers the detailed light path from light source to detector, and is schematically sketched in Fig. 4.1 for the empty cell. For its description the following symbols are used:

R_{AV} : Reflectivity of Al mirror – Vacuum interface,

R_{QV} : Reflectivity of quartz – vacuum interface,

T_Q : Transmission coefficient of quartz,

R_{VX} : Reflectivity of melt – vacuum interface,

T_X : Transmission coefficient of melt,

R_{XM} : Reflectivity of melt – Mo mirror interface.

We consider first the configuration for the reflectivity of the empty cell (Fig. 4.1). In every reflection from an interface the intensity of the light beam is multiplied by the corresponding reflectivity. The intensity of light, which passes through the quartz window, is multiplied by a non-reflected term of the interface, i.e. $1-R$. For the transmission through the quartz window the beam intensity is attenuated by the factor, T_Q . Attenuation of the whole light pathway yields, finally, the relation between incident beam, I_0 , and the light incoming to the detector, I_{12} , as (I12 model):

$$\frac{I_{12}}{I_0} = R_{AV}^2 (1 - R_{QV})^2 T_Q^2 \{ R_{QV} + (1 - R_{QV})^2 R_{MV} \}. \quad (4.1)$$

From a similar consideration for the reflectivity measurements including the melt (Fig. 4.2) the relation between I_0 and incoming light to the detector, I_{16} , reads (I16 model):

$$\frac{I_{16}}{I_0} = R_{AV}^2 (1 - R_{QV})^2 T_Q^2 \left[R_{QV} + (1 - R_{QV})^2 \left\{ R_{VX} + (1 - R_{VX})^2 T_X^2 R_{XM} \right\} \right], \quad (4.2)$$

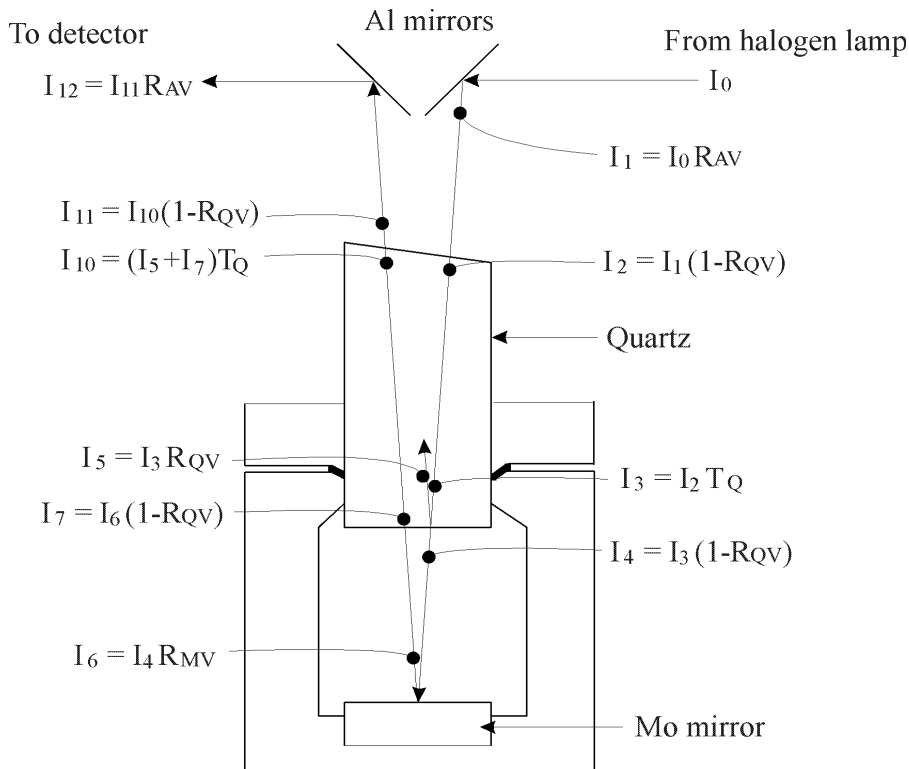


Fig. 4.1 Schematic light pathway through empty reflectivity cell (I12 model).

where the optical constants of the vapour phase in the cell are assumed to be the same as those of air, i.e. $n = 1$, $k = 0$, and multiple reflections in the melt are neglected.

Taking the ratio of (4.1) and (4.2) we have

$$\frac{I_{16}}{I_{12}} = \frac{R_{QV} + (1 - R_{QV})^2 \{R_{VX} + (1 - R_{VX})^2 T_X^2 R_{XM}\}}{R_{QV} + (1 - R_{QV})^2 R_{MV}}. \quad (4.3)$$

The apparent reflectivity, R_X' , can be defined by:

$$R_X' \equiv R_{VX} + (1 - R_{VX})^2 T_X^2 R_{XM}. \quad (4.4)$$

which includes all the contributions from the melt in eqn. (4.3).

The definition of absorbance gives according to eqn. (2.9)

$$\frac{I_{16}}{I_0} = 10^{-A_p(\hbar\omega)} \quad \text{and} \quad \frac{I_{12}}{I_0} = 10^{-A_e(\hbar\omega)}, \quad (4.5)$$

where $A_p(\hbar\omega)$ and $A_e(\hbar\omega)$ are the measured extinctions of sample and empty cell, respectively.

Thus, from eqns. (4.3) – (4.5) the apparent reflectivity is expressed as

$$R_X' = \frac{1}{(1 - R_{QV})^2} \left[10^{-A_p(\hbar\omega) + A_e(\hbar\omega)} \{R_{QV} + (1 - R_{QV})^2 R_{MV}\} - R_{QV} \right]. \quad (4.6)$$

From the literature data of the refractive index and absorption coefficient of quartz and Mo [Palik85, Sopra], the reflectivities R_{QV} and R_{MV} are calculated by

$$R_{QV} = \frac{(n_Q - 1)^2}{(n_Q + 1)^2} \text{ and } R_{MV} = \frac{(n_{Mo} - 1)^2 + k_{Mo}^2}{(n_{Mo} + 1)^2 + k_{Mo}^2}. \quad (4.7)$$

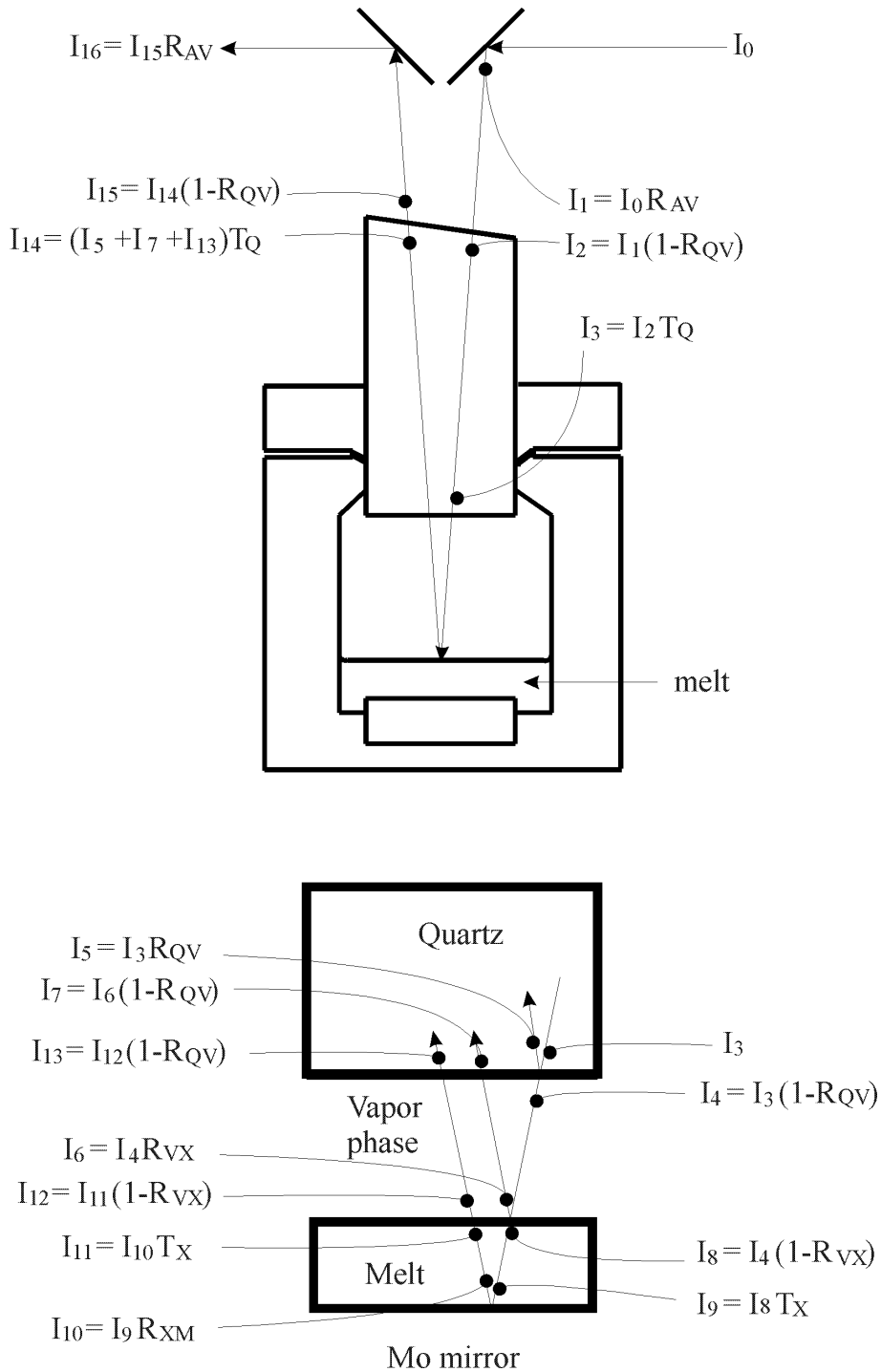


Fig. 4.2 Light pathway through reflectivity cell containing melt (I16 model).

The reflectivity spectrum of the empty cell was measured at room temperature and used as the $A_e(\hbar\omega)$ data set. The apparent reflectivity was calculated accordingly by using eqns. (4.6), (4.7) and experimental data of $A_p(\hbar\omega)$ and $A_e(\hbar\omega)$ for each energy point from 0.5 to 5 eV with the help of a PASCAL program.

As an example, the apparent reflectivity of a NdCl_3 melt is presented in Fig. 4.3. where sharp well resolved peaks of f-f transitions are observed. Peak positions are qualitatively in agreement with those of crystalline NdCl_3 [Sinha66a].

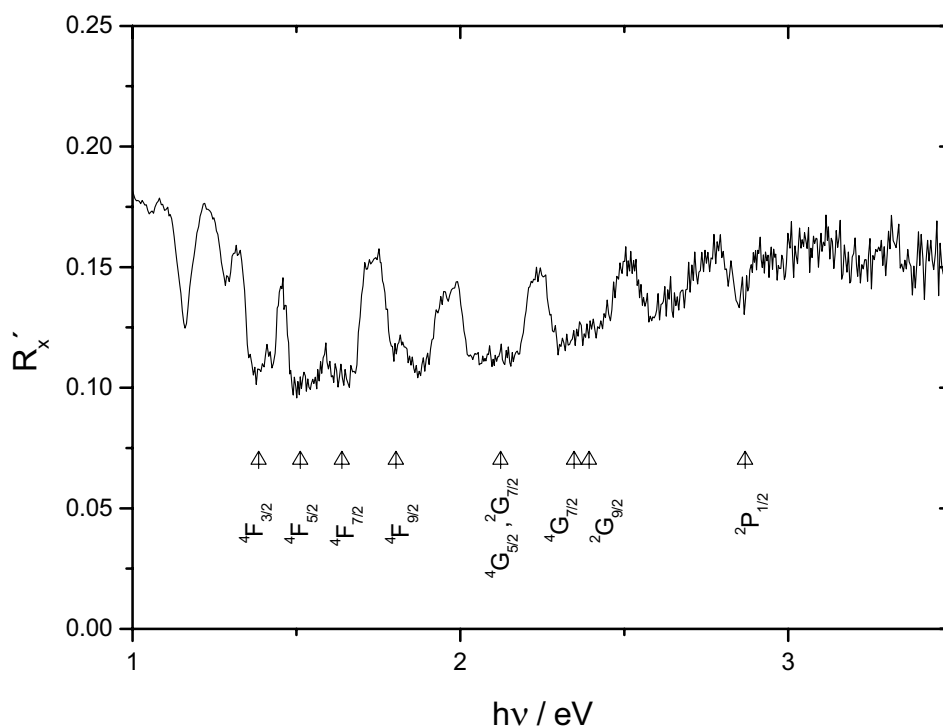


Fig. 4.3 Apparent reflectivity of NdCl_3 melt at 758 °C. Band assignments of excited states from ground state, $^4I_{9/2}$, in Russel-Saunders' notation correspond to literature data of crystalline NdCl_3 [Sinha66a].

4.1.2 Experimental problems and principal restrictions

In the reflectivity cell construction developed here the window material has no direct contact with the sample melt, and so no condensation should occur at the quartz – vapour interface, since the temperature at the window interface was always kept above that at the sample

position. Nevertheless, the following severe experimental restrictions were found for metal doped melts which are presented and analysed in this section in detail.

4.1.2.1 Film formation

In several measurements on metal doped melts it was observed that the quartz window was covered with a thin reflecting film. The film deposits were analysed with electron microscopy¹. The identification of elements is shown in Fig. 4.4.

The approximate composition was estimated as Nd : Cl = 1:3. Since the absolute accuracy of this analysis is rather low and the analysis could not be done for the whole quartz surface region, the film is supposed to have the composition of NdCl_x with $2 \leq x \leq 3$.

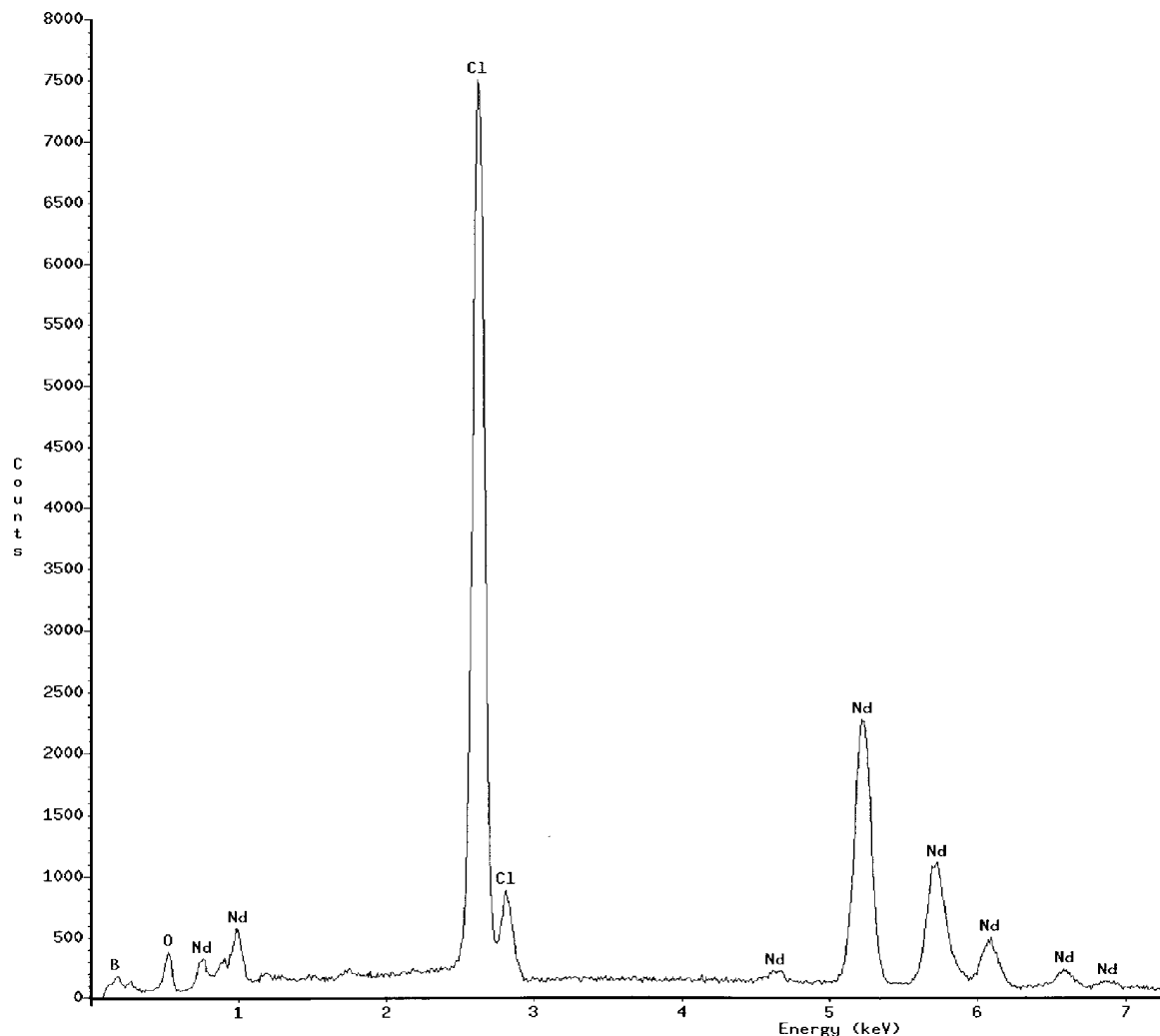
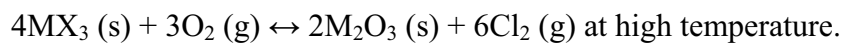
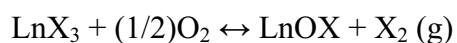
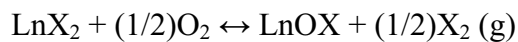


Fig. 4.4 Electron microprobe analysis of a typical film deposits in a Nd-NdCl₃ melt measurement. Each peak was assigned to the element.

¹ Laboratorium für Elektronenmikroskopie, Universität Karlsruhe.

One possible reason for this film formation is an adsorption process between vapour species and quartz substrate, and a consequent corrosion process, i.e. chemical reaction. Another important factor which should be considered is halogen gas formation.

Recent Raman measurements with a window-less cell for Ln-LnX₃ melts showed that reduction by a thermal decomposition process, $\text{LnX}_3 \leftrightarrow \text{LnX}_2 + (1/2)\text{X}_2(\text{g})$, can occur in melt inside a Mo reservoir above 400 °C [Rodriguez B. 00]. Such decomposition has been also reported in DTA measurements which starts above ~ 400 °C for NdCl₃ [Laptev86]. Furthermore, oxidation processes of dihalide or trihalide have to be considered [Gmelin82]:



Although these processes are not known in detail and the level of oxide impurities in the experiments is very low, these reactions may be sufficient to form thin solid films disturbing the reflectivity measurements.

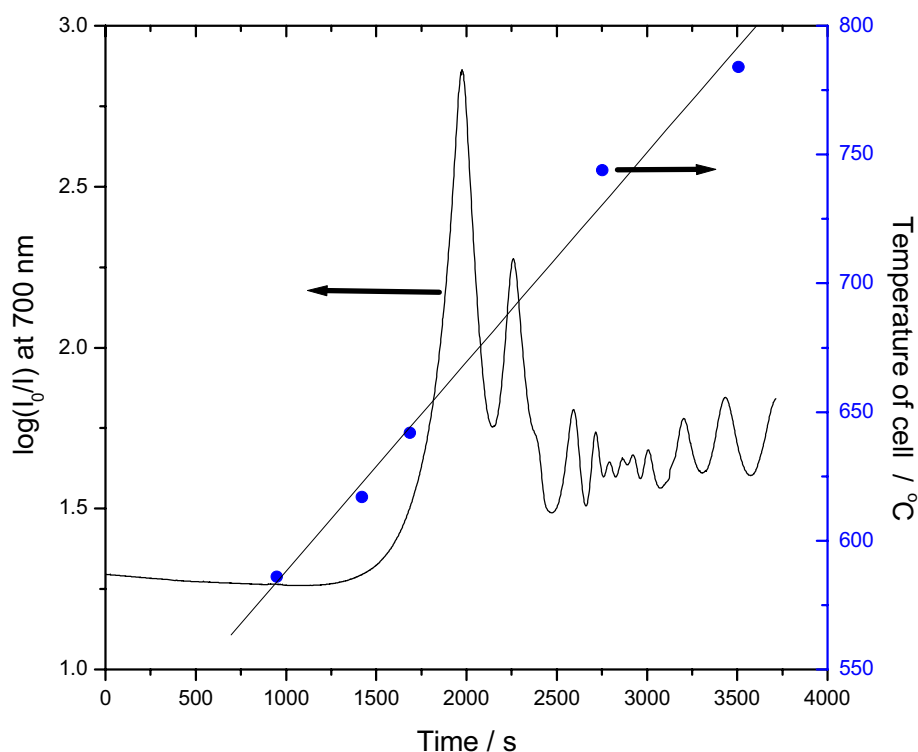


Fig. 4.5 Time variation of the absorbance (corresponding to $\log_{10}(I_0/I_{16})$, see Fig.4.2) at 700 nm and the cell temperature in the measurement of a Nd_{0.01}(NdCl₃)_{0.99} melt.

It is known that chlorine gas attacks quartz at high temperature more rigorously than iodine gas. From the experimental observation in the optical measurements that the corrosion of quartz windows was more pronounced for chloride melts in comparison to iodide melts, the halogen gas seems to play an important role in the chemical reaction and the consequent film formation.

This film formation process could be observed simultaneously with increase of temperature, as displayed in Fig. 4.5. A quasi interference pattern as a function of time at constant wavelength represents the growth of the film at the window – vapour interface. Though the metal concentration is small (1 mol percent), an interesting observation is that this film formation starts at a temperature of about 620 °C (~ 1500 s in Fig. 4.5), which agrees within the error of temperature with the eutectic point of the Nd-NdCl₃ system, i.e. 640 °C [Bredig64].

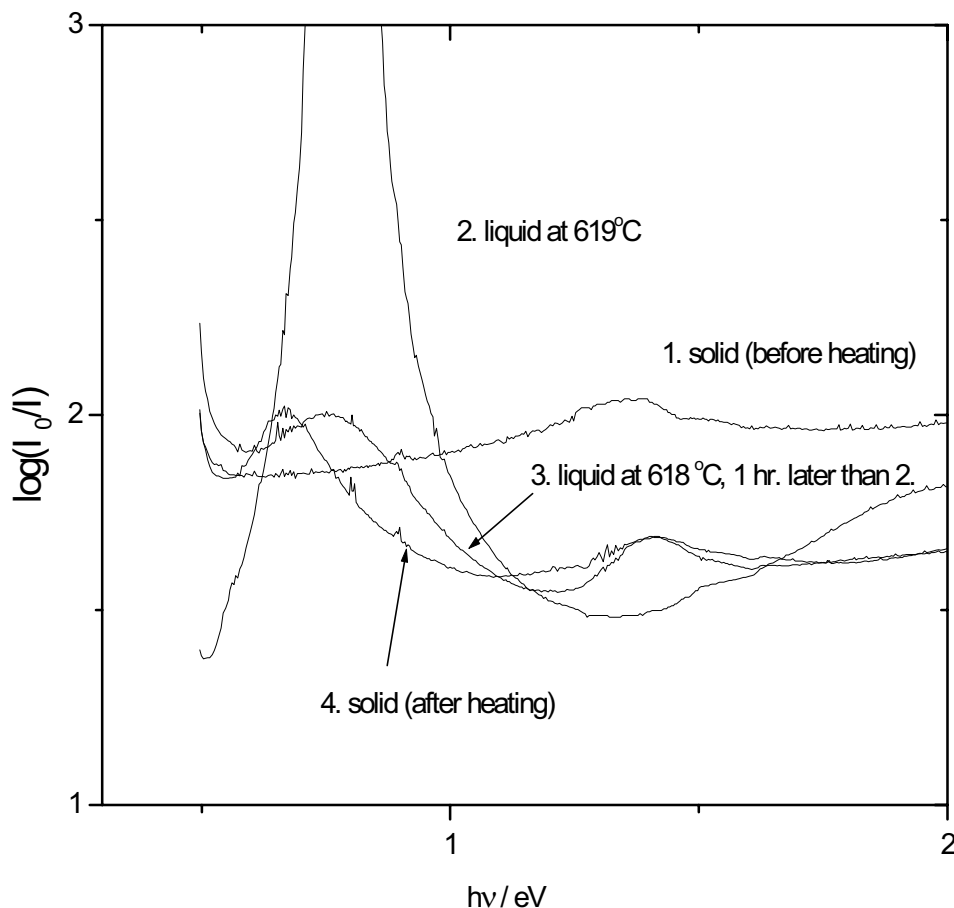


Fig. 4.6 Reflectivity of Nd_{0.23}(NdI₃)_{0.74} melt. Note that the scale is in $\log(I_0/I)$. Because of a continuous film growth the spectra change drastically with time.

When a thin film covers the quartz surface homogeneously, a characteristic interference pattern is observed as a function of energy. An example is shown in Fig. 4.6.

The steady growth of the film causes a large change of the spectra of the liquid phase (at 619 °C) with time (spectra 2 and 3). The spectrum (3) is already similar to the solid-state spectrum (4), i.e. the dominant reflection is due to the quartz – film interface. This can also be seen in the different spectra shape of the solid before and after heating. A detailed analysis of the film contribution, therefore, is required and will be treated in the coming section.

4.1.2.2 Analysis of film spectra

Fig. 4.7 shows the reflectivity solely of a quartz window which was taken at room temperature in air atmosphere after the high temperature measurement of a $\text{Nd}_{0.23}(\text{NdI}_3)_{0.77}$ melt (Fig. 4.6). Because of the thin film thickness a significant interface pattern can be seen in the spectrum. In such an ideal case it is possible to evaluate both the optical constants and film thickness from the three phase interface model sketched in Fig. 4.8. Supposing three phases (quartz-film-air) as shown in Fig. 4.8, the total reflectivity from the quartz – film interface is given in terms of the optical constants, n_i and k_i of i -th phase by [Grosse79]:

$$R = \frac{R_{qf} + R_{fa} \exp(-4k_f k_0 d) - 2\sqrt{R_{qf} R_{fa}} \exp(-2k_f k_0 d) \cos(2n_f k_0 d + \delta_{fa} - \delta_{qf})}{1 + R_{qf} R_{fa} \exp(-4k_f k_0 d) - 2\sqrt{R_{qf} R_{fa}} \exp(-2k_f k_0 d) \cos(2n_f k_0 d + \delta_{fa} + \delta_{qf})}, \quad (4.8)$$

where the R_{qf} and R_{fa} are the reflectivity of the quartz-film interface and film-air interface with phase shift δ_{fa} and δ_{qf} , respectively, i.e.

$$R_{qf} = \frac{(n_q - n_f)^2 + (k_q - k_f)^2}{(n_q + n_f)^2 + (k_q + k_f)^2}, \quad R_{fa} = \frac{(n_f - n_a)^2 + (k_f - k_a)^2}{(n_f + n_a)^2 + (k_f + k_a)^2}. \quad (4.9)$$

It should be noted that multiple reflections are also taken into account in eqn. (4.8).

Assuming $n_a = 1$, $n_q = 1.5$, $k_a = k_q = 0$ and $\delta_{fa} = \delta_{qf} = 0$, the above formula was applied for fitting of the interference pattern in Fig 4.7. The interference pattern (solid line) can be modelled reasonably by this formula (dotted line). The obtained optical constants and thickness are $n_f = 2.9$, $k_f = 0.2$, $d = 0.7 \mu\text{m}$ with an offset parameter 0.6 in the absorbance scale. With these values of the optical constants, the thickness dependence of reflection from the quartz – film interface is simulated with help of eqn. (4.8) in order to examine the influence of the film on the reflectivity of melt where the same window was used. As shown in Fig. 4.9, a strong peak around 0.7 eV of the $\text{Nd}_{0.23}(\text{NdI}_3)_{0.77}$ melt spectra at 619 °C may be explained by this interference effect with a film thickness around 0.3 μm . It is interesting to point out that the first apparent interference peak shifts to lower energies with increasing film

thickness. This trend is also observed in the spectra in Fig. 4.6 at different times, that is the film growth is monitored through reflectivity measurements.

From the above discussion it must be concluded that the film formation has a significant influence on the reflectivity measurements of the present systems, especially for the lower energy range. This effect can hardly be corrected since it involves time dependent processes of both the kinetics of adsorption and chemical reaction. The interpretation of reflectivity data for these systems, therefore, is highly complicated and uncertain.

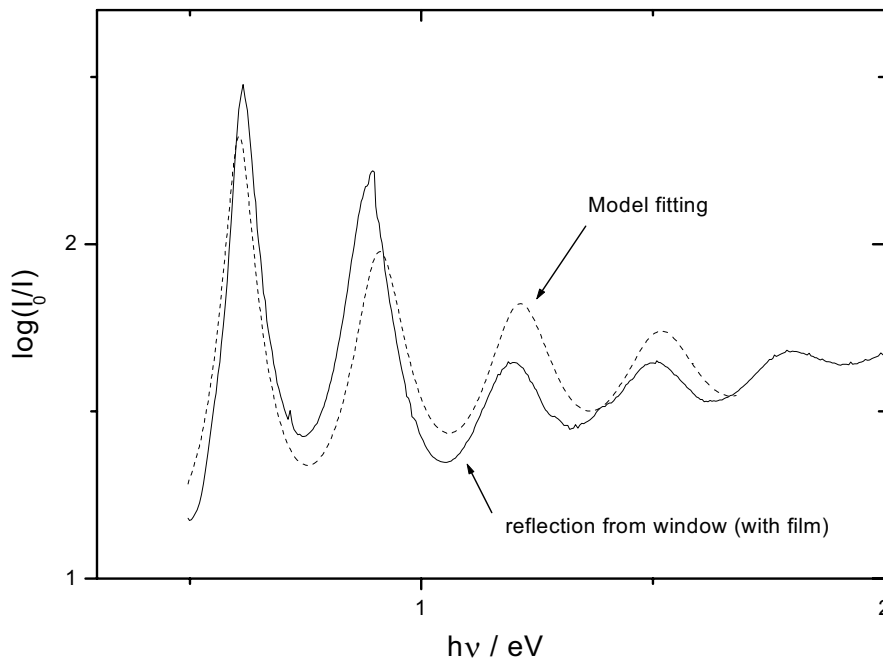


Fig. 4.7. Interference of quartz window with deposited film after the high temperature measurement of a $\text{Nd}_{0.23}(\text{NdI}_3)_{0.77}$ melt (Fig. 4.6). Fitting with interface model (eqn. (4.8)) is also included. For details see text.

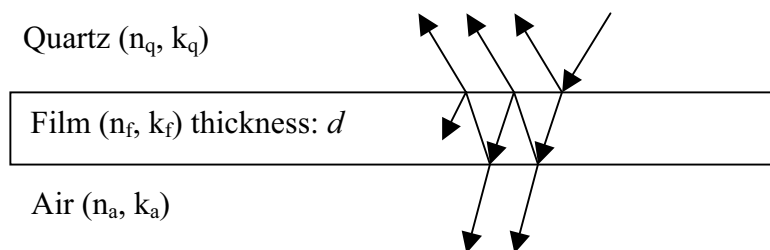


Fig. 4.8 Three phase model of film on quartz window

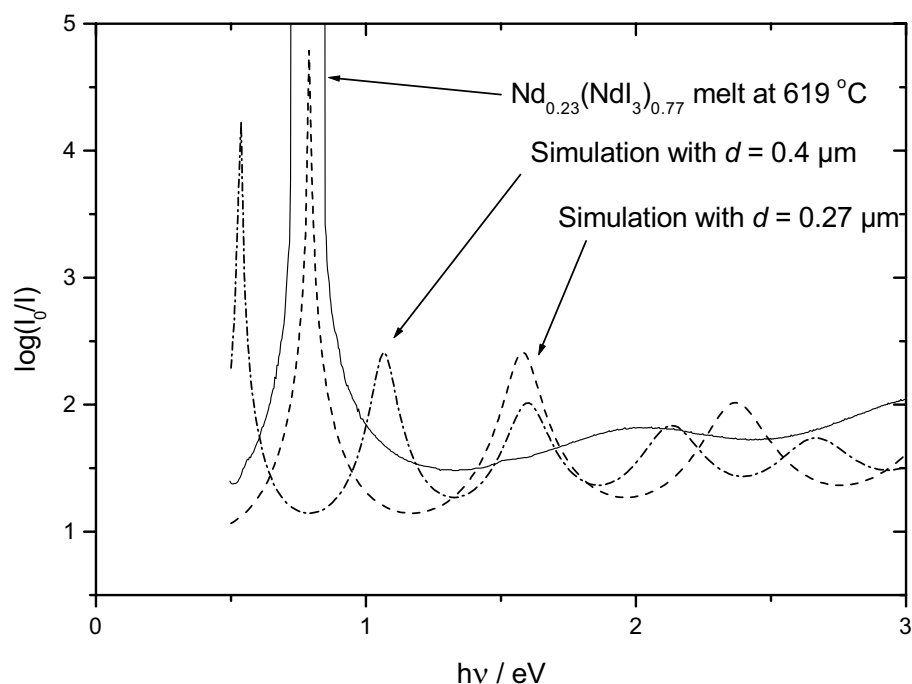


Fig. 4.9 Simulation of the film thickness dependence of the reflectivity from quartz – film interface in absorbance scale. The experimental data (solid line) corresponds to $\text{Nd}_{0.23}(\text{NdI}_3)_{0.77}$ melt at $619\text{ }^\circ\text{C}$ (Fig. 4.6)

4.1.2.3 Metal dissolution in rare earth halide – alkali halide mixtures

Taking into account the shortcomings of the reflectivity measurements on the Ln-LnX_3 melt described above, we tried to escape the high temperature corrosive problems by studying the reflectivity in $\text{Ln-LnX}_3\text{-(LiX-KX)}_{\text{eut}}$ mixtures which have clearly lower eutectic temperatures although the phase diagrams are not known in detail [Janz67]. However, another problem arises with these systems. Though the samples have been prepared by melting the corresponding mixtures prior to high temperature reflectivity measurement, small pieces of metal, in some cases, remained in the melts without complete dissolution, which can be recognized easily after measurements. That means the dissolution process occurs during the spectra recording. Fig. 4.10 shows a selection of reflectivity spectra of $\text{Ce}_{0.005}(\text{CeCl}_3)_{0.09}\text{-(LiCl-KCl)}_{\text{eut}, 0.905}$ melt which are presented on the absorbance scale.

After melting the spectral shape changes drastically within an hour (spectra were recorded at intervals of 13 min from spectrum 2 to 5). A small piece of cerium metal was found remaining in the melt after the measurement. This sequence of spectra shows that it is difficult to assign the spectra to a specific melt concentration and, in addition, to separate the

reflectivity of the continuously forming film deposit. A further difficulty in preparing proper compositions is due to the fact that there are no phase diagram data for $\text{Ln-LnX}_3\text{-(LiX-KX)}_{\text{eut}}$ systems. It should be noted that a similar dissolution problem was found also in electrical conductivity measurements for Ln-LnX_3 melts [Zein El Abedin 00] where the metal solubility limits were established.

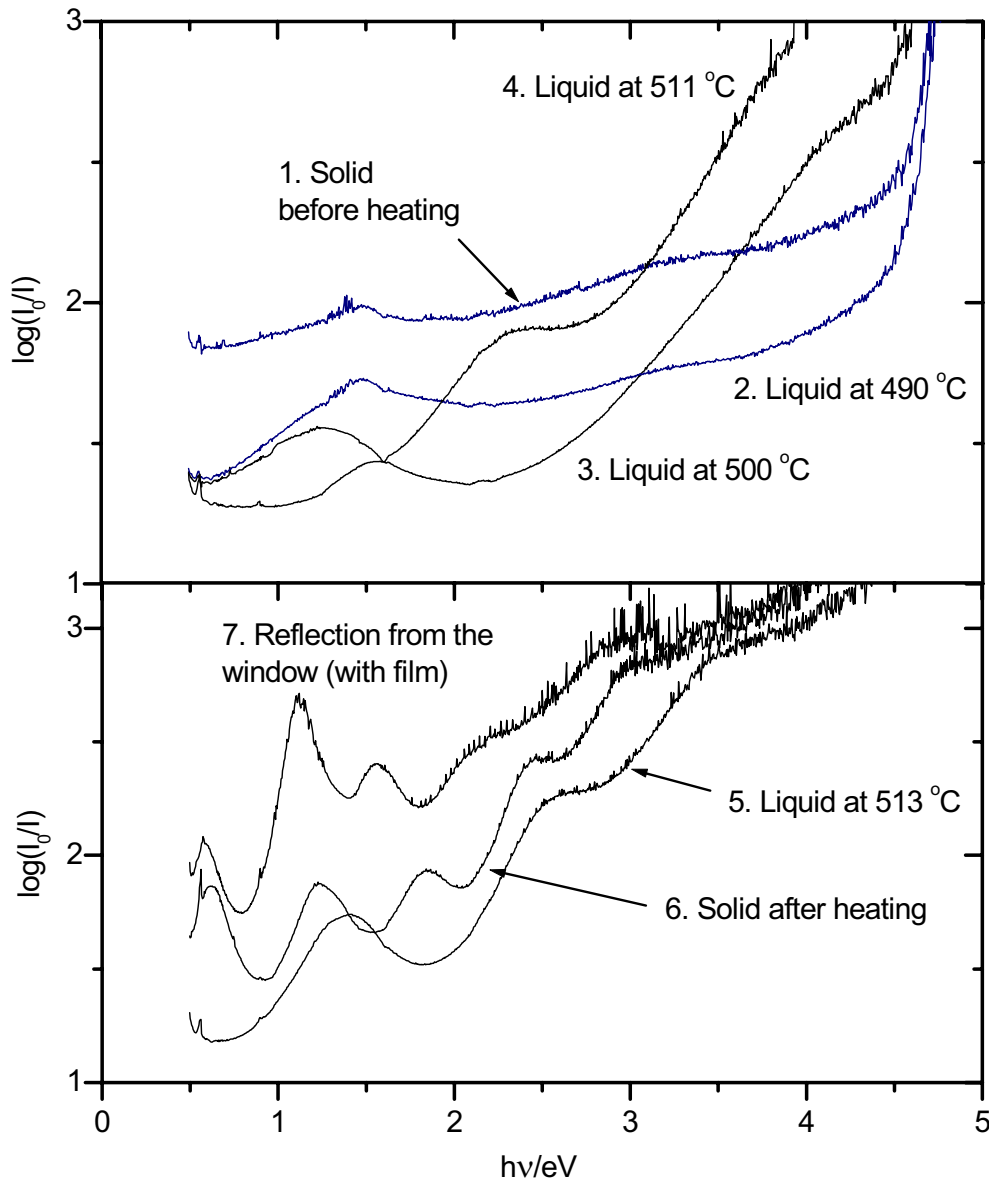


Fig. 4.10 Reflectivity measurement of $\text{Ce}_{0.005}(\text{CeCl}_3)_{0.09}\text{-(LiCl-KCl)}_{\text{eut } 0.905}$ presented on a $\log_{10}(I_0/I)$ scale. The number in the figure gives the sequence of spectra recording. Just after melting (No. 2) the spectra were taken immediately at time interval of 13 min. No. 7 is the reflectivity of the window alone after the high temperature measurement, recorded in air atmosphere at room temperature.

4.2 Absorption measurements

4.2.1 Analysis of absorption measurements

The original absorption spectra recorded in the extinction scale contain not only the contribution from the melt but also from other influences like absorption of sapphire and quartz window at the chamber, and losses of intensity due to reflection at various interfaces. The small cross-section of sample compartment reduces the light beam through the chamber and cell and has to be calibrated. In order to correct these influences, the absorbance of the empty cell measured below the melting point have been subtracted from the sample spectra:

$$A_{\text{cor}}(\hbar\omega) = A_{\text{sample}}(\hbar\omega) - A_{\text{Sapphire}}(\hbar\omega). \quad (4.10)$$

For further analysis, $A_{\text{cor}}(\hbar\omega)$ was converted to the absorption constant according to eqn. (2.9). As an example, Fig. 4.11 shows the absorption constant of a $(\text{NdCl}_2)_{0.02}(\text{NdCl}_3)_{0.02}-(\text{LiCl-KCl})_{\text{eut } 0.96}$ melt at different temperatures and recording times.

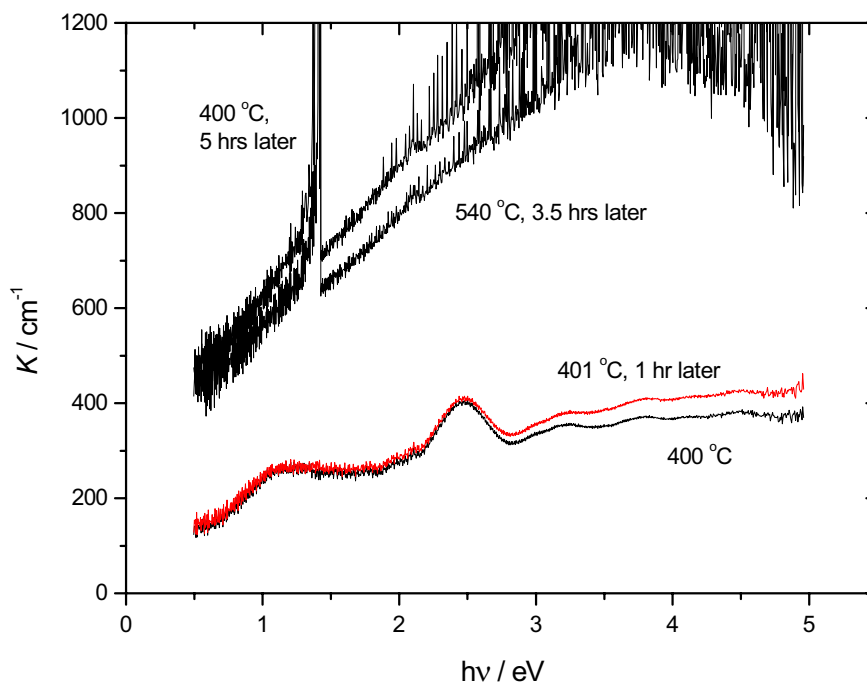


Fig. 4.11 Absorption spectra of $(\text{NdCl}_2)_{0.02}(\text{NdCl}_3)_{0.02}-(\text{LiCl-KCl})_{\text{eut } 0.96}$ melt. The time shown in the figure is the recording time after the first spectrum at 400 °C. The apparently strong absorption around 1.4 eV for the last two spectra (3.5 and 5 hrs later) is due to the switching of detector at 870 nm (See the experimental section). Furthermore, the interference pattern can be recognized typical of the thin liquid film of optical cell (See also Fig. 4.12 and Fig. 5.11).

4.2.2 Experimental problems in absorption measurements of $\text{LnX}_2\text{-LnX}_3\text{-(LiX-KX)}_{\text{eut}}$ melts

Although measurements of the absorption spectra of $\text{LnX}_2\text{-LnX}_3\text{-(LiX-KX)}_{\text{eut}}$ and $\text{LnI}_2\text{-LnI}_3$ melts have been possible (see results and discussion section), the influence of chemical reactions and, consequently, gas formation inside the sapphire cells has to be considered similar to the reflectivity measurements described above. Fig. 4.12 shows the absorption spectra of $(\text{EuCl}_2)_{0.1}(\text{EuCl}_3)_{0.1}\text{-(LiCl-KCl)}_{\text{eut}, 0.8}$. If the cell is not filled completely with absorbing liquid, part of the light can path, so that characteristic but unphysical flat terraces at higher energies occurs where strong absorption of charge transfer bands is expected (Fig. 4.12). In these cases it was observed that small bubbles were distributed homogeneously inside the liquid film and could not be removed by heating or cooling cycles which is an effective method to get rid of inhomogeneous filling due e.g. to impurities on the sapphire windows. Consequently, it has to be concluded that the halide gas is formed inside the absorption cell. As mentioned previously, the following three possibilities are considered:

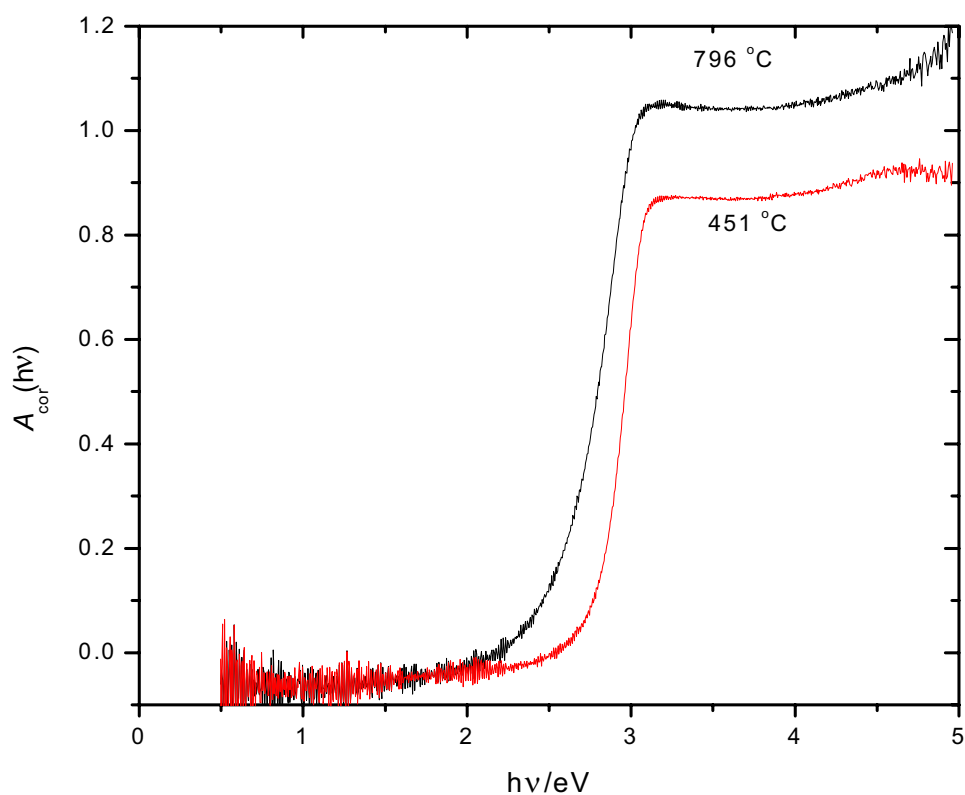


Fig. 4.12 Absorption spectra of $(\text{EuCl}_2)_{0.1}(\text{EuCl}_3)_{0.1}\text{-(LiCl-KCl)}_{\text{eut}, 0.8}$ melt in corrected absorbance scale, see eqn.(4.10).

1. Reaction of the rare earth dihalide with oxygen: $\text{LnX}_2 + (1/2)\text{O}_2 \leftrightarrow \text{LnOX} + (1/2)\text{X}_2 (\text{g})$.
2. Chemical reaction of sapphire and rare earth halides (especially divalent halides).
3. Thermal decomposition of trihalides.

In the case of the europium system, as seen in Table 4.1, thermal decomposition of EuCl_3 may play a dominant role because of the relatively low standard Gibbs free energy change.

For the $(\text{NdCl}_2)_x(\text{NdCl}_3)_y\text{-(LiCl-KCl)}_{\text{eut}, 1-x-y}$ system at longer measuring times intensive and noisy absorption spectra were recorded, indicating a significant contribution of this corrosion effect. Therefore, the measurements for neodymium chloride melts have been carried out within one hour at 400 °C.

For the absorption measurements for the $\text{LnI}_2\text{-LnI}_3$ systems, no significant indication of gas formation has been found except for $\text{CeI}_2\text{-CeI}_3$ melts with high CeI_2 concentrations, which will be presented in the results section. However, the influence of dissolved gas on the recorded spectra cannot be totally excluded, since it is known that iodine gas is well dissolved into molten salts to form polyhalide ions, e.g. I^{3-} , see e.g. [Child83, Nakowsky84].

Table 4.1. Calculated values of standard Gibbs free energy change of the reaction, ΔG_{298}° , [Gmelin82]²: $\text{MX}_3 (\text{s}) \leftrightarrow \text{MX}_2 (\text{s}) + (1/2)\text{X}_2 (\text{g})$.

MCl_3	LaCl_3	CeCl_3	PrCl_3	NdCl_3	PmCl_3	SmCl_3	EuCl_3
ΔG_{298}° (kcal/mol)	153±5	128±7	90±7	77±4	68±10	43±5	21±4

4.3. Error analysis of optical measurements

4.3.1 Instrumental error sources

The main error contributions of spectrometers as given by the manufacturer (AVIV) are summarised here. Accuracy of wavelength is given as ± 0.4 nm, corresponding to an

² See Appendix 1 for formation enthalpy data of LnX_2 and LnX_3 .

uncertainty of the energy scale of 5×10^{-4} eV at 1 - 2 eV. The accuracy of extinction is given as follows:

Extinction A	Error ΔA
0.3	0.001
0.5	0.001
1	0.002
1.5	0.009
2	0.014

4.3.2 Error in absorption measurements

Because of the relatively large dimensions of the optical cell, the temperature gradient from the center to the edge of the sapphire cell is taken as 10 – 15 °C which was observed in the change of the absorbance at freezing point of the melts (see experimental section). An additional error is the deviation of temperature from the mean value measured at different parts of the metal frame that amounts to ± 3 °C.

The most important error contribution in the determination of the absorption constant is the reflection from the sapphire – melt interface. As shown in Fig. 4.11 the corrected absorbance is negative in the lower energy range. Since the refractive index changes on melting of the sample, we have different reflections according to

$$R = \frac{(n - n_s)^2 + k^2}{(n + n_s)^2 + k^2}, \quad (4.11)$$

where n and k are the optical constants in the sample space (argon gas before melting, liquid sample after melting) and n_s is the refractive index of sapphire³.

Since two interfaces of sapphire – melt exist in the absorption cell, the real extinction, A_r , is expressed in terms of R and the measured extinction, A_S , as:

$$A_r = A_S + \log(1-R)^2. \quad (4.12)$$

Neglecting the absorption coefficient in eqn. (4.11), the variation of the second term in eqn. (4.12) for the different media amounts to 100 cm^{-1} in absorption constant, K , where the refractive indices of argon and sapphire are taken as 1.0 and 1.76, respectively [Mallitson62]

³ The absorption coefficient of sapphire is neglected in eqn. (4.11).

and the refractive index of the melt was assumed to be 1.7, typical value of rare earth chloride melts [Iwadate81]. The temperature and frequency dependence of this term have a small effect on the absorbance or absorption constant, so that this is treated as the systematic background offset in the following discussion.

From the instrumental absorbance error and the error in the optical path length the error of absorption constant is given by:

$$\Delta K = \left| \frac{\partial K}{\partial A} \right| \Delta A + \left| \frac{\partial K}{\partial d} \right| \Delta d . \quad (4.13)$$

The error of the optical path length, Δd , was determined from the statistic error of thickness measurement, and lies within 10 %. Thus, the whole relative error of the absorption constant is estimated to be ± 15 %.

4.3.3 Error in reflectivity measurements

As for the error in temperature, a calibration has been performed by measuring the temperatures at different positions, i.e. at the quartz surface in contact with the vapour phase, on the Mo mirror, and 1 mm above the Mo mirror in contact with a caesium iodide melt. The temperature of the quartz surface was always approximately 20 degree higher than that of the melt. In addition to the above temperature gradient, the absolute error in temperature is estimated as ± 5 °C.

As seen in the formula of the apparent reflectivity, eqn. (4.6), the following error contributions should be taken into account: 1. errors in extinction of $A_p(\hbar\omega)$ and $A_e(\hbar\omega)$, 2. errors in reflectivity of R_{QV} and R_{MV} . Besides the photometric error which is described above, it should be taken into account that the reflectivity spectrum of the empty cell was measured separately from those of the melts. The absolute error, which may be caused by the alignment, is taken as 0.01 in extinction units. Errors in the reflectivities, R_{QV} and R_{MV} , can be neglected in comparison with the large contributions above.

Due to the problems in the reflectivity measurements, in particular, the time dependent film formation, a quantitative error estimate is not possible.

4.4 ESR measurements

ESR experiments have been carried out for various mixtures of $(\text{LnX}_2)_x(\text{LnX}_3)_y$ in $(\text{LiX-KX})_{\text{eut}, 1-x-y}$ melts with $\text{Ln}=\text{Ce}, \text{Nd}$ and $\text{X}=\text{Cl}, \text{I}$. In most cases the reproducibility and signal to noise ratio were not sufficient for a quantitative analysis of the spectra. Besides corrosion problems one of the main experimental difficulties was caused by the small sample volume of $\sim 1 \text{ mm}^3$ which is necessary to reduce the temperature and magnetic field inhomogeneity across the sample and to optimise the quality factor inside the cavity. On the other hand, alignment of this small sample inside the cavity is complicated. Further complications are due to creeping of the liquid sample towards the lower temperature end of the quartz capillary and to large composition uncertainties of the given small sample size. This last problem does not exist in high temperature ESR experiments on M-MX melts where the composition has been controlled *in situ* by Coulometric titration [Schindelbeck95, 96].

Finally the errors in ESR measurements are briefly described. Details are found in [Schindelbeck95, Poh01]. As described in the experimental section the temperature gradient was calibrated prior to the high temperature measurement by measuring the temperatures at different heights inside the sapphire cell. The calibration yields an uncertainty of the temperature of $\pm 3 \text{ }^\circ\text{C}$ for the sample with approximately 3 mm height. The absolute error of temperature can be calibrated at the melting point of the salt by monitoring the clear change in the reflected microwave intensity (mode curve) which arises from the dielectric loss of melt with relatively high conductivity compared with solid salt. The total error in temperature is estimated as $\pm 10 \text{ }^\circ\text{C}$.

The statistic error in estimating the half width is $\pm 8 \%$. As mentioned before, the influence of halogen gas plays crucial role in $\text{LnX}_2\text{-LnX}_3\text{-(LiX-KX)}_{\text{eut}}$ melts, so that a quantitative absolute error estimate is not possible.

5. Results

In this chapter the results of both optical and ESR measurements are presented for the systems summarised in the following table. All the original data are saved in a CD-ROM which is available from Prof. W. Freyland in the Institute of Physical Chemistry, University of Karlsruhe.

Reflectivity measurements	(Presented in Chapt. 5.1)
$\text{Nd}_x(\text{NdCl}_3)_{1-x}$ melts	(Chapt. 5.1.1)
$\text{Ce}_x(\text{CeCl}_3)_y\text{-(LiCl-KCl)}_{\text{eut}, 1-x-y}$ melts	(Chapt. 5.1.2)
Absorption measurements	
The $(\text{LnCl}_2)_x(\text{LnCl}_3)_y\text{-(LiCl-KCl)}_{\text{eut}, 1-x-y}$ systems	(Chapt. 5.2)
$(\text{NdCl}_2)_x(\text{NdCl}_3)_y\text{-(LiCl-KCl)}_{\text{eut}, 1-x-y}$ melts	(Chapt. 5.2.1)
$(\text{EuCl}_2)_x(\text{EuCl}_3)_y\text{-(LiCl-KCl)}_{\text{eut}, 1-x-y}$ melts	(Chapt. 5.2.2)
The $(\text{LnI}_2)_x(\text{LnI}_3)_y\text{-(LiI-KI)}_{\text{eut}, 1-x-y}$ systems (Ln=Nd and Ce)	(Chapt. 5.3)
The $(\text{LnI}_2)_x(\text{LnI}_3)_{1-x}$ systems	(Chapt. 5.4)
$(\text{NdI}_2)_x(\text{NdI}_3)_{1-x}$ melts	(Chapt. 5.4.1)
$(\text{CeI}_2)_x(\text{CeI}_3)_{1-x}$ melts	(Chapt. 5.4.2)
ESR measurement	
$(\text{NdCl}_2)_{0.02}(\text{NdCl}_3)_{0.02}\text{-(LiCl-KCl)}_{\text{eut}, 0.96}$ melt	(Chapt. 5.5)

5.1 Reflectivity measurements

In this section reflectivity data of $\text{Nd}_x(\text{NdCl}_3)_{1-x}$ and $\text{Ce}_x(\text{CeCl}_3)_y\text{-(LiCl-KCl)}_{\text{eut}, 1-x-y}$ melts are presented. It should be emphasised that, as discussed in the previous chapter, an overlap of the reflectivity spectra by interference patterns cannot be excluded so that interpretation of the spectra is not straightforward.

5.1.1 $\text{Nd}_x(\text{NdCl}_3)_{1-x}$ melts

Fig. 5.1 shows the apparent reflectivity spectra of $\text{Nd}_x(\text{NdCl}_3)_{1-x}$ melts which have been evaluated according to the scheme described in chapt. 4.1. Broad bands have been observed around 1.5 eV and towards the NIR end for the metal doped samples, while the apparent reflectivity of pure NdCl_3 melt shows only characteristic weak and sharp intra 4f excitations from the $^4I_{9/2}$ ground state (Fig. 4.3). Comparing the band at ~ 1.5 eV with the polaron band of solid mixed valence compounds such as EuCl_x with a band energy of ~ 2 eV [Lange92], this excitation may be attributed to the intervalence charge transfer band. The band at lower energy may be due to the formation of a film as described in section 4.1.2. Its interpretation is still unclear yet.

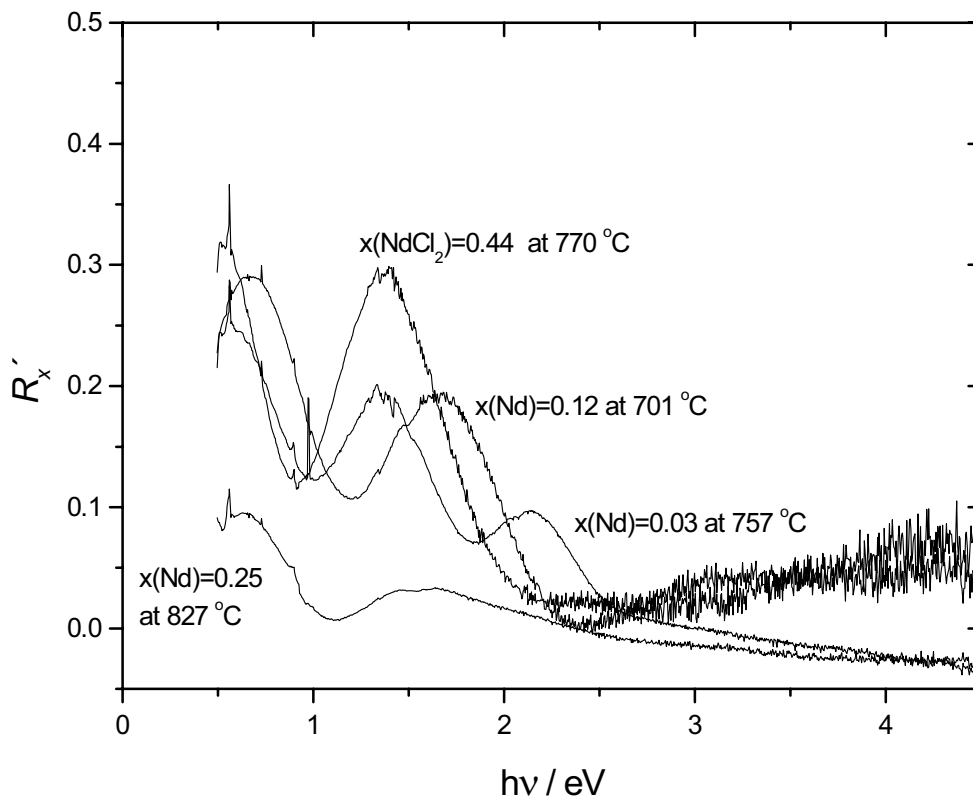


Fig. 5.1 Apparent reflectivity of $\text{Nd}_x(\text{NdCl}_3)_{1-x}$ melt with different composition and temperature.

5.1.2 $\text{Ce}_x(\text{CeCl}_3)_y\text{-(LiCl-KCl)}_{\text{eut}, 1-x-y}$ melts

Optical studies of the lighter rare earth metal – halide system, i.e. the La and Ce systems, should give insight into the differences in the electronic structure within the rare earth series. Reflectivity measurements for Ce-CeCl₃ melts, however, have not been successful in obtaining the necessary information due to horrible corrosion of the quartz windows used. Thus, only results for $\text{Ce}_x(\text{CeCl}_3)_y\text{-(LiCl-KCl)}_{\text{eut}, 1-x-y}$ melts have been obtained which are presented in Fig. 5.2. The apparent reflectivity has been evaluated and presented here for the spectra recorded just after melting, e.g. spectrum 3 in Fig. 4.13 for $x = 0.005$. The interference effect arising from the film formation can be seen in the lower energy range (< 1 eV) in the spectrum and a physically meaningless reflectivity, i.e. $R_x' < 0$, was obtained in the higher energies for $x = 0.01$. The interpretation of the concentration dependence of the spectra is rather uncertain, since the dissolution process of metal should play a crucial role as mentioned in chapt. 4.1.2 (Fig. 4.10). However, it is interesting that the relative intensity of the band towards the NIR seems to increase with increasing Ce metal concentration.

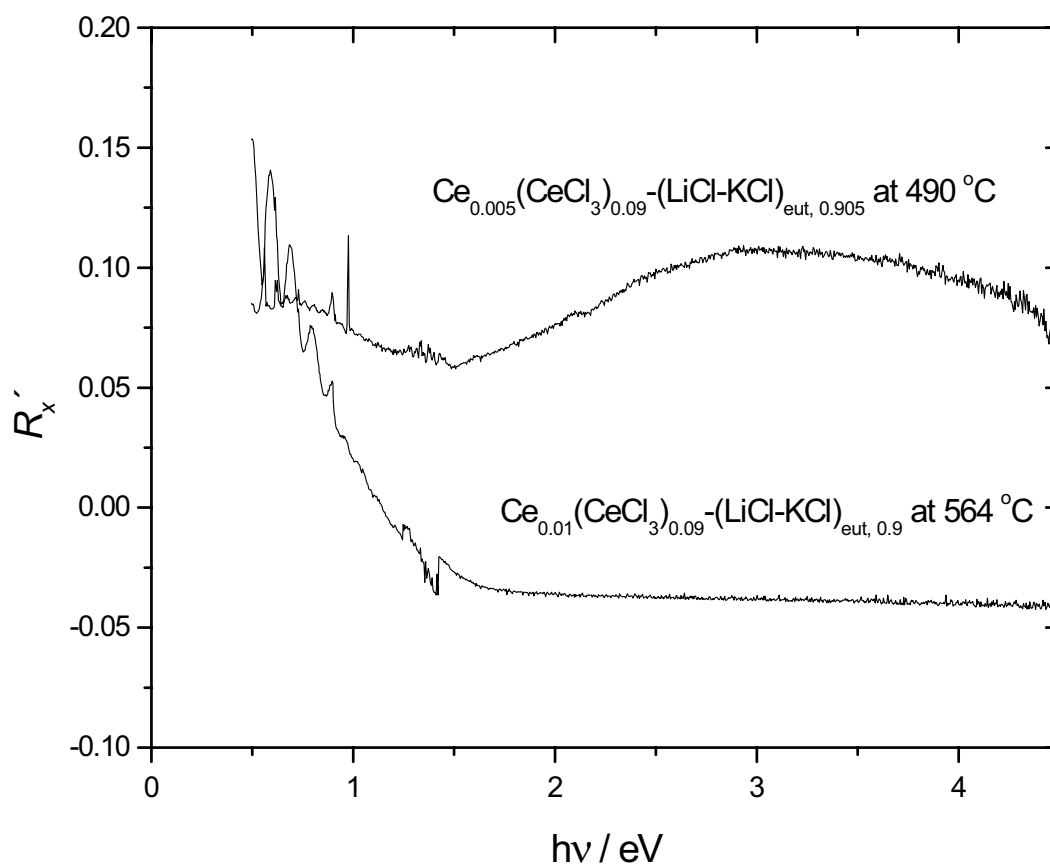


Fig. 5.2 Apparent reflectivity of $\text{Ce}_x(\text{CeCl}_3)_y\text{-(LiCl-KCl)}_{\text{eut}, 1-x-y}$ melts. For $x = 0.005$ the spectrum 3 in Fig. 4.13 was converted to the R_x' .

This might be related with the increase of a free electron like Drude term contributing more significantly to the spectra with increase of Ce metal concentration, which is in agreement with the monotonous increase of the electrical conductivity with metal composition for Ce-CeCl₃ melts [Bredig64]. However, for the systems with low mobility the Drude term contributes only as a flat absorption, e.g. in the optical spectra of low metal concentration of M-MX melts where the mobility is of the order of 0.1 cm² V⁻¹ s⁻¹ [Nattland93] – see also section 6.3.2.

5.2 Absorption measurements of (LnCl₂)_x(LnCl₃)_y-(LiCl-KCl)_{eut, 1-x-y} melts

5.2.1 (NdCl₂)_x(NdCl₃)_y-(LiCl-KCl)_{eut, 1-x-y} melts

The absorption spectra of (NdCl₂)_x(NdCl₃)_y-(LiCl-KCl)_{eut, 1-x-y} melt at 400 °C are shown in Fig. 5.3. For comparison the literature data of the optical absorption spectra of divalent neodymium ion in different matrices are presented in Fig. 5.4.

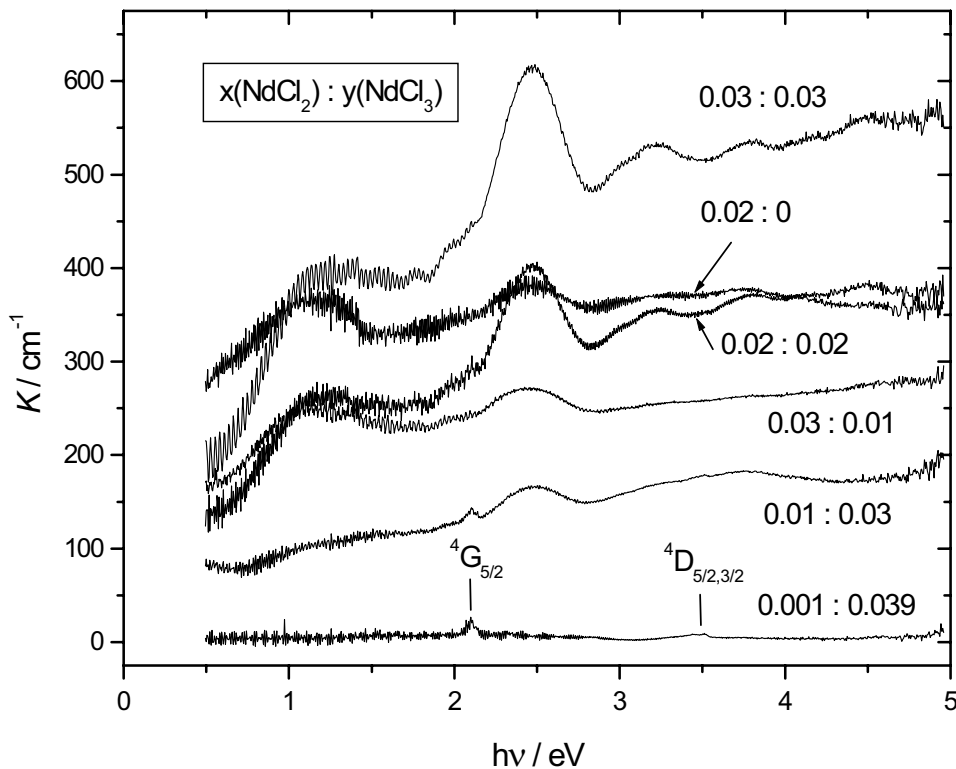


Fig. 5.3 Absorption spectra of (NdCl₂)_x(NdCl₃)_y-(LiCl-KCl)_{eut, 1-x-y} melts at 400 °C. The spectrum of $x = 0.001$ is shifted 0.05 upward in absorbance unit, corresponding to ~ 20 cm⁻¹. Two excited states of f-f transitions (~ 2.1 and 3.5 eV) are assigned and shown with Russel Saunders' notation.

Except for the measurement of the melt with $x(\text{NdCl}_2) = y(\text{NdCl}_3) = 0.03$ cells were not filled completely with sample melts, so that the absolute value of absorption constant must be determined with different constant backgrounds so that an absolute comparison of different spectra is uncertain. On the other hand, further discussion of the relative intensity of the spectrum shape in one spectrum is possible.

As seen in Fig 5.3, the spectra are characterised by sharp, weak f-f transitions around 2.1 and 3.5 eV and broad f-d bands with strong intensity. As has been discussed for reflectivity data of pure NdCl_3 (Fig. 4.3), both f-f bands are assigned as $^4I_{9/2} \rightarrow ^4G_{5/2}$ (2.1 eV) and the $^4D_{5/2,3/2}$ (3.5 eV), respectively. The former, especially, is known as hypersensitive transition of the Nd^{3+} ion [Boghosian96]. With increasing dichloride concentration, the f-d bands become clearly visible, whose peak positions are in fair agreement with those of NdI_2 in THF solution [Kamenskaya83] (Fig. 5.4). An interesting observation is that the excitation around 2.5 eV has maximum intensity at the composition of $x(\text{NdCl}_2) : y(\text{NdCl}_3) = 1 : 1$.

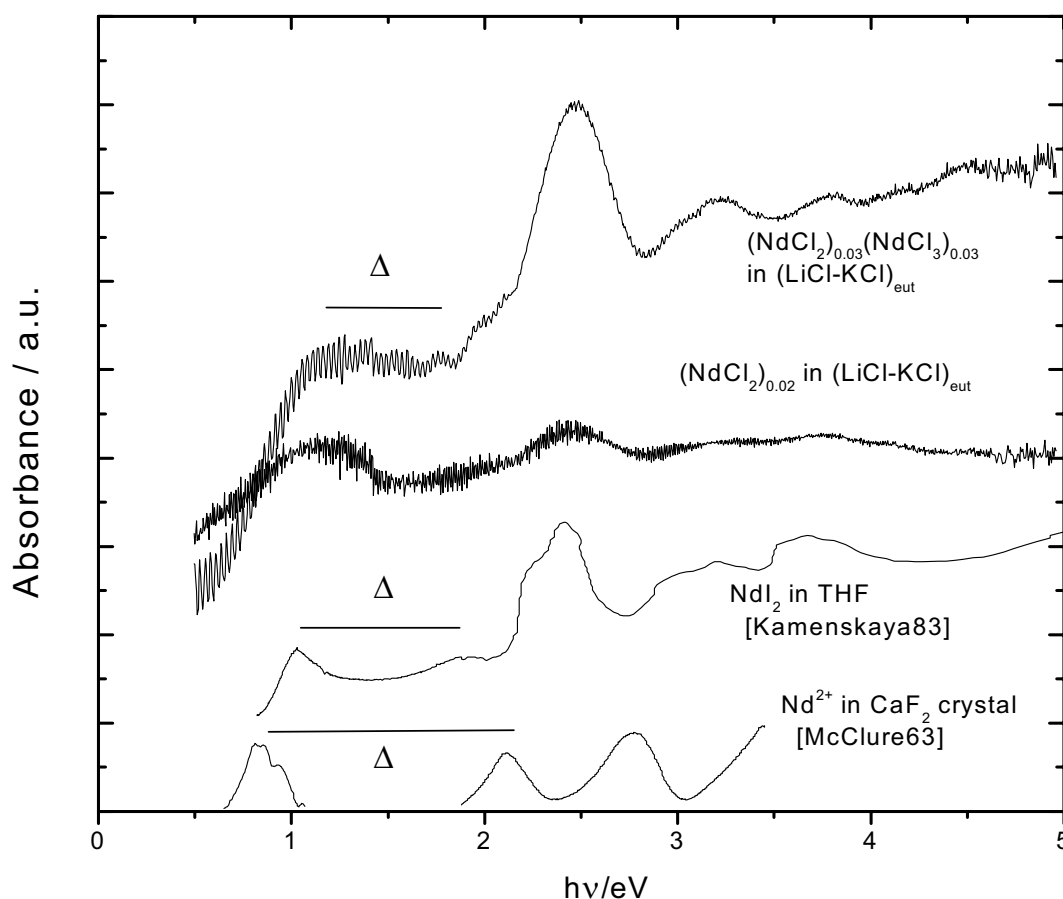


Fig. 5.4 Comparison of literature data of optical absorption spectra of divalent neodymium ion in different matrix. The symbol, Δ , is ligand field strength for Nd^{2+} ion, elucidated from the possible energy level diagram for the ion (See Fig. 5.5).

The possibility of an electron exchange between Nd^{2+} and Nd^{3+} is proportional to the product of mole fraction of the constituting ions, i.e. $x(\text{Nd}^{2+}) \cdot y(\text{Nd}^{3+})$. This can explain the maximum intensity at this composition. Since intervalence charge transfer (IVCT) bands sometimes overlap with the excitation of the constituent ions, e.g. intra d-d transitions [Hush67], this observation indicates that this excitation corresponds to the intervalence charge transfer band in the present system.

It should be also noted that the half-oxidation time of Nd^{2+} in THF is ~ 20 minutes [Kamenskaya83], so that we cannot conclude the absorption band around 2.5 eV is intrinsic excitation of divalent Nd. For the analysis of the optical spectra of divalent rare earth ions in CaF_2 crystal, Johnson and Sandoe applied the $J\Gamma$ coupling scheme to evaluate the ligand field strength, Δ , of the excited 5d state. In this scheme the Russel Saunders (LS) coupled configuration of the $4f^{N-1}$ core is associated with the 5d levels in a ligand field with cubic symmetry [Johnson69a]. This treatment was further adapted to analyse the optical spectra of divalent rare earth ions in solutions¹ [Kamenskaya83]. The schematic energy diagram is shown in Fig. 5.5.

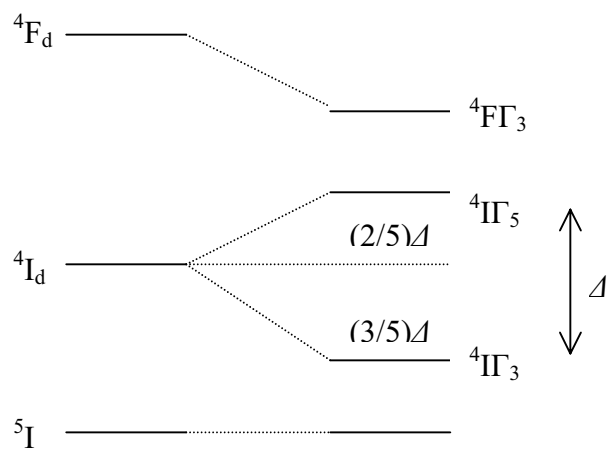


Fig. 5.5. Proposed energy level diagram for the Nd^{2+} ion in calcium fluoride after Johnson *et al.* [Johnson69a] where the levels on the left side give the spin orbit splitting of f and d levels and those on the right hand side are the energy levels for which ligand field splitting is taken into account. The meaning of symbols is: Δ is the ligand field splitting parameter, Γ_3 and Γ_5 are the 5d levels in cubic ligand field.

¹ Though rare earth complex may not have cubic symmetry in solutions, Kamenskaya *et al.* concluded that ligand field parameters by this scheme are rather well in agreement with those estimated from other f-d excitations [Kamenskaya83].

In the framework of this scheme ligand field splitting parameter corresponds to the difference of first and second peak positions of f-d transitions which are shown in Fig. 5.4.

Rough estimate of Δ yields 0.6 eV for the $(\text{NdCl}_2)_x(\text{NdCl}_3)_y(\text{LiCl-KCl})_{\text{eut}, 1-x-y}$ melt. In comparison to the other systems (1.2 and 0.87 eV in CaF_2 crystal and THF solution, respectively) the small value of Δ in the present system may reflect the less coupling between the central rare earth ion and the surrounding chlorine anions.

5.2.2 $(\text{EuCl}_2)_x(\text{EuCl}_3)_y(\text{LiCl-KCl})_{\text{eut}, 1-x-y}$ melts

In all the experiments of the absorption spectra of the europium chloride system the optical cell could not be filled completely with sample melts, giving rise to an apparent “terrace” in the spectra at high absorption constants (See chapter 4). This is clearly seen in the higher energy range in Fig. 5.6. The spectra are characterised by a strong absorption towards the UV range, and there is no significant excitation found in the NIR or VIS range.

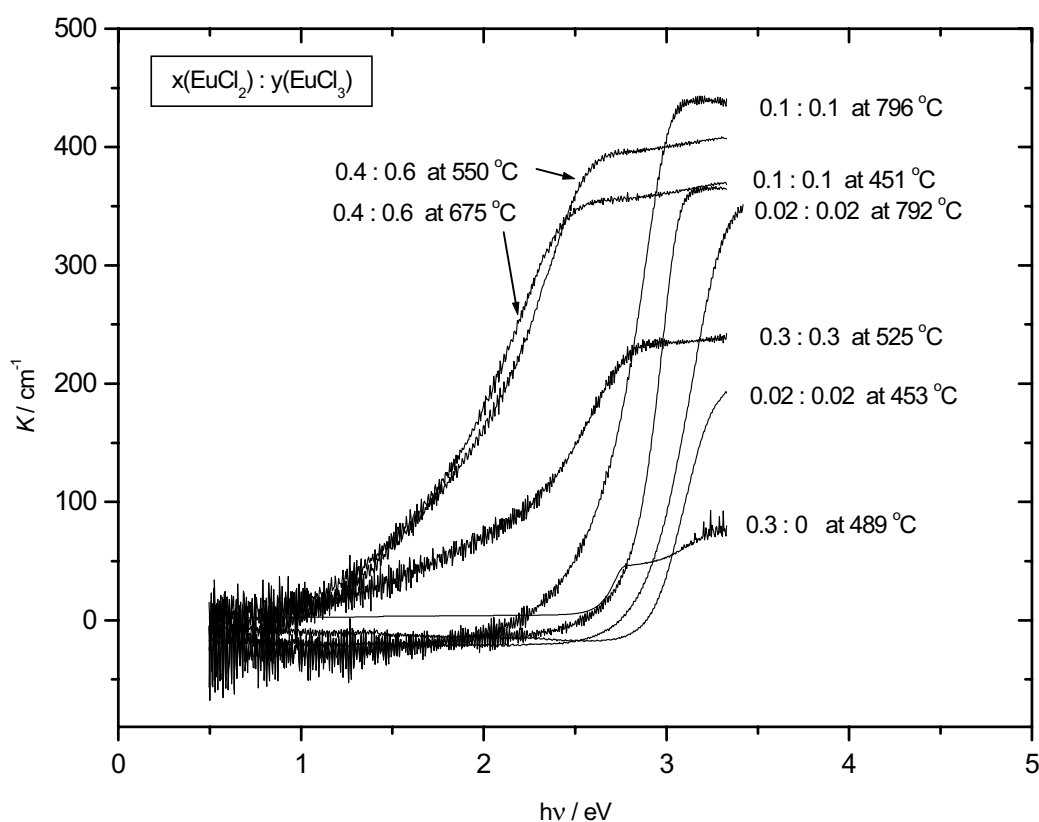


Fig. 5.6 Absorption spectra of $(\text{EuCl}_2)_x(\text{EuCl}_3)_y(\text{LiCl-KCl})_{\text{eut}, 1-x-y}$ melt. Since the background absorption constant could not be corrected (See sec. 4.3), some absorption constants have apparently negative values.

It is of interest to compare the optical properties of europium chloride melts with those of the corresponding solids which have been investigated extensively, see e.g. [Lange92]. The absorption spectra of crystalline mixed valent EuCl_x show a broad IVCT band at ~ 2 eV [Lange92]. As shown in Fig. 5.7 a very broad band appears after quenching the melts centered around 1.5 eV with more than 1 eV width, i.e. in the polycrystalline state. Moreover, it seems that the peak position shows a red shift with increasing temperature, which is a characteristic feature of the IVCT excitation. Details of IVCT band will be described in the discussion section.

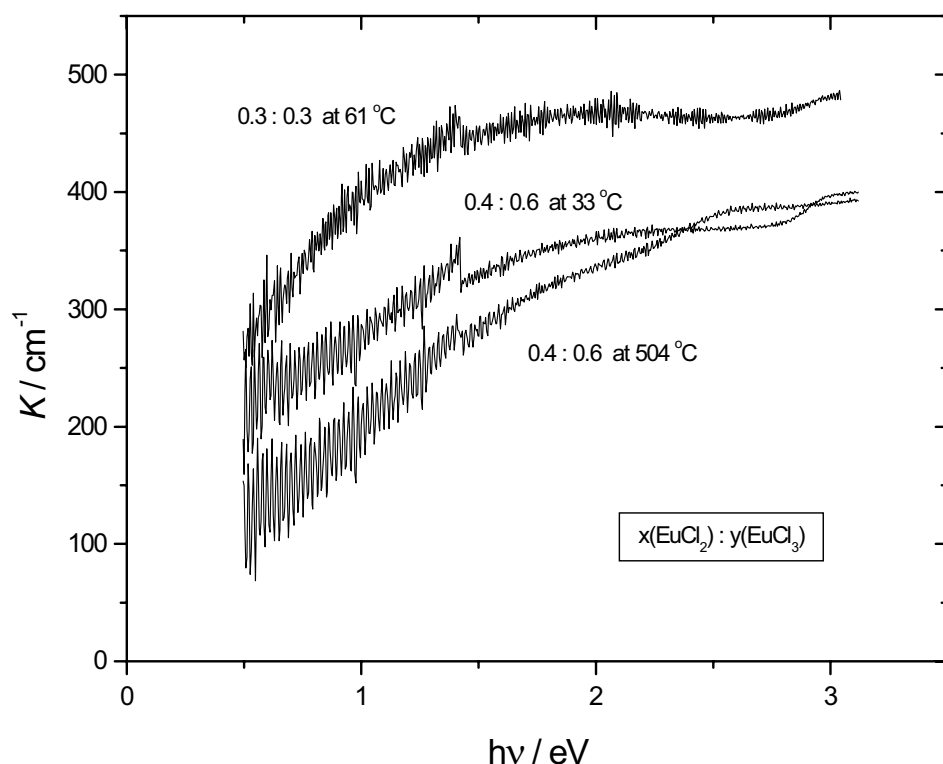


Fig. 5.7 Absorption spectra of $(\text{EuCl}_2)_x(\text{EuCl}_3)_y-(\text{LiCl-KCl})_{\text{eut},1-x-y}$ in the quenched polycrystalline state. The small jump at 1.4 eV is presumably due to switching of the detector at 870 nm.

5.3 Absorption measurements of $(\text{LnI}_2)_x(\text{LnI}_3)_y-(\text{LiI-KI})_{\text{eut},1-x-y}$ melts

As described in sec. 4.2.2, absorption measurements of rare earth halides in alkali halide eutectic melts may be disturbed by the formation of halide gas. This was especially the case for the rare earth iodide systems. In some preparations of $(\text{LnI}_2)_x(\text{LnI}_3)_y-(\text{LiI-KI})_{\text{eut},1-x-y}$ samples iodine gas was visible after the melting of the mixtures, which was confirmed by

means of spectrophotometry. Moreover, in all the absorption measurements of these melts the sapphire cells were not filled completely with sample melts, so that the obtained data in the higher energy range, where the fundamental absorption or halogen-metal charge transfer excitation dominates, cannot be considered here quantitatively above a certain value of the absorbance.

Fig. 5.8 shows the absorption spectra of a $(\text{NdI}_2)_{0.02}(\text{NdI}_3)_{0.02}-(\text{LiI-KI})_{\text{eut}, 0.96}$ melt at different temperatures. The spectra are characterised by a hypersensitive f-f transition at 2.1 eV, a strong absorption in the UV range, and by a weak absorption around 2.7 eV whose intensity decreases with increasing temperature. The latter band is especially interesting in relation with the experimental results of the corresponding neodymium chloride melts where the most intense absorption around 2.5 eV occurred at the composition of $x(\text{Nd}^{2+}) : y(\text{Nd}^{3+}) = 1 : 1$.

Fig. 5.9 shows the absorption spectra of a $(\text{CeI}_2)_{0.02}(\text{CeI}_3)_{0.02}-(\text{LiI-KI})_{\text{eut}, 0.96}$ melt. A very low and broad absorption around 2 eV is presumably caused by the interference effect of precipitated materials on the windows of the vacuum chamber due to the leakage of the cell.

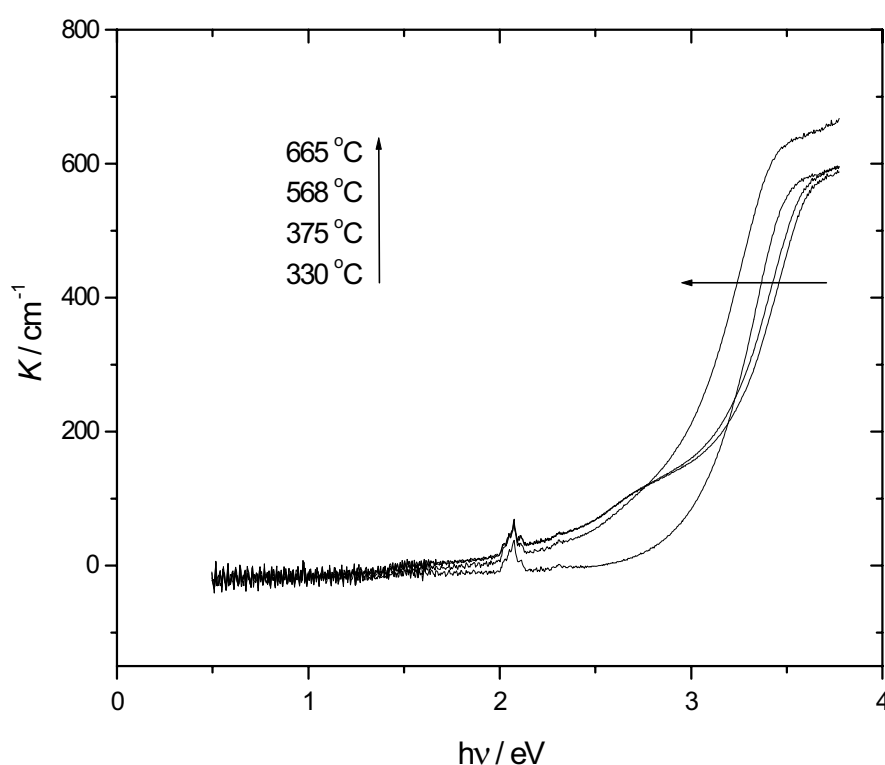


Fig. 5.8 Absorption spectra of a $(\text{NdI}_2)_{0.02}(\text{NdI}_3)_{0.02}-(\text{LiI-KI})_{\text{eut}, 0.96}$ melt. Temperature increases with the direction of the arrow displayed in the figure.

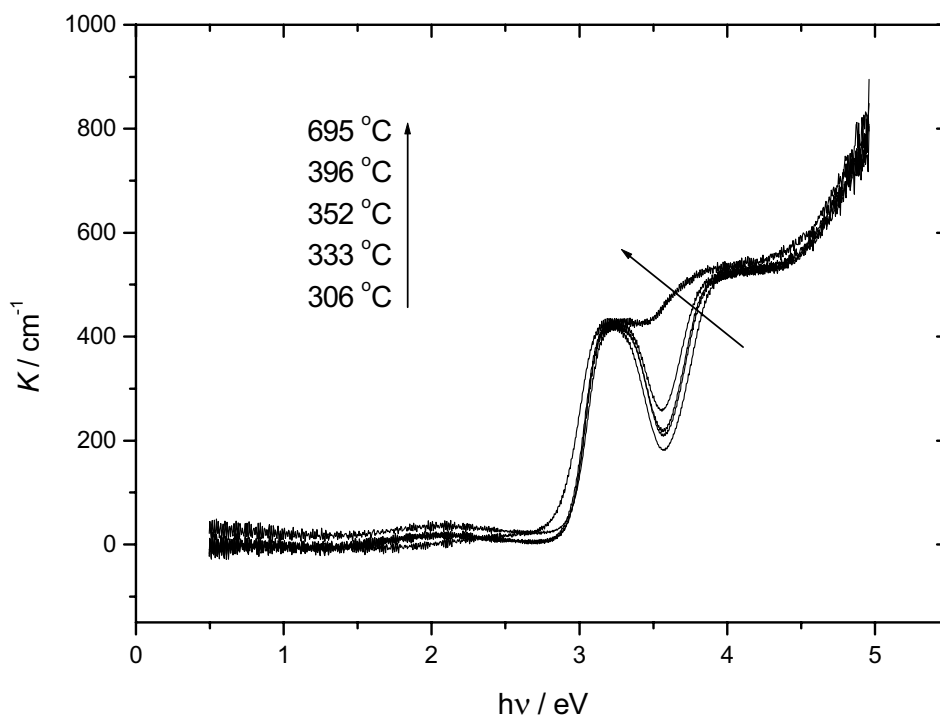


Fig. 5.9 Absorption spectra of $(\text{CeI}_2)_{0.02}(\text{CeI}_3)_{0.02}-(\text{LiI-KI})_{\text{eut}0.96}$ melt.

Further experiments have been performed both for neodymium and cerium iodide systems especially with higher rare earth halide concentration. However, as described before, the formation of iodine gas was remarkable and sufficient data could not be obtained. As a consequence, the observed excitation around 3.2 eV might be due to the polyiodide, e.g. I_3^- , in the melts. Child and Papatheodorou reported the optical excitation of an $\text{I}_2 - (\text{LiI-KI})_{\text{eut}}$ melt around 3.5 eV at 350 °C [Child83]. Though the slightly lower peak position in the present system might be related with the optical properties of Ce ions, the details are not clear yet.

5.4 Absorption measurements of $(\text{LnI}_2)_x(\text{LnI}_3)_{1-x}$ melts

In this study optical absorption spectra of $(\text{LnI}_2)_x(\text{LnI}_3)_{1-x}$ melt (Ln = Ce or Nd) have been measured with sapphire window for the first time without significant corrosion or gas formation which occurred crucially in the above described optical measurements.

5.4.1 (NdI₂)_x(NdI₃)_{1-x} melts

Pure NdI₃ melt

Fig. 5.10 shows the absorption spectra of a NdI₃ melt at different temperatures. The spectra consist of a hypersensitive f-f transition of the Nd³⁺ ion, i.e. $^4I_{9/2} \rightarrow ^4G_{5/2}$ (See section 5.2.1), and a fundamental absorption edge in the UV. Other intra 4f transitions are masked by the interference pattern typical of the thin liquid film optical cell. With increasing temperature, the absorption edge shifts towards lower energies.

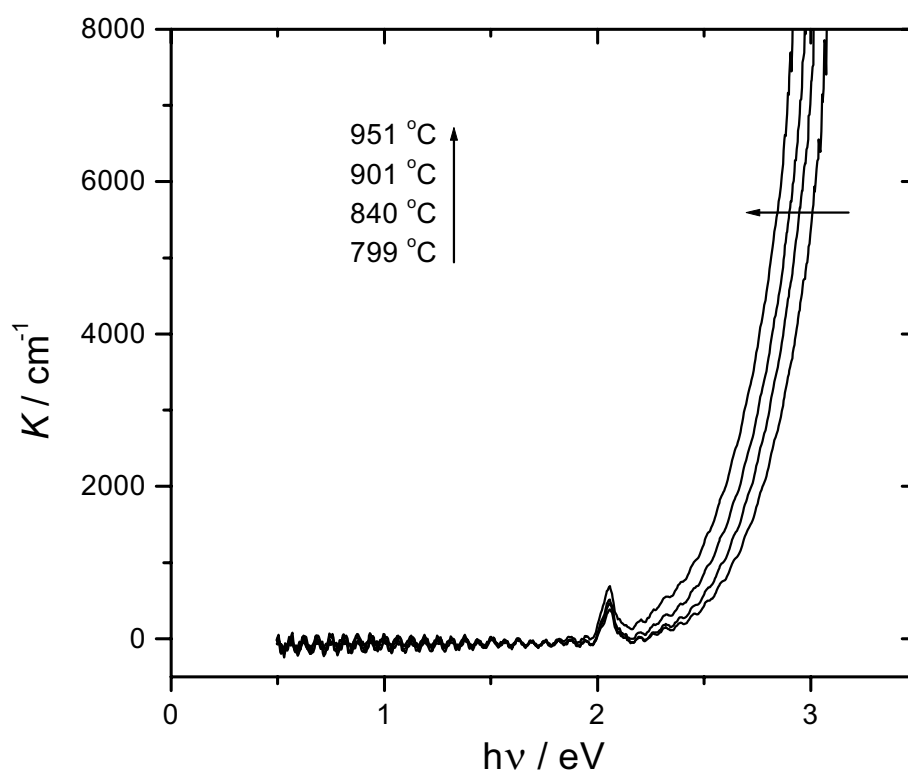


Fig. 5.10 Absorption spectra of NdI₃ melt. Temperature increases with the direction of the arrow displayed in the figure.

NdI₂ - NdI₃ mixture

The addition of NdI₂ into NdI₃ melt gave rise to the appearance of a broad band near 1.5 eV above 750 °C, as shown in Fig. 5.11 for a (NdI₂)_{0.78}(NdI₃)_{0.22} melt. The appearance and disappearance of this band was reversible in several heating and cooling cycles, so that this is

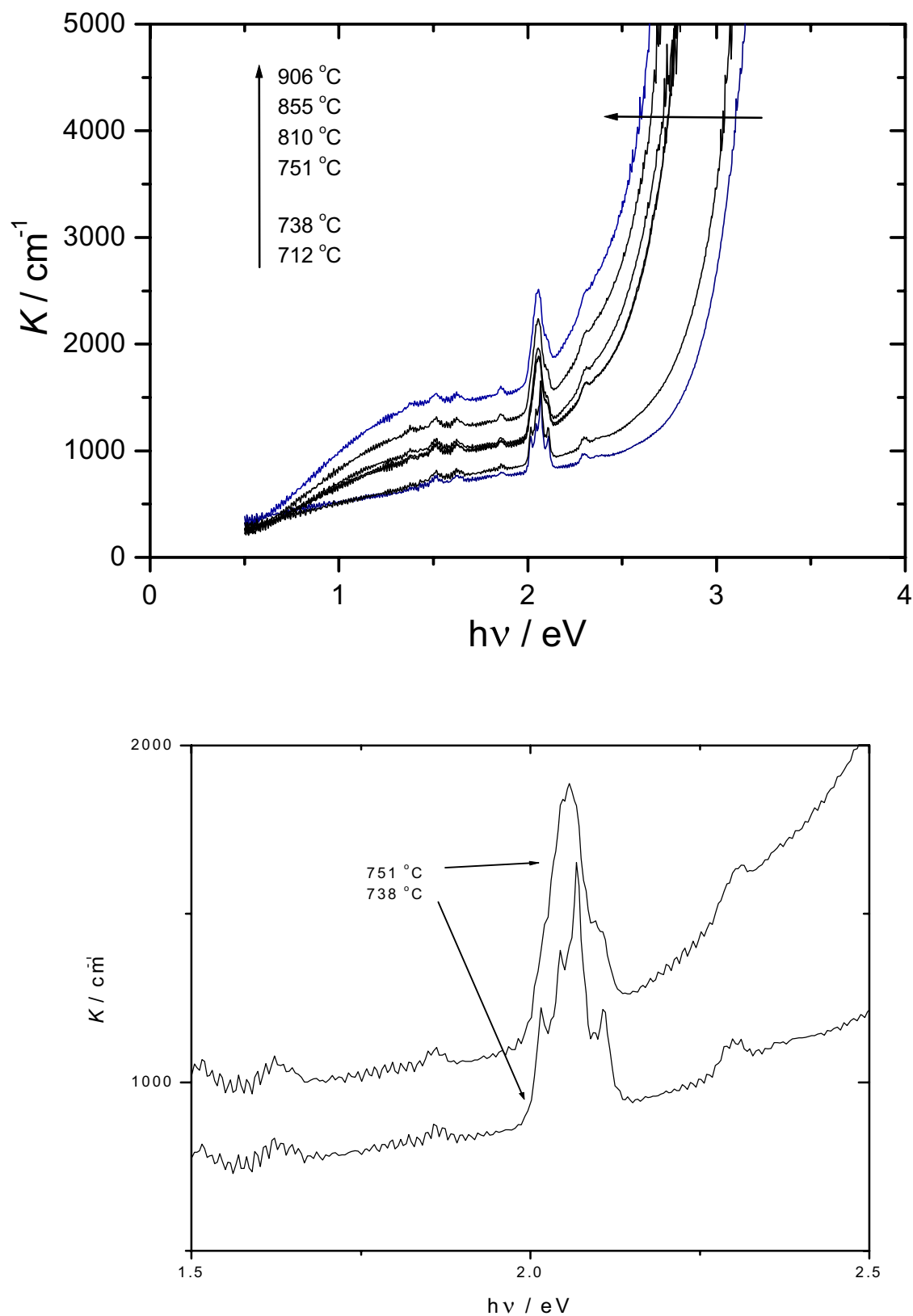


Fig. 5.11 Temperature variation of absorption spectra of a $(\text{NdI}_2)_{0.78}(\text{NdI}_3)_{0.22}$ melt.

not due to the effect of corrosion or other factors but is an intrinsic optical property of the melt. Furthermore, an interesting observation is that at a temperature of ~ 740 °C the spectral shape exhibits characteristic changes:

- 1) The hypersensitive f-f transition near 2.1 eV changes clearly as seen in the lower panel of Fig. 5.11. The spectra are very similar to those of solid and liquid NdI_3 [Gruen66], though the melting point of the mixture is around 500 °C [Bredig64], far away from the temperature observed here, i.e. 738 to 750 °C.
- 2) The fundamental absorption edge jumps by ~ 0.5 eV towards lower energies², indicative of a solid – liquid phase transition.

This peculiar phase transition will be further discussed in section 6.3.3.5.

Pure NdI_2 melt

Spectra very similar to the di- and trivalent mixtures were found for a pure NdI_2 melt (Fig. 5.12). In Fig. 5.13 spectra are compared with different NdI_2 concentration around 820 °C. The above mentioned transition of spectral shape was observed for the NdI_2 melt around 700 °C, at a slightly lower temperature than that for the $(\text{NdI}_2)_{0.78}(\text{NdI}_3)_{0.22}$ melt (Fig. 5.11).

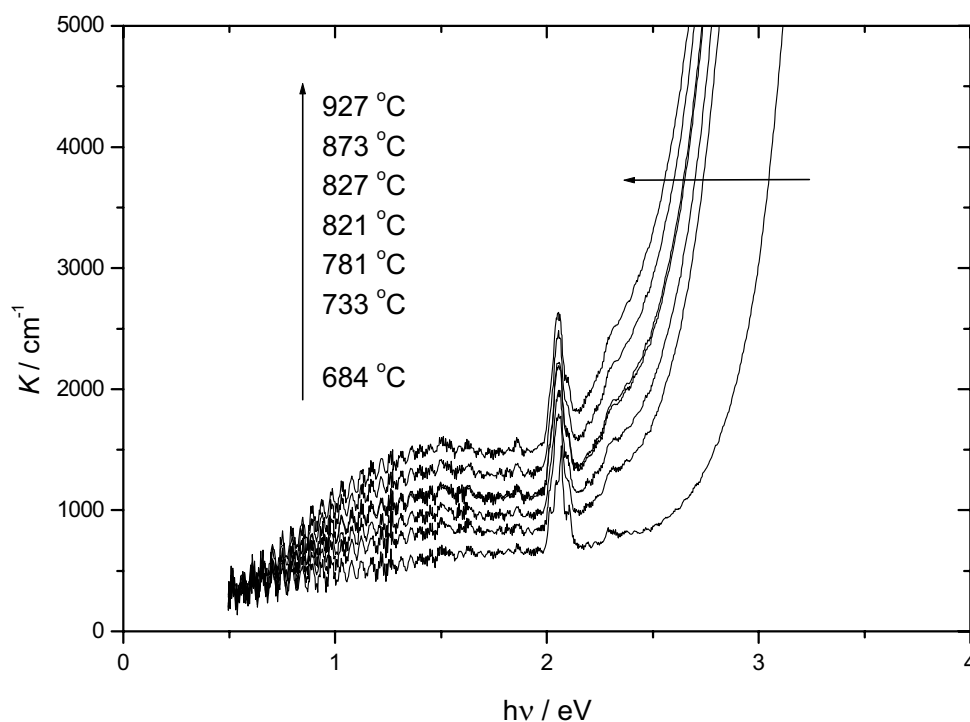


Fig. 5.12 Absorption spectra of a NdI_2 melt at different temperatures.

² The quantitative analysis is given in the next chapter.

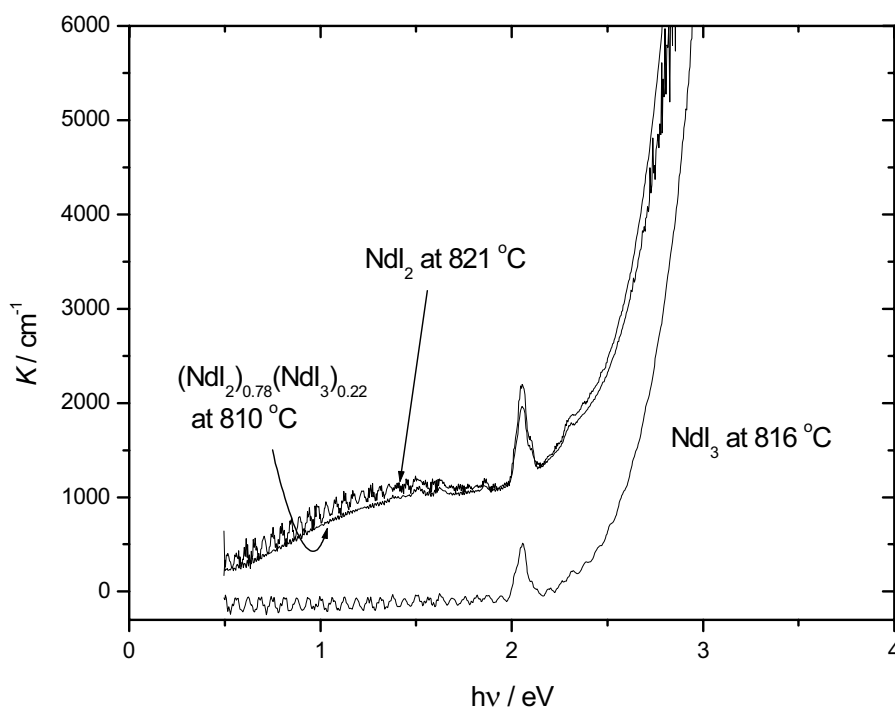


Fig. 5.13 Absorption spectra of $(\text{NdI}_2)_x(\text{NdI}_3)_{1-x}$ melt around 820°C .

Absorption measurements have been performed for several compositions of NdI_2 in NdI_3 , especially with emphasis on the composition of $[\text{NdI}_2]:[\text{NdI}_3] = 1:1$. However, here difficulties occurred in obtaining a homogeneous liquid film for the 1:1 composition. Presumably this is due to partial wetting of the sapphire windows by the melt and by decomposition of the neodymium iodide.

5.4.2 $(\text{CeI}_2)_x(\text{CeI}_3)_{1-x}$ melts

Fig. 5.14 shows the absorption spectra of a pure CeI_3 melt. No significant excitations (e.g. f-f transitions) have been found, which is in agreement with the literature data for Ce^{3+} ion in different solutions, see e.g. [Smith64]. The fundamental absorption edge towards the UV range shows a red shift with increasing temperature. From the conductivity behaviour of Ce doped CeI_3 melts it is expected (see Introduction) that the optical spectra of $\text{CeI}_2 - \text{CeI}_3$ mixtures show characteristics similar to the alkali – alkali halide melt [Freyland84, Nattland93], i.e. F-center absorption and Drude type absorption of nearly free electron.

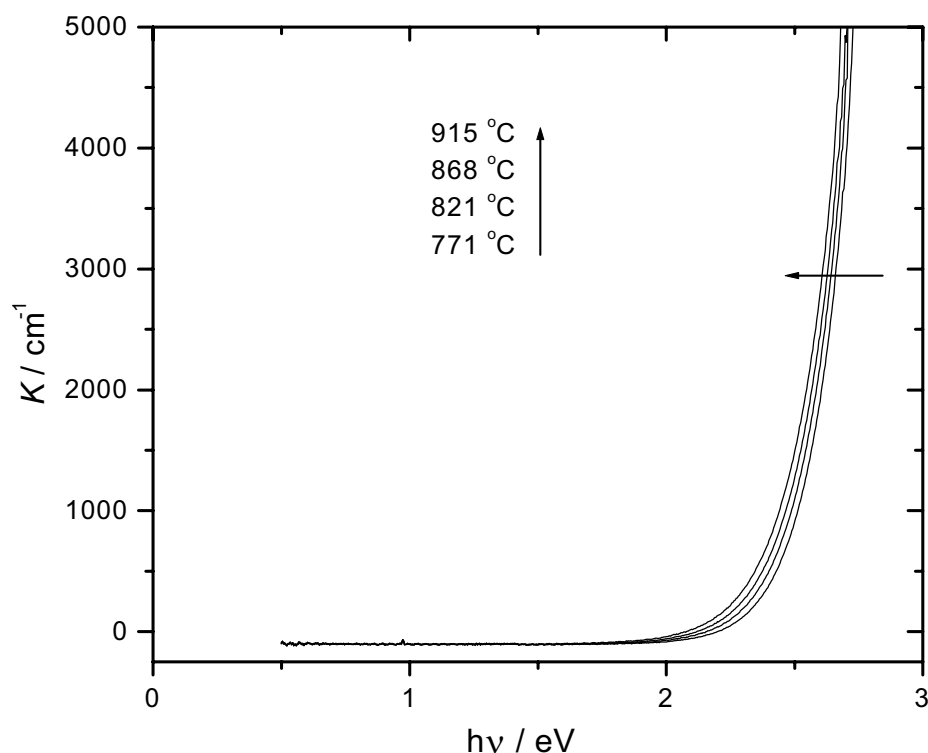


Fig. 5.14 Absorption spectra of a CeI_3 melt. Temperature of the sample follows the direction of the arrow in the figure.

Optical studies of the CeI_2 doped melts, however, show no significant change in comparison to the pure CeI_3 melt, as is shown in Fig. 5.15. As will be analysed and discussed in detail in the next chapter, the spectra of CeI_3 and $(\text{CeI}_2)_{0.06}(\text{CeI}_3)_{0.94}$ melts are identical with respect to the fundamental absorption. For the highest concentration of diiodide, the optical cell was not filled completely with the sample melt, and in addition, the volume of the bubbles increased with time, as shown in Fig. 5.15. It is concluded that the formation of I_2 -bubbles plays an important role.

On the other hand, it is unlikely that all the diiodide was converted to triiodide or reacted with sapphire within the time of experiment because of the following reasons. 1) If the corrosion or chemical reaction is dominant, it is expected that the background shows a profound increase (see e.g. Fig. 4.11). In the present system it is almost constant regardless of the doping of di-iodide. 2) In Fig. 5.16 are displayed the Raman spectra of solid CeI_3 and $(\text{CeI}_2)_{0.06}(\text{CeI}_3)_{0.94}$ samples whose optical spectra have been measured in the melt [Rodríguez B. 01]. It is seen that the structure of these two systems is clearly different in the solid at room temperature. Further consideration will be given in the discussion section.

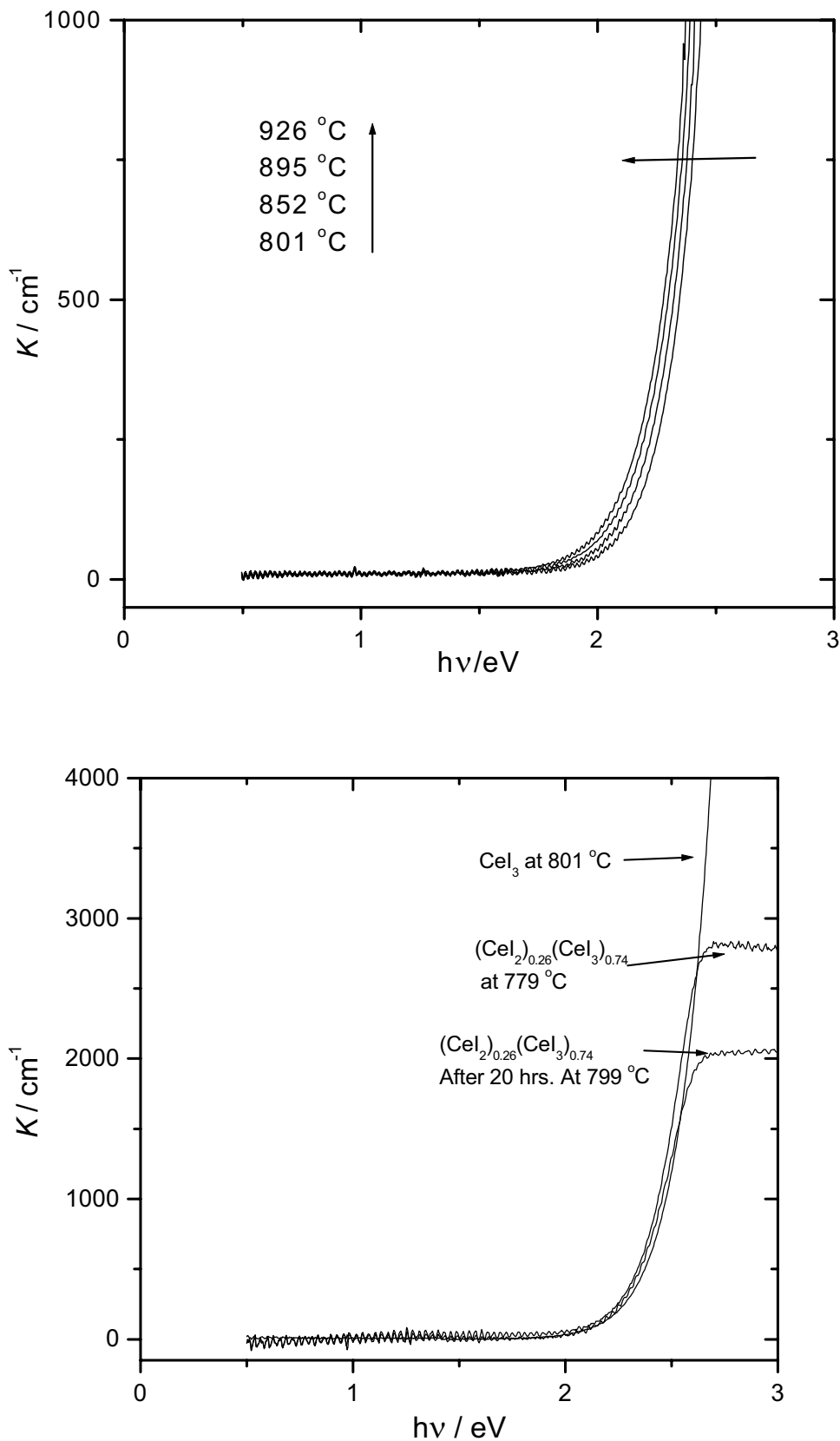


Fig. 5.15 Absorption spectra of di-iodide doped CeI_3 melt. Upper panel: $(\text{CeI}_2)_{0.06}(\text{CeI}_3)_{0.94}$ melt. Lower panel: $(\text{CeI}_2)_{0.24}(\text{CeI}_3)_{0.76}$ melt at different spectrum recording times, together with the spectrum of CeI_3 melt for comparison.

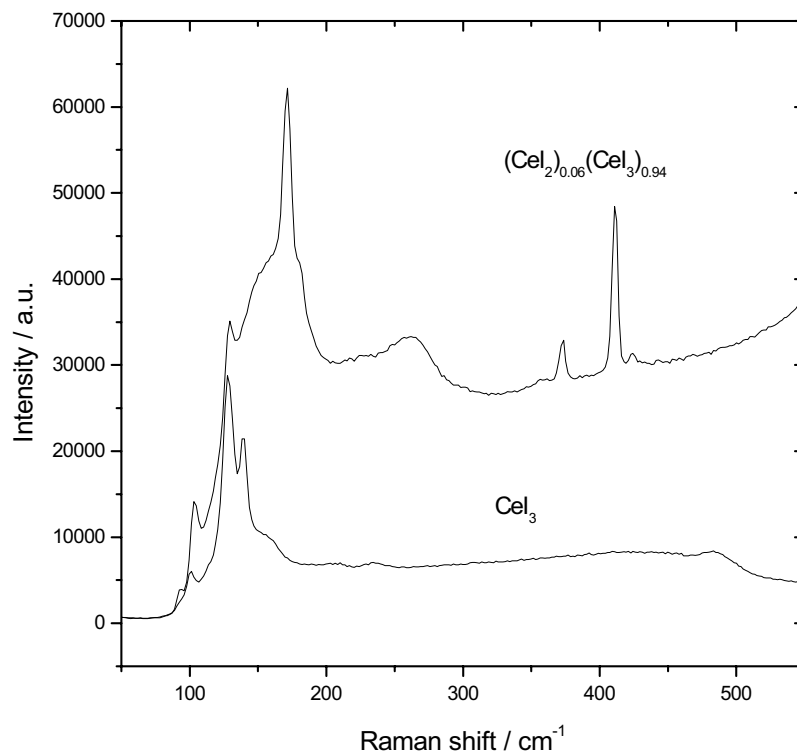


Fig. 5.16 Raman spectra of both solid CeI_3 and $(\text{CeI}_2)_{0.06}(\text{CeI}_3)_{0.94}$ samples in the sapphire cells which had been used for the optical measurements [Rodriugez B. 01]. Spectra were taken at room temperature with He-Ne laser (633 nm). Details of experimental techniques is given in [Rodriugez B. 02].

5.5 ESR measurement of a $(\text{NdCl}_2)_{0.02}(\text{NdCl}_3)_{0.02}-(\text{LiCl-KCl})_{\text{eut}, 0.96}$ melt

As described in chapter 4, difficulties occurred in obtaining the ESR spectra with sufficient reproducibility. Therefore, the following presentation of ESR results has to restrict on the example of the of $(\text{NdCl}_2)_{0.02}(\text{NdCl}_3)_{0.02}-(\text{LiCl-KCl})_{\text{eut}, 0.96}$ liquid system.

Fig. 5.17 shows the typical ESR spectra of this system at different temperatures up to 415 °C. The spectra are characterised by two sapphire signals due to transition metal impurities³ at ~ 1890 and 5300 Gauss, and by a large half width of the ESR resonance with a peak-to-peak

³ Two signals are presumably due to the g-values of single crystal of sapphire parallel and vertical to magnetic field applied, i.e. g_{\parallel} and g_{\perp} .

value, ΔB_{pp} , of 1100 Gauss at 350 °C. Such a broad ESR resonance is typical of Ln-ions – see discussion section. The interesting ESR parameters are summarized in Table 5.1.

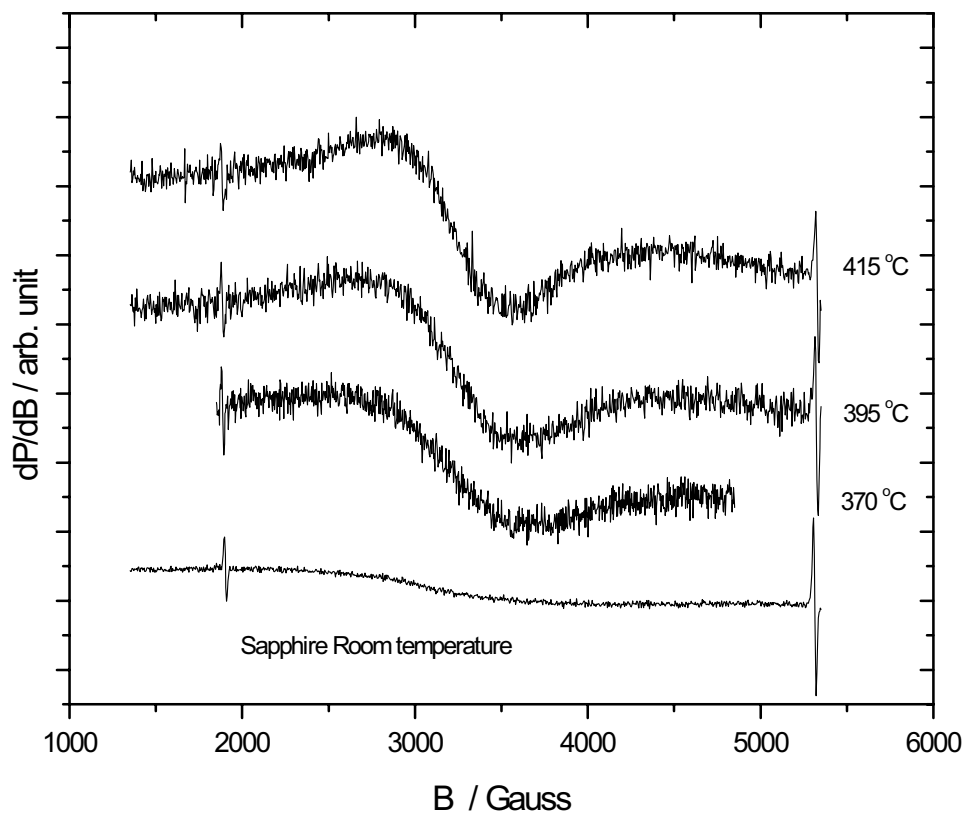


Fig. 5.17 ESR spectra of $(\text{NdCl}_2)_{0.02}(\text{NdCl}_3)_{0.02}-(\text{LiCl-KCl})_{\text{eut}, 0.96}$ melt at different temperatures. Intensity of sapphire spectrum was scaled to fit the intensity of the sapphire signal around 5300 Gauss to that in the melt at 395 °C.

Table 5.1 ESR parameters for the broad band around 3300 Gauss for $(\text{NdCl}_2)_{0.02}(\text{NdCl}_3)_{0.02}-(\text{LiCl-KCl})_{\text{eut}, 0.96}$ melt

T / °C	g-factor	Integrated Intensity / a.u.	ΔB_{pp} / Gauss
350	2.11	1.62	1100
395	2.10	1.75	930
415	2.08	1.33	780

Two resonances of the sapphire capillary of the cell, which have been recorded *in situ*, serve as an internal standard for calibration of the spin intensity [Schindelbeck95, Poh01]. Spectrum of sapphire compartment is also displayed in the figure where its intensity was multiplied by 0.22 in order to fit that in the spectrum of the melt at 395 °C.

6. Discussion

In the previous chapter the results of both optical and ESR measurements of Ln-LnX_3 and $\text{LnX}_2\text{-LnX}_3\text{-(LiX-KX)}_{\text{eut}}$ melts have been presented. In the discussion of these results the main focus is to clarify the different electronic properties within the rare earth metal series. As mentioned in chapter 1, the electrical conductivity of the lighter rare earth metal systems, i.e. La or Ce, shows a strong increase with metal composition, which is analogous to the alkali-alkali halide (M-MX) melts (type1). On the other hand, that of heavier metals, e.g. the Nd system, shows only a slight deviation from the additivity of the ionic conductivities of Nd^{2+} and Nd^{3+} molten salts at the composition of $[\text{Nd}^{2+}] : [\text{Nd}^{3+}] = 1:1$ (type2). Thus, for the following discussion it is convenient to treat them separately, namely pure halide melts and lighter and heavier rare earth metal – metal halide melts, and to compare the results with existing literature data of both type 1 and 2 melts, e.g. M-MX, In-InX₃, refractory metal halide melts, and solid mixed valence compounds. For this purpose the following important aspects are focused on and discussed in this chapter: 1. The influence of disorder and thermal fluctuation on the electronic structure, 2. The role of electron localization in the melts, 3. Electron dynamics.

For fluid systems at high temperature the local fluctuation of potential on a time scale of the order of pico second, i.e. a typical diffusional time scale, becomes important, and influences the character of the band structure of the system. As discussed in several theoretical models [Logan92, Koslowski96] this influence plays especially a crucial role for ionic fluids. In the next section this point and its consequences for the optical properties of pure halide melts will be discussed. The charge transfer band, namely the electronic excitation from halogen anion to metal cation, will be analysed, which has been studied intensively both theoretically and experimentally.

Recent intensive studies on the M-MX systems give us the details of their electronic structure, especially of localised electronic defect species in metal doped melts. This information makes it possible to discuss the electronic structure in comparison with the lighter rare earth-rare earth halide melts. After a brief description of the experimental and theoretical results of M-MX melts the results for the lighter rare earth systems will be discussed.

As for the heavier metal systems (type2), e.g. Nd or Eu, the electron hopping between cation sites with different oxidation states are expected, which is the important electron transfer mechanism in class II compounds of mixed valence compounds (see chapter 2). A theoretical model for the electron transfer process is introduced and applied for the quantitative interpretation of the present results. It follows a discussion on electron dynamics in these systems.

6.1 Microscopic structure of LnX_3 , LnX_2 and $\text{LnX}_3\text{-MX}$ solids and melts

The physicochemical properties of molten LnX_3 and $\text{LnX}_3\text{-MX}$ salts have been quite intensively studied both experimentally and theoretically in recent years. Especially, their structural data are currently available owing to the recent experimental progress and systematic studies by Raman [Photiadis97], X-ray [Iwadata95] and neutron diffraction methods [Wasse99], including their theoretical interpretations, e.g. [Hutchinson99, Madden00]. These features are briefly discussed in this section.

Some of the physicochemical properties of MX_3 crystals and melts are listed in Table 6.1 and 6.2, together with those of alkali halides.

Table 6.1 Structural data for some crystalline rare earth trihalides [Haschke79]

Structure type (space group)	UCl_3 ($\text{P}\bar{3}\text{cl}$)	PuBr_3 (Cmcm)	YCl_3 (C2/m)	BiI_3 ($\text{R}\bar{3}$)
Cl	La-Gd	Tb	Dy-Lu, Y	
Br	La-Pr	Nd-Eu		Gd-Lu, Y
I		La-Nd		Sm-Lu, Y
X^-/R^{3+} Range	1.63-1.93	1.96-2.17	1.99-2.13	2.08-2.55
Cation CN	9	8	6	6

Table 6.2 Change of some physicochemical properties of rare earth trichlorides and alkali halides on melting [Freyland95, Iwadata98, Wasse99 and references therein].

T_m : temperature of melting, $\Delta V/V$: the percentage volume change relative to the solid volume, σ : the ionic conductivity near the melting point, R_{+-} : the nearest neighbour cation-anion distances in the melt and corresponding crystalline data in brackets, E_0 : the fundamental optical absorption energies of the melt, together with energy gap of the corresponding crystals, E_g , in brackets.

Salt	T_m ($^{\circ}\text{C}$)	$\Delta V/V$ (%)	σ ($\Omega^{-1} \text{cm}^{-1}$)	R_{+-} (\AA)	$E_0(E_g)$ (eV)
(Crystal structure UCl_3 type)					
LaCl_3	858-877	16-19.1	1.2-1.5	2.93	
LaBr_3	788	12	0.6-0.8	3.01	
CeCl_3	817	18	0.8-1.1	2.93	
CeBr_3	732			3.01	
NdCl_3	768	21.8	0.8		
SmCl_3	662	24.5	0.5		
GdCl_3	602	26.5	0.2		
(Crystal structure PuBr_3 type)					
LaI_3	778	24	0.4	3.18	(3.8 ^b)
CeI_3	760		0.4	3.18	(3.5 ^b)
NdBr_3	682 ^a		0.5 ^a		
NdI_3	782 ^c		0.4 ^a		
(Crystal structure YCl_3 type)					
YCl_3	714	0.5	0.35-0.40	2.64	
ErCl_3	775	5.3	0.3-0.4	2.66	
(MX)					
NaCl	807	25.6	3.59	2.78(2.81)	6.3
NaI	662	18.6	2.24	(3.23)	4.6
KCl	772	20.2	2.16	3.06(3.14)	6.2 (8.9)

^a [Dworkin63], ^b [Stöwe97], ^c [Bredig64]

On melting a large fractional volume change is observed for LnX_3 systems, which are of special interest here (Ce, Nd, Eu)¹, its increase being comparable to the MX melts. The coordination number (CN) around a rare earth cation decreases from 9 or 8 for the crystalline to ~ 6 in the liquid state. Raman [Photiadis98] and X-ray diffraction studies [Iwadate95] show that the dominant structure of the melts is the distorted octahedral complex, LnX_6^{3-} (X=Cl, Br), sharing edges with neighbouring octahedra.² Addition of MX leads to a continuous destruction of the loose network structure. Consequently, the predominant species are LnX_6^{3-} octahedra in molten mixtures rich in alkali halide with mole fractions of LnX_3 less than 0.25 [Photiadis98].

The ionic conductivity of LnCl_3 melts is of the order of $1 \Omega^{-1} \text{ cm}^{-1}$, indicating fully ionised liquids, and the value decreases with increasing atomic number of cation and anion. From these considerations of the similarity to alkali halides upon melting the electronic structure of LnX_3 melts can be considered by purely ionic models [Tatlipinar92] and they are treated within the ionic model in the following sections. It should be noted, however, that the influence of “covalent” effects, which may be crucial for iodides, have to be treated through polarizability models [Madden00].

In comparison to LnX_3 melts, less is known for pure divalent halide melts except the conductivity measurements performed by Bredig’s group [Bredig64]. This is due to the extreme chemical corrosive properties and the problems of disproportionation, i.e. $3\text{LnX}_2 \rightarrow 2\text{LnX}_3 + \text{Ln}$, in some cases. The experimental data found in the literature are density and Raman measurements of the stable divalent EuCl_2 melt [Gaune-Escard99, Koyama97]. Raman spectra give less information on the structure but it is assumed that the structure is similar to the crystalline compounds. In Table 6.3 are summarised the crystal structure data of rare earth dihalides.

¹ For monoclinic LnX_3 (e.g. YCl_3) the volume does not change drastically upon melting. This indicates that the structure of these LnX_3 melts is similar to the monoclinic solid with coordination number of ~ 6 . Accordingly, the local structure of all LnX_3 melts is similar to each other, independent of their structure of crystals [Papatheodorou00].

² On the other hand, CN of $\sim 7-8$ was reported and no evidence for LnX_6^{3-} species was found by neutron diffraction [Wasse98, 99] and MD studies [Hutchinson99].

Table 6.3 Structural data for some crystalline rare earth dihalides [Haschke79]

Structure type (space group)	PbCl ₂ (Pnma)	CuTi ₂ (I4/mmm)	SrBr ₂ (P4/n)
Cl	Nd, Sm, Eu		Dy
Br	Nd, Sm		Sm, Eu
I		La-Pr	Nd
Cation coord. No.	9	8	8

6.2 Optical absorption in pure rare earth metal trihalides

6.2.1 Electronic structure of ionic liquids and Charge transfer band

In a simple picture of the electronic structure of typical ionic compounds, for instance NaCl, the valence band arises from states of halogen (3p for Cl) and conduction band from orbitals of metal (3s for Na) - see e.g. [Cox87]. As mentioned above, the influence of potential fluctuations on the nature of band edge states is especially important for ionic liquids. Logan and Siringo studied the distribution of Madelung energies of the liquid state within the framework of linear theories such as the mean spherical approximation [Logan92]. They found a Gaussian distribution of the Madelung potential fluctuations with a half width of the order of an electron volt. The mean Madelung potential energy itself changes only slightly upon melting. As a consequence, together with the consideration on the influence of the purely topological disorder effect [Koslowski96], both valence and conduction bands broaden upon melting, and the crystal gap is smeared out by a Gaussian tailing of the band edge states. John *et al.* investigated the behaviour of this band tailing by considering a Gaussian random potential [John88]. An exponential tail in the density of state is found for the systems with rapidly decaying short range potential-potential correlation.

These theoretical considerations are consistent with the empirical Urbach rule which describes the frequency and temperature dependence of the excitation of the low-frequency UV or fundamental absorption and is given by:

$$K_{\text{Urbach}}(\hbar\omega) = K_0 \exp\left(\frac{\gamma}{kT}(\hbar\omega - E_0)\right), \quad (6.1)$$

where K_0 is the absorption constant at the maximum of the optical excitation, E_0 is the energy gap and γ is a constant. This rule can be applied almost universally for alkali halide crystals and melts, and amorphous solids³ [Freyland95, Mott71]. Typical values of these parameters are: $K_0 \sim 10^5\text{-}10^6 \text{ cm}^{-1}$, $\gamma \sim 1$.

The optical absorption edge of LnX_3 melts is analysed in the following with the Urbach relation, eqn. (6.1). Fig. 6.1 shows the absorption spectra of CeI_3 on a logarithmic scale vs. energies, $\hbar\omega$ – see also Fig. 5.14. As is clearly seen, the spectral characteristics are totally in accordance with the Urbach relation: i.e. 1. the absorption edge follows an exponential dependence on $\hbar\omega$. 2. the apparent slope decreases with increasing temperature, 3. the spectra for different temperatures merge at a specific energy, E_0 . In the low and high absorption constant range, i.e. $\ln(K/\text{cm}^{-1})$ up to ~ 2 and above ~ 8.3 , the uncertainty of the measured K -values causes the scattering on logarithmic scale as is seen in the figure. In order to evaluate the spectra more quantitatively fitting with eqn. (6.1) was performed by means of a least square algorithm according to the Lavenberg-Marquardt method, see e.g. [Press89] and [Diehl95]. In these fitting procedures the initial parameter values should be physically reasonable in order to obtain meaningful results. Furthermore, for sufficient accuracy the number of the parameters should be as low as possible. These points are especially crucial when a complex fitting function is used, which will appear in the later sections. In the present case $\ln K = \alpha\hbar\omega + \beta$ has been taken as a model function. Thus, γ is determined through $\gamma = \alpha kT$ from the fitting results of the slope, α . E_0 is then obtained from the mean value of the cross points of the lines at different temperatures. Finally, K_0 is given by the above γ , β and E_0 . The obtained parameters for pure LnX_3 melts are summarised in Table 6.4. The values of γ and K_0 are reasonable for typical Urbach parameters, indicating that the absorption band is a charge transfer excitation. The general trend of the optical gap energy, E_0 , also holds for LnX_3 melts, namely E_0 decreases upon melting (though only slightly) [Freyland95] and with increasing anion size [Cox87].

³ Various theoretical models of the Urbach rule are briefly reviewed in [Mott71].

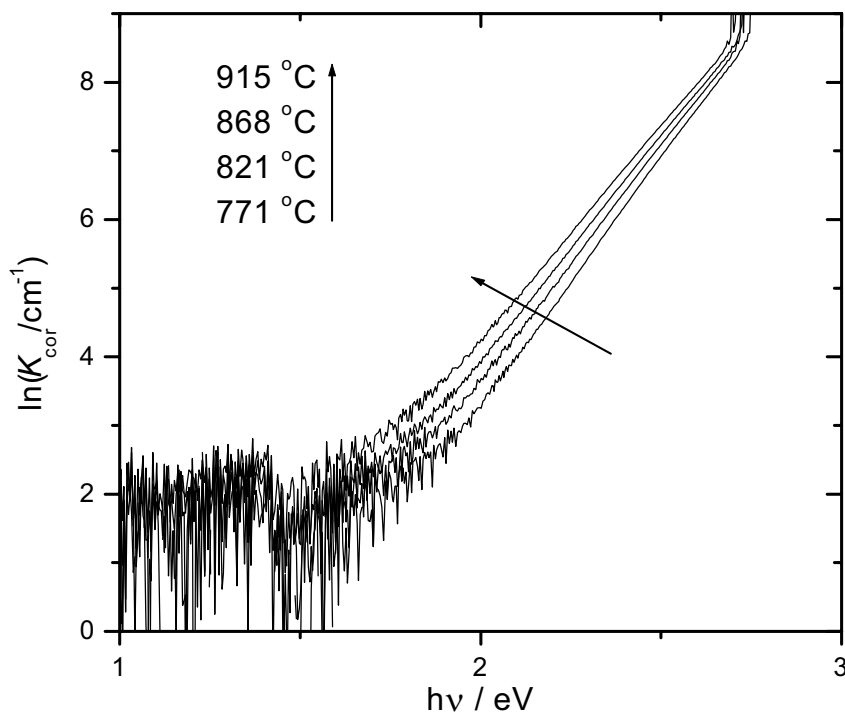


Fig. 6.1 Absorption spectra of CeI_3 melt on a logarithmic scale. For background correction the absorption constant is shifted by 100 cm^{-1} upward. Temperature of the melt increases with the direction of arrow in the figure. The uncertainty in absorbance causes the scattering in the low and high K regions of spectra.

Table 6.4 Summary of Urbach parameters of pure LnX_3 melts.

	CeI_3	NdCl_3^{a}	NdI_3
Temp. range / $^{\circ}\text{C}$:	771-915	769-887	799-951
γ :	0.65 ± 0.01	0.48	0.44 ± 0.01
$K_0 / 10^4 \text{ cm}^{-1}$:	9.5 ± 0.9	8.1 ± 0.3	6.0 ± 0.2
E_0 / eV :	2.9 ± 0.4	5.3 ± 0.1	4.0 ± 0.1

^a [Potapov98]

In the following the results are discussed in terms of a model proposed for interpretation of the optical gaps of alkali halides [Senatore84]. For crystalline alkali halides E_0 is qualitatively described by

$$E_0 = E_A - E_I + \alpha_M \frac{e^2}{4\pi\epsilon_0 R_{+-}}, \quad (6.2)$$

where E_A is the halogen electron affinity, E_I is the metal ionisation potential, α_M is the Madelung constant and R_{+-} is the lattice constant. This simple formula provides insights into the origin of the optical gap energy: an optical excitation is associated with the electron transfer from a halogen anion to metal cation, thus, the term $E_A - E_I$ contributes to E_0 . The Madelung potential for an electron is positive for the cation site (raises the energy level) and negative for the anion site (lowers the energy level) so that it enters eqn. (6.2) "twice". Roughly half of this is compensated by other effects, e.g. band broadening and polarization effects, leading to eqn. (6.2). This formula was further extended to the liquid phase taking into account the changes in the microscopic structure as follows [Senatore84]:

$$E_0 = E_A - E_I + (-E_M) \left(f_X + \frac{g_M}{\epsilon_\infty} \right) - \frac{2e^2}{R_{+-}\epsilon_\infty}, \quad (6.3)$$

where E_M is the Madelung energy of the liquid and the coefficients f_X and g_M are given by

$$f_X = 1 - \rho\sigma/(1+\rho) \quad \text{and} \quad g_M = 1 - \sigma/(1+\rho)$$

$$\text{with } \sigma = R_{+-} / s \quad \text{and} \quad \rho = \sigma_- / \sigma_+,$$

σ_+ and σ_- being the ionic radii of cation and anion in Å, respectively, and s a scaling divisor. The lattice constant R_{+-} is now modified and is the nearest-neighbour ionic distance in liquids. The scaling divisor s is assigned a value of 15 and 20 for crystals with NaCl (CN=6) and CsCl (CN=8) type structure, respectively, and for melts $s \sim 10$ gives a best fit to the experimental data of MX melts (with the apparent CN of ~ 6) [Senatore84].

In order to apply eqn. (6.3) to LnX_3 melts, the first two terms should be modified as $3E_A$ and $E_1 - E_2 - E_3$ where E_i is the i -th ionisation energy of the rare earth metal. Since the Madelung energy for a liquid is known to differ only slightly from that of the solid [Senatore80], the lattice energy of crystalline compounds has been used instead of $(-E_M)$ [CRC97]. For the dielectric constant of the high frequency limit, $\epsilon_\infty = (1.9)^2$ is taken where the refractive index of 1.9 was estimated from the literature data of LaCl_3 (~ 1.7 [Mochinaga78]) and LaBr_3 (~ 1.8 [Fukushima96]) melts. With the above assumptions the calculation yields an E_0 of the order of 10 eV with different s values ($s = 8-10$), a factor of 2-3 larger than the experimental values (see Table 6.4). It should be noted that similar deviation from eqn. (6.3) have been found for divalent alkaline earth halide melts, e.g. MgCl_2 and MgI_2 [Bachtler89].

6.2.2 Intra 4f transition

In the optical absorption spectra of neodymium halide melts a hypersensitive transition ($^4I_{9/2} \rightarrow ^4G_{3/2}$) has been observed at ~ 2.1 eV. As has been mentioned in section 2.3.3, hypersensitive transitions are sensitive to changes of the symmetry and interaction with the surrounding ligands. From the band integration the oscillator strength, f , has been determined for NdI_3 melts by eqn. (2.21) with the corresponding density data [Kutscher74]. For the refractive index which appears in eqn. (2.21) a value of $n = 1.9$ is taken (see above). The temperature dependence of f is plotted in Fig. 6.2. It can be seen that the oscillator strength shows an increase within the experimental errors from 30×10^{-6} at 800°C to 40×10^{-6} at 900°C . This observation indicates a change in the structure or symmetry of the complex ions. Chrissanthopoulos and Papatheodorou reported the increase of the oscillator strength of the Ho^{3+} hypersensitive transition with increasing temperature [Chrissanthopoulos00]. They concluded from their results, together with Raman data, an increase of octahedral distortion imposed on the HoCl_6^{3-} octahedral species with increasing temperature. The same argument holds presumably for NdI_3 melts. Further experiments, e.g. Raman measurements, are required for the determination of the structural changes.

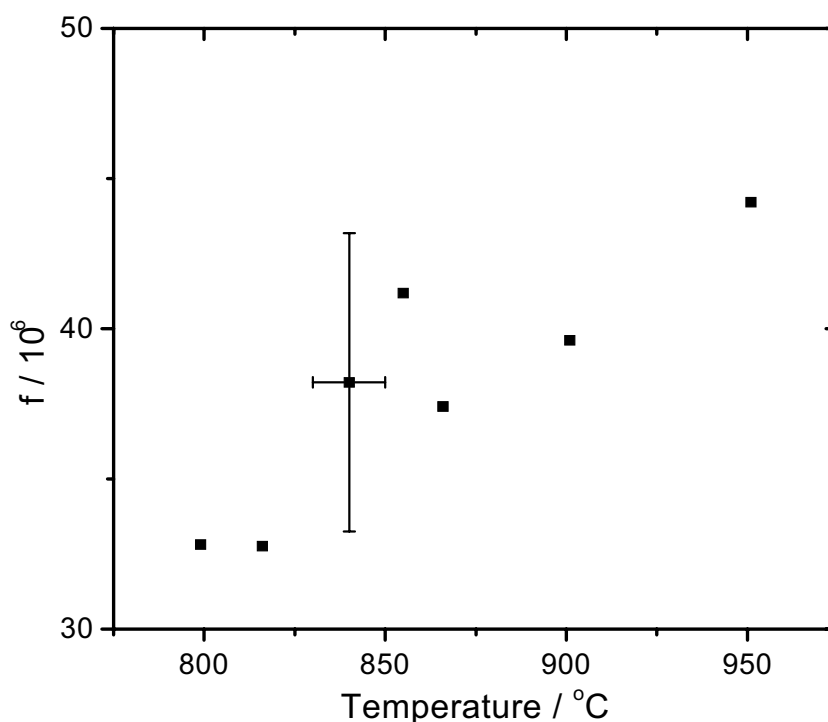


Fig. 6.2 Oscillator strength of the f-f transition around 2.1 eV for a NdI_3 melt.

As for the absolute value of the oscillator strength of NdI₃ melts, Gruen and Decock reported a value of 210×10^{-6} at 800 °C [Gruen66]. The reason for the difference of a factor ~ 7 in comparison to the measurements of this work is not yet clear. It should be noted, however, that the oscillator strengths of the hypersensitive transition of other Nd-complexes [Misra93] and that of Ho³⁺ in rare earth halide melts, as mentioned above, are in good agreement with the present result.

6.3 Electron localization and VIS-IR spectra in M-MX and Ln-LnX₃ melts

6.3.1 F-center and Mollwo Ivey rule

One of the main objectives of this work was to examine the metal-doping effect on the spectral parameters discussed above. In the following section the optical spectra of metal-doped melts are considered with respect to the literature data of the M-MX systems, and the results of Ce-CeI₃ melts are considered, whose optical spectra have been conjectured to be analogous to those of the M-MX systems.

The dominant electronic defect in coloured alkali halide crystals is the well-known F-center⁴. It is characterised by a strong absorption peak around 2 eV for KCl [Fowler68]. In the liquid state evidence for F-center like defect species has been found [Freyland95]. Optical spectra of M-MX melts show the absorption band around 1.3 eV for K-KCl melts at 800 °C. The electronic structure of the F-center in liquid state has been intensively studied by computer simulation studies for M_xMX_{1-x} melts [Selloni87, Koslowski97].

For crystalline alkali halides the absorption maximum, E_{max} , of the F-center follows the so-called Mollwo-Ivey relation which is given by [Fowler68]:

$$E_{max} \propto R_{+-}^{-\alpha}, \quad (6.4)$$

where α is a constant depending on the structure ($\alpha \sim 1.8$ for NaCl type, $\alpha \sim 2.5$ for CsCl type) and R_{+-} is the inter ionic distance (see Table 6.2). As shown in Fig. 6.3, the Mollwo-Ivey rule can also be applied for M-MX melts except the Na systems [Freyland95]. This observation implies - though a high degree of disorder is expected from the drastic density change of \sim

⁴ With increasing the defect concentration the aggregated species like M or V centers should be considered.

20 % upon melting - that the local structure is rather well defined by Coulombic ordering similar to the crystals, which is confirmed by the pair correlation functions [Ballone84].

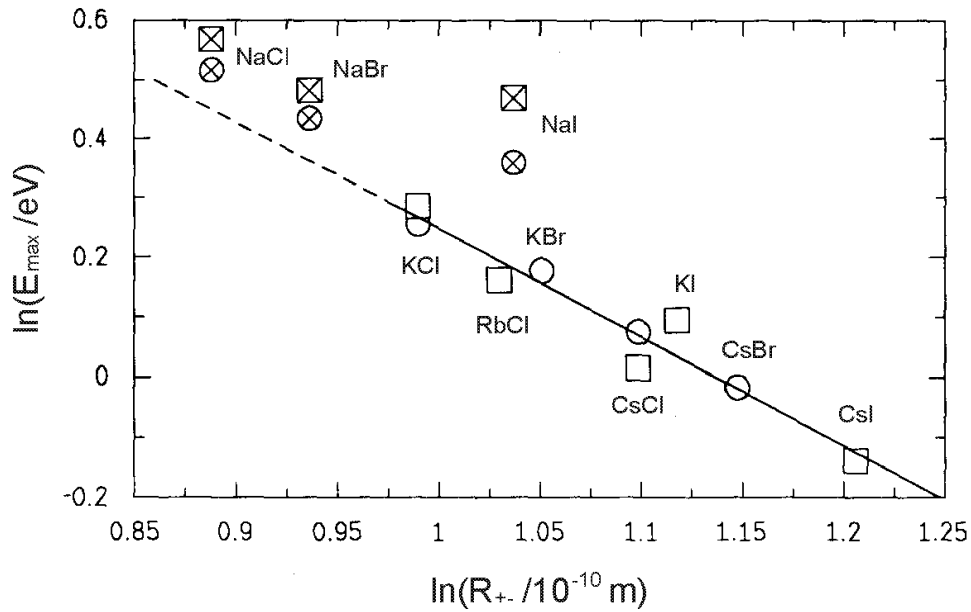


Fig. 6.3 Mollwe-Ivey plot for dilute M-MX solutions: Optical absorption maximum at temperatures near the melting point as a function of the interionic distances [Freyland95]. The circles correspond to the data by [Schmitt77].

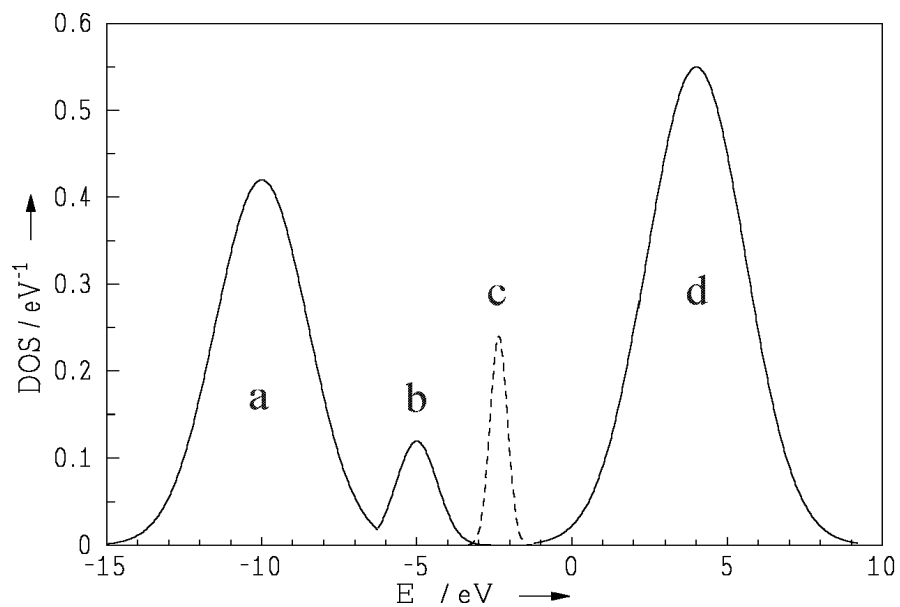


Fig. 6.4 Schematic electronic density of state of a $M_x(MX)_{1-x}$ melt [Koslowski97]: a: valence band, b: F-center ground state, c: F-center excited state, d: conduction band.

The main results of the optical studies of salt-rich M-MX melts can be summarised as follows [Nattland93, 95]: 1. with increasing metal mole fraction an additional absorption component with a peak position at slightly higher energies becomes visible. 2. a back ground absorption which is characterised by very weak dispersion.

The latter is assigned to a Drude electron like absorption (see section 2.1.2) with a mobility of the order of $0.1 \text{ cm}^2 \text{ V}^{-1} \text{ s}^{-1}$. This is consistent with direct measurements of the mobility [Haarberg88].

6.3.2 F-centers in $(\text{CeI}_2)_x(\text{CeI}_3)_{1-x}$ melts?

The fundamental absorption edge of $(\text{CeI}_2)_{0.06}(\text{CeI}_3)_{0.94}$ melts is also characterised by an exponential energy dependence and the analysis with the Urbach relation yields $\gamma = 0.665 \pm 0.005$, $K_0 = (6.2 \pm 0.3) \times 10^4 \text{ cm}^{-1}$ and $E_0 = 3.0 \pm 0.1 \text{ eV}$, which is in good agreement with the CeI_3 melt (see Table 6.4).

In analogy to optical spectra of M-MX melts the hypothesis of these studies on the Ce-systems was that F-center like states should exist within the energy gap between halogen valence band and metal conduction band – see the density of state (DOS) of a $\text{M}_x(\text{MX})_{1-x}$ melt in Fig. 6.4. However, a striking result of the optical spectra of $(\text{CeI}_2)_x(\text{CeI}_3)_{1-x}$ melts is that there is no significant F-center like absorption in the range 0.5 – 3 eV up to $x = 0.26$. The ionic distance R_{+-} ($\sim 3.2 \text{ \AA}$) is comparable to those of $\text{Cs}_x(\text{CsBr})_{1-x}$ (3.15 \AA) or $\text{Cs}_x(\text{CsI})_{1-x}$ (3.34 \AA) melts so that an absorption at $\sim 1 \text{ eV}$ could be expected (0.98 and 0.85 eV for the CsBr and CsI systems, respectively). This fact demonstrates that no strongly localised states like F-centers exist in these melts with excitation energies below 3 eV.

A possibility might be that defect species would exist as weakly localized mobile electrons which should contribute a very flat Drude type absorption in the spectra, as described in the previous section. This is, however, not plausible since the absorption constant in the visible range stays constant with variation of diiodide doping – see Fig. 5.15.

6.3.3 Optical properties of the Nd and Eu systems

For heavier metal halide systems the influence of electron transfer between different oxidation states, Intervalence Charge Transfer (IVCT), has to be considered [Stöhr99]. In general, the

absorption spectra of IVCT are characterised by a slightly asymmetric Gaussian with a clearly higher oscillator strength compared to parity forbidden transitions, e.g. d-d or f-f excitations. In this section the optical spectra of neodymium and europium halide melts are interpreted by the “small polaron model” which describes the electron transfer of class II of mixed valence compounds in the terminology by Robin and Day (see section 2.4).

6.3.3.1 Interpretation of optical spectra of $(\text{NdI}_2)_x(\text{NdI}_3)_{1-x}$ mixtures

The optical spectra of molten $(\text{NdI}_2)_x(\text{NdI}_3)_{1-x}$ mixtures consist of 1. Urbach tail, 2. f-f transitions, and 3. a broad band at ~ 1.5 eV. As for the broad band, there are two possibilities for interpretation, i.e. 1. 4f-5d transition, 2. IVCT band. For this aim the spectra have been fitted by a Gaussian and an exponential Urbach type function. As shown in Fig. 6.5 the spectrum is reasonably described by these two functions except the additional f-f transitions. From this fitting the half width of the Gaussian band is determined to be ~ 1.5 eV, and its intensity increases by ~ 40 % with increase of temperature by 200 K. These features are not consistent with a 4f-5d excitation, since it is characterized by a clearly reduced band width less than 0.5 eV (e.g. see Fig. 5.3 for the optical spectra of neodymium chloride) and by a decreasing band intensity with increasing temperature [Potapov00]. On the other hand, as discussed in chapter 5.2.1, an electron exchange between different oxidation states should lead to a maximum at the concentration of $[\text{Nd}^{2+}]: [\text{Nd}^{3+}] = 1:1$.

An open problem is that spectra of nominally pure NdI_2 melt exhibit characteristics similar to those of $(\text{NdI}_2)_x(\text{NdI}_3)_{1-x}$ mixtures – see Fig. 5.13. The reason is still not yet clear. However, it has to be noted that a partial disproportionation of the salt, i.e. $3\text{NdI}_2 \leftrightarrow 2\text{NdI}_3 + \text{Nd}$, or a slight contamination by oxide impurities cannot be excluded. Furthermore, in the synthesis of NdI_2 small amounts of NdI_3 may remain which has been shown by Raman measurements of solid NdI_2 [Rodriugez B. 02]. This may lead to a Nd^{3+} concentration high enough to show the broad band. It should be also noted here that solid NdOI shows a very similar optical absorption spectrum [Haire80].

Another possibility of the apparent coexistence of Nd^{3+} ions in NdI_2 melt may be that discussed for the high-pressure modification of crystalline NdI_2 [Beck76, 92]. According to the p,T diagram of NdI_2 , the fields of existence of NdI_2 -I (salt-like, SrBr_2 structure) and NdI_2 -II (metallic character, Ti_2Cu structure) are separated by a coexistence line with negative slope.

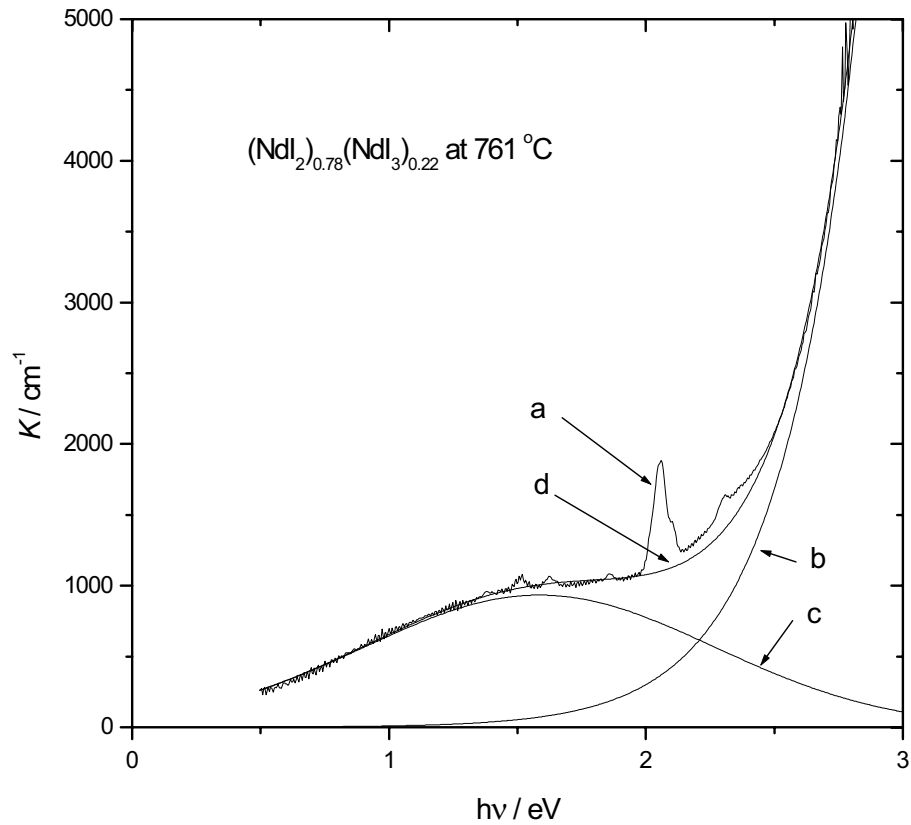


Fig. 6.5 Fitting result of $(\text{NdI}_2)_{0.78}(\text{NdI}_3)_{0.22}$ melt at $761\text{ }^\circ\text{C}$ through an Urbach term (b) and a Gaussian (c). (a) is original spectrum and (d) is summation of (b) and (c).

Extrapolation of this line yields a similar transition under ambient pressures at $\sim 500\text{ }^\circ\text{C}$. Though such a transformation has not been observed for solid NdI_2 yet, it might happen under the present experimental conditions, leading to the NdI_2 -II phase with the apparent chemical formula of $\text{Nd}^{3+} \cdot \text{e}^- \cdot (\text{I})_2$.

In conclusion, we may assign the broad band at 1.5 eV in $(\text{NdI}_2)_x(\text{NdI}_3)_{1-x}$ mixtures to an IVCT excitation, although there are some unclear points concerning the spectra of pure NdI_2 . In order to discuss the IVCT excitation more quantitatively the “two-site small polaron model” is introduced in the following section, which will be used for the analysis of the optical absorption spectra of $(\text{NdI}_2)_x(\text{NdI}_3)_{1-x}$ mixtures. For the details of the small polaron theory and its optical properties readers are referred to [Böttger85, Emin93, He95, Kuznetsov98].

6.3.3.2 Two-site Small Polaron Model

A polaron is a quasi particle where an electron strongly polarizes its surrounding through strong electron phonon coupling. As an example, an electron which is induced in an alkali halide crystal distorts the lattice. This distorted field follows with the motion of the electron, so that the effective mass of the electron increases considerably. The system lowers its energy through the polarization by an amount, E_p , so-called polaron shift, and the electron tends to localise. On the other hand, the kinetic energy of the system attempts to remove the carrier and tries to delocalise the electron. The competition of these two factors determines the size of a polaron. Since the kinetic energy is approximately equal to the resonance integral, J , the formation of a polaron whose radius is small compared to the lattice constant (small polaron) requires the condition $J/E_p \ll 1$. The investigation of small polarons has been especially stimulated by the experimental findings of a number of materials with low electronic mobilities. For such a compound the transport properties are not understood by the usual band model. The dominant electron transport can be described by thermally activated jumps of the carries from site to site.

In the theory of small polaron the following three dimensionless parameters are important for the classification:

1. $\eta_1 = J / E_A$, where J is the resonance or exchange integral and E_A is the thermal activation energy. Since the polaron shift is related to the thermal activation energy by $E_p \sim 2E_A$, this parameter is the measure of localisation of electrons. The system with $\eta_1 \ll 1$ corresponds to the small polaron, and that with $\eta_1 \gg 1$ is called large polaron.
2. $\eta_2 = J^2 / (\hbar\omega_{op}\sqrt{E_A kT})$, where ω_{op} is the phonon frequency within the Einstein model for phonons. This parameter is regarded as a parameter of adiabaticity and characterises the mechanism of an electron hopping from a lattice site to the next site. In the case of $\eta_2 > 1$, the probability for non-adiabatic hopping is small so that electron transfer occurs adiabatically from one site to the next neighbour. On the other hand, for $\eta_2 \ll 1$, it occurs non-adiabatically. The term ‘‘adiabaticity’’ will be explained below.
3. $\eta_3 = J^2 / E_A kT$, which characterises the hopping range of electron. For $\eta_3 \ll 1$, hopping occurs practically only between the nearest-neighbour sites.

For typical rare earth compounds $\eta_1, \eta_2, \eta_3 \ll 1$ is expected because of the narrow 4f band (small J). Especially for small η_3 the system can be treated by the ‘‘two-site model’’.

Assuming all ions vibrate with a single frequency, ω_{op} , (Einstein model), the classical Hamiltonian of the two-site model reads

$$H = \frac{M}{2}(v_1^2 + v_2^2) + \frac{M}{2}\omega_{op}^2(x_1^2 + x_2^2) + A(x_1 - x_2)(a_1^+ a_1 - a_2^+ a_2) + J(a_1^+ a_2 + a_2^+ a_1) \quad (6.5)$$

where M is the mass of a vibrating ion, x_i is the displacement of the i -th ion from its equilibrium position, $v_i = dx_i/dt$ (t : time), A is a constant describing the coupling between the electron and the lattice, a^+ and a are creation/annihilation operators, respectively.

From the adiabatic or static phonon approximation the energy levels of the two-site system are given in terms of the coordinate $x = x_1 - x_2$, which describes the relative motion of the ions, by:

$$E_{\pm} = \frac{\omega_{op}^2 M}{4} x^2 \pm \sqrt{A^2 x^2 + J^2} \quad (6.6)$$

Fig. 6.6 shows the energy levels as a function of x . This potential profile can be understood in the following way.

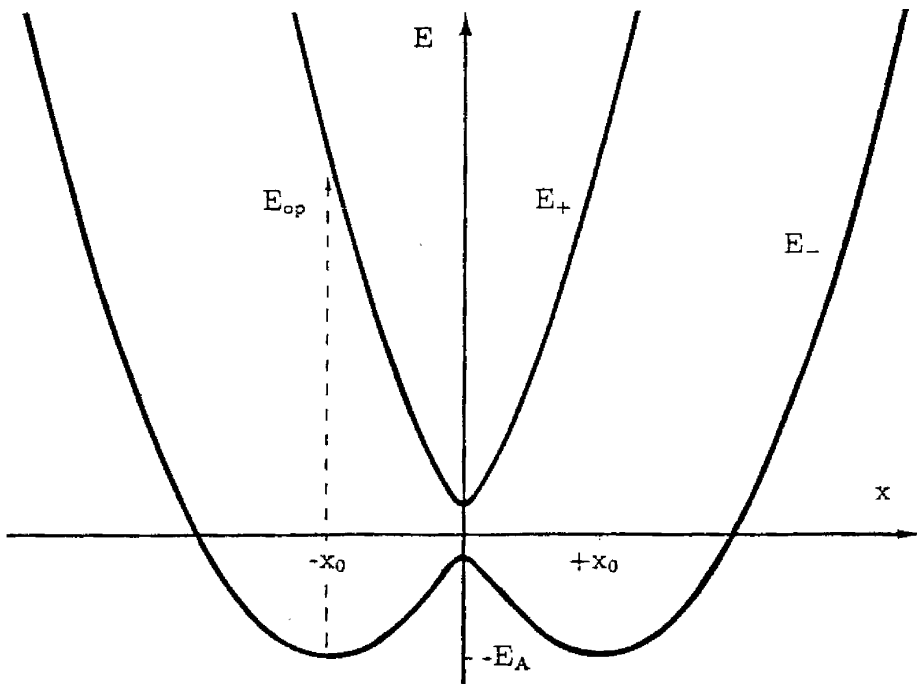


Fig. 6.6 The adiabatic levels E_+ and E_- in the two-site model in dependence of the relative displacement of the ions, x . The minimal distance between E_+ and E_- at $x = 0$ is equal to $2J$. When J is large enough, an electron delocalises between the sites – see also Fig. 2.2.

For the hypothetical case in which no extra electron is considered in the two-site system, both sites consist of Ln^{3+} ions and have the parabolic profile with one minimum ($E = 0$) at $x = 0$ from harmonic oscillator approximation. When an extra electron is brought to the system, there are two possibilities for the localization either at left site ($-x_0$) or at right site ($+x_0$). The resonance integral, J , scales the degree of electron delocalisation at $x = 0$. The adiabaticity is important for the electron transfer process at $x = 0$.

When the system reaches $x = 0$ with small but finite probability due to statistical fluctuation, the system can either non-adiabatically pass from E_- to E_+ and the electron is eventually transferred to the other side, or overcome the maximum at $x = 0$.

The former corresponds to the non-adiabatic transition ($\eta_2 \ll 1$), and the latter adiabatic ($\eta_2 > 1$). The hopping mobility, u_h , is given by

$$u_h = u_0 \frac{1}{2\pi} \frac{\hbar\omega_{op}}{kT} \exp(-E_A/kT) \times \begin{cases} 1 & \text{for } \eta_2 > 1 \\ \pi^{3/2} \eta_2 & \text{for } \eta_2 \ll 1, \end{cases} \quad (6.7)$$

where $u_0 = ea^2/\hbar$ is a constant and has the dimension of mobility with the hopping distance (also lattice constant), a . Thus, in the non-adiabatic case ($\eta_2 \ll 1$), the DC hopping conductivity, σ_h , becomes

$$\sigma_h = eu_0 n(1-f) \frac{\sqrt{\pi}}{2} \frac{J^2}{kT \sqrt{E_A kT}} \exp(-E_A/kT), \quad (6.8)$$

where n is the concentration of the charge carriers, and f is the Fermi distribution function, i.e. $f = \{\exp(-\mu/kT) + 1\}^{-1}$, (μ : chemical potential of electron).

6.3.3.3 Optical properties of small polaron model

Within the two-site model the frequency dependence of the electrical conductivity, i.e. optical conductivity, $\sigma(\hbar\omega, T)$, is derived through the Kubo formula and yields for the real part

$$\sigma'(\hbar\omega, T) = eu_0 n_L (1-f) \frac{\sqrt{\pi}}{2} \frac{J^2}{\sqrt{E_A kT}} \frac{1 - \exp(-\hbar\omega/kT)}{\hbar\omega} \exp\left\{-\frac{(\hbar\omega - 4E_A)^2}{16E_A kT}\right\}. \quad (6.9)$$

Thus, the absorption constant K for small polaron model is derived from eqns. (6.9) and (2.10).

The formula (6.9) describes a weakly asymmetric Gauss function with the absorption peak at $\hbar\omega = E_{op} = 4E_A$, see Fig. 6.6. Furthermore, with increasing temperature the width of the absorption band increases – so called phonon broadening, and the peak position shows a red shift.

6.3.3.4 Analysis of absorption spectra of $(\text{NdI}_2)_x(\text{NdI}_3)_{1-x}$ melts

In order to perform the fitting of the spectra with the small polaron formula, eqn. (6.9) is modified as

$$K_{pol}(\hbar\omega) = \frac{\sigma'(\hbar\omega)}{n\epsilon_0 c} = \frac{A}{\sqrt{E_A kT}} \frac{1 - \exp(-\hbar\omega / kT)}{\hbar\omega} \exp\left\{-\frac{(\hbar\omega - 4E_A)^2}{16E_A kT}\right\}, \quad (6.10)$$

where A denotes a parameter that combines the pre-factors in eqn. (6.9). Hence, the fitting model function is

$$K(\hbar\omega) = K_{\text{Back}} + K_{\text{urb}}(\hbar\omega) + K_{\text{pol}}(\hbar\omega), \quad (6.11)$$

where K_{Back} is the correction for a constant background, K_{urb} is the Urbach term, eqn. (6.1).

The fit result of the $(\text{NdI}_2)_x(\text{NdI}_3)_{1-x}$ spectra is very similar to that in Fig. 6.5, namely a very broad polaron band at ~ 1.6 eV and an Urbach tail toward the UV range.

The temperature variation of the fitting results are presented in Fig. 6.7 and the obtained Urbach parameters are summarised in Table 6.5. The activation energy decreases slightly with increasing temperature, in accordance with the prediction of small polaron model. The exception at 950 °C may be due to the strong overlap of the Urbach curve (see Fig. 5.11), leading to a large uncertainty in the peak position of the polaron band. An anomaly at this temperature is also found in the integrated intensity of the hypersensitive transition (Fig. 6.8). The value of E_A (~ 0.4 eV) is in good agreement with the experimental value from the recent electrical conductivity measurements [Zein El Abedin02]. The parameters, E_A and A , will be further considered in the discussion of the transport properties and electron dynamics of the present system in later sections.

Table 6.5 Summary of Urbach parameters of $(\text{NdI}_2)_x(\text{NdI}_3)_{1-x}$ melts. See text for details.

Composition	NdI_3	$(\text{NdI}_2)_{0.78}(\text{NdI}_3)_{0.22}$		NdI_2
Temp. range / °C	799-951	566-738	751-957	733-932
K_0 / cm^{-1}	$(6.0 \pm 0.2) \times 10^4$	$(4.7 \pm 0.8) \times 10^4$	$(2.4 \pm 0.4) \times 10^4$	$(1.6 \pm 0.1) \times 10^5$
γ	0.44 ± 0.01	0.54 ± 0.02	0.28 ± 0.02	0.36 ± 0.02
E_0 / eV	4.0 ± 0.1	3.8 ± 0.1	3.3 ± 0.1	3.65 ± 0.1

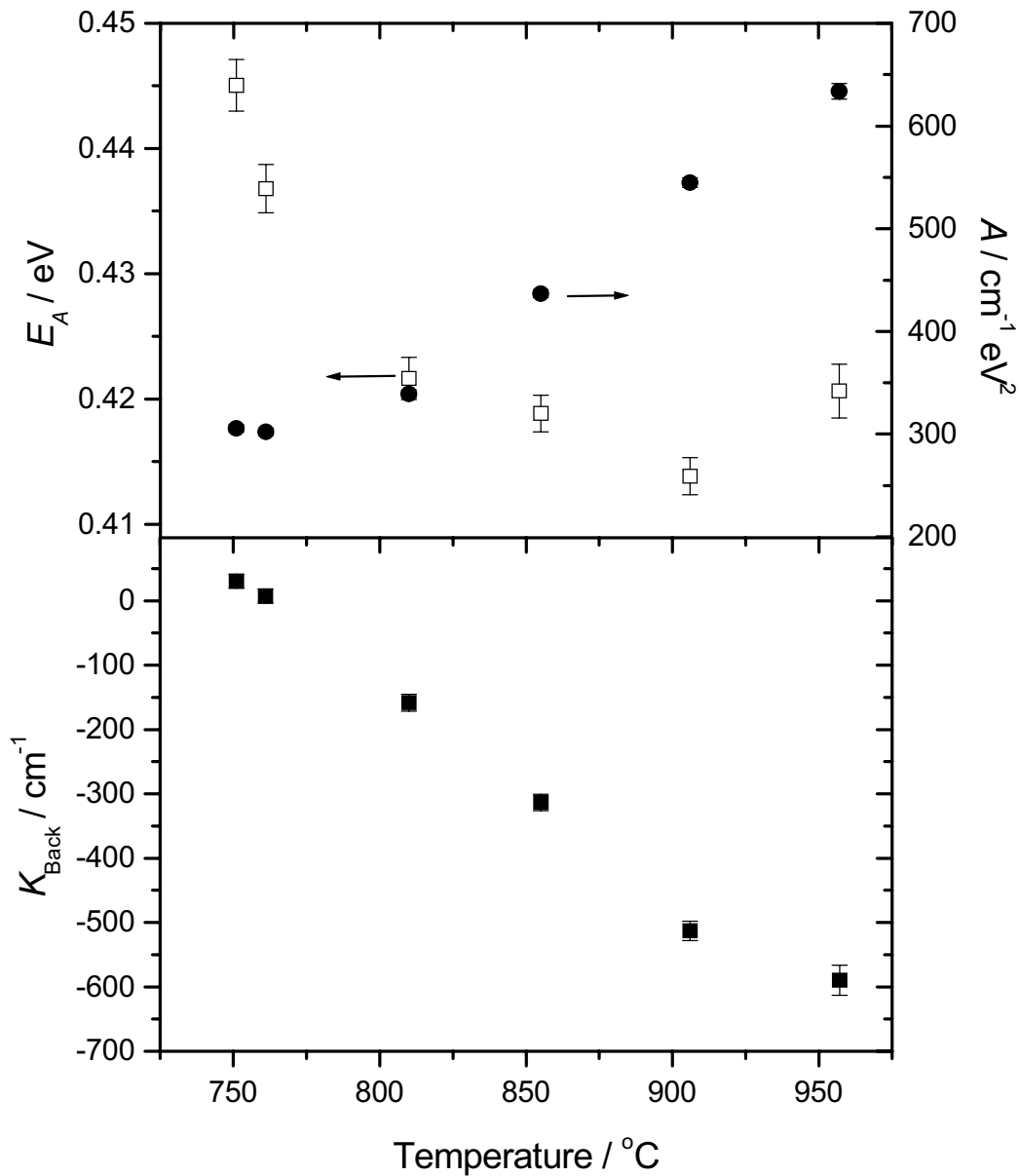


Fig. 6.7 Temperature dependence of fitting parameters of small polaron band in the optical spectra of $\text{Nd}_{0.78}(\text{NdI}_3)_{0.22}$ melt. The error bars refer only to the fitting analysis.

The linear dependence of K_{Back} is an interesting observation. It is unlikely that the reduction of background constant with temperature is due to the change of optical path length by the thermal expansion and squeezing of the Ta sealing wire at higher temperatures, since the spectra were reproduced with several heating and cooling cycles. Furthermore, the background corresponding to 600 cm^{-1} obviously exceeds the reflection correction due to the different media in the sapphire cell - see chapt. 4.3.3. In the light of this unexplained effect, the increase of A in Fig. 6.6 is very uncertain. The spectra of mixtures at lower temperature

(566-738 °C, see Fig. 5.11) are well described by a combination of a linear function ($K(\hbar\omega) = (170 \pm 70)\hbar\omega + (340 \pm 60)$), and an Urbach curve. These Urbach parameters are also included in Table 6.5. It is interesting that the values of the optical gap, E_0 , and constant γ of NdI₂ doped melt are lower than those of pure NdI₃ (except those of mixtures in the low temperature range). The rather large shift of optical gap at 740 °C will be discussed in the following section.

6.3.3.5 Hypersensitive transition and spectral change in NdI₂ containing melts

In Fig. 6.8 the integrated intensity of the hypersensitive transition of Nd³⁺ ion at different concentrations and temperatures is plotted. With increasing temperature a continuous increase of the integrated intensity is found similar to the example of pure NdI₃ melt within the experimental uncertainty. Furthermore, it increases with raising the diiodide content. Because of the absence of density data for NdI₂ containing melts the oscillator strength cannot be estimated. The density of crystalline NdI₂ and NdI₃ can be estimated from X-ray structure data as 5.46 and 5.81 g cm⁻³, respectively [Beck76, 79]. Thus, if both the density change upon melting and the temperature dependence of density of the NdI₂ containing system are comparable to pure NdI₃, the oscillator strength should have the same tendency as the integrated intensity. This implies that the local structure around the rare earth ions changes continuously towards the pure NdI₂ melt. Further investigation of f-f electronic transitions in conjunction with Judd-Ofelt theory (chapt. 2.3.4) will give us useful information on the local structure or complex formation in the present system.

Another striking feature of the optical spectra of (NdI₂)_x(NdI₃)_{1-x} melts is the discontinuous change in the liquid phase at ~ 740 °C – see Fig. 5.11. This is clearly demonstrated in the jump of E_0 , a change of the spectral shape of the f-f transition, and the appearance/disappearance of the polaron band. As for the first point, the absorption constant at higher energy is smaller for $T < 740$ °C than in the higher temperature spectra. This may indicate a partial solidification, which leads to the f-f transition of solid phase [Gruen66] and apparent “terrace” effect in spectra. However, the temperature at which this change occurs is obviously higher than the liquidus temperature, and the background constant should also jump to higher values because of the scattering of light in polycrystals when the melt is solidified. On the other hand, the integrated intensity of hypersensitive band does not show a remarkable change within the experimental errors (Fig. 6.8). Haire *et al.* reported the optical absorption

spectra of solid NdI_3 [Haire80]. Through the noticeable spectral change a conversion from orthorhombic to hexagonal conversion was observed at 600 ± 30 °C. Whether such a conversion really exists in the liquid phase - further investigation on the structure of this system should clarify the type of this peculiar phase transition.

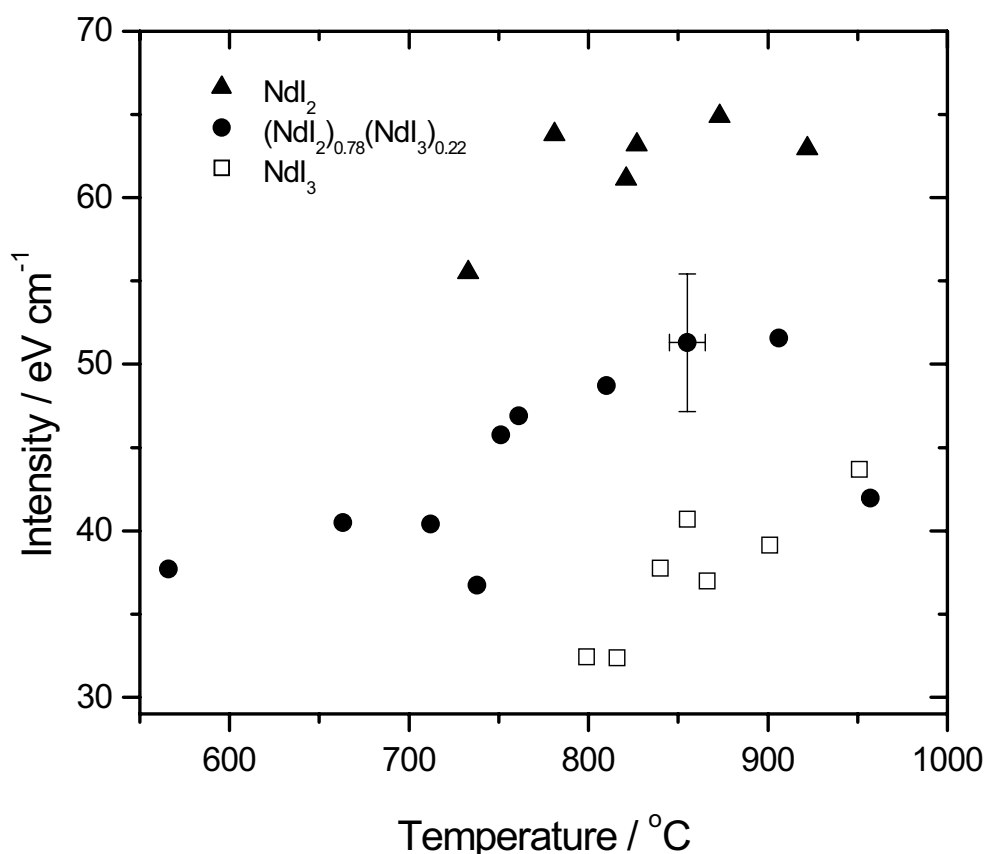


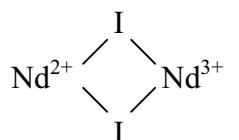
Fig. 6.8 Temperature dependence of integrated intensity of the hypersensitive transition for Nd^{3+} ion (${}^4\text{I}_{9/2} \rightarrow {}^4\text{G}_{5/2}$).

6.3.3.6 Comparison with the neodymium chloride systems and the role of eutectic melt

As presented in sections 5.1.1, 5.2.1 and 5.3, the reflectivity data of $\text{Nd}_x(\text{NdCl}_3)_{1-x}$ melts show a broad band at ~ 1.5 eV which may be assigned to an IVCT band. On the other hand, in the absorption spectra of $(\text{NdX}_2)_x(\text{NdX}_3)_y - (\text{LiX-KX})_{\text{eut}, 1-x-y}$ the intensity of a band at ~ 2.5 eV shows a maximum at the concentrations of $x = y$. It is of considerable interest to compare these data with the iodide system discussed above. On the one hand, the peak position of the IVCT band for the $(\text{NdI}_2)_x(\text{NdI}_3)_{1-x}$ melts, $\hbar\omega = 4E_A \sim 1.6$ eV, is comparable to that of the

broad band of reflectivity data of the chloride melt. On the other hand, these differ by ~ 1 eV from that observed in mixtures with alkali halide eutectic melts.

The occurrence of an IVCT always involves the intermediate state through a bridging ion/compound, like D-B-A where D, B and A denote, respectively, electron donor, bridge compound and electron acceptor – see Fig. 2.2. The higher optical excitation energy in the eutectic melts, therefore, may be due to the weaker interaction of the neodymium complexes in the salt matrix. This has been examined by the analysis of the ligand field strength parameter – see 5.2.1. Furthermore, as mentioned in section 6.1, the structural data suggest that with increasing rare earth halide concentration the rare earth complexes share their edges and form a loose network structure. If this network formation is also applicable to the mixture of Nd^{2+} and Nd^{3+} , the above mentioned intermediate state would have the form of edge sharing of octahedra, i.e.



Further experiments, e.g. Raman study, are needed to examine the complex formation of neodymium di- and trivalent cations.

6.3.3.7 Europium chloride melts

Absorption spectra of europium chloride melts are characterised by a monotonous increase of absorption towards higher energies, presumably a combination of Urbach and extra absorption band. However, a deconvolution analysis according to the Urbach relation and an appropriate function corresponding to the IVCT can be hardly performed.

One interesting observation is that the spectra of polycrystalline solids show a weak but clearly noticeable absorption peak around 1.5 eV. Lange reported the absorption spectra of mixed valence europium chloride crystals [Lange92]. The absorption at ~ 2 eV was assigned to the IVCT band with the characteristic optical features of the small polaron band, i.e. red shift and band broadening with increasing temperature. In addition, its intensity decreases

with temperature. With further increase of temperature the peak position shows a slight blue shift above the temperature of the solid – solid phase transition (~ 230 °C)⁵.

From these experimental findings polaron band in liquid phase may overlap strongly with the fundamental absorption, so that it cannot be clearly resolved in the visible range. In order to clarify the electronic properties of this system, further experimental studies are needed, e.g. electronic conductivity and mobility measurements.

In the final section optical and ESR data will be discussed in terms of the transport and dynamic properties of IVCT, and will be compared with the existing data for polyvalent halide melts.

6.4 Intervalence charge transfer and electron dynamics

6.4.1 Hopping conduction and Electronic mobility

From eqns. (6.8) and (6.10) the hopping conductivity for the small polaron system is given by

$$\sigma_h = n\varepsilon_0 c \frac{A}{kT \sqrt{E_A kT}} \exp(-E_A / kT). \quad (6.12)$$

Fig. 6.9 shows recent results of the electronic conductivity, σ_{elec} , which has been determined from the measured electrical conductivity, σ_{total} , with the assumption of a linear concentration dependence of the ionic conductivity, σ_{ionic} , between the limits of NdI₂ and NdI₃, respectively, i.e. $\sigma_{\text{elec}} = \sigma_{\text{total}} - \sigma_{\text{ionic}}$ [Zein El Abedin02]. The temperature dependence of hopping conductivity evaluated from eqn. (6.13)⁶ and parameters obtained through the fitting of the absorption spectra of a (NdI₂)_{0.78}(NdI₃)_{0.22} melt is also included in the figure.

It is remarkable that the magnitude of σ_h of $1 \Omega^{-1} \text{ cm}^{-1}$ is in good agreement with the measured conductivity data. This result, together with the agreement of the thermal activation energy both from electrical and optical measurements, supports the occurrence of IVCT in the present system.

From eqn. (6.7) it is possible to estimate the mobility of this melt through:

⁵ Similar change of red/blue shift was observed for mixed valence Yb chloride compounds close to this phase transition [Haselhorst94], though Haselhorst concluded that the blue shift was not clearly confirmed because of the experimental uncertainty.

⁶ The refractive index of 1.9 (see section 6.2.1) is used for the calculation of σ_h .

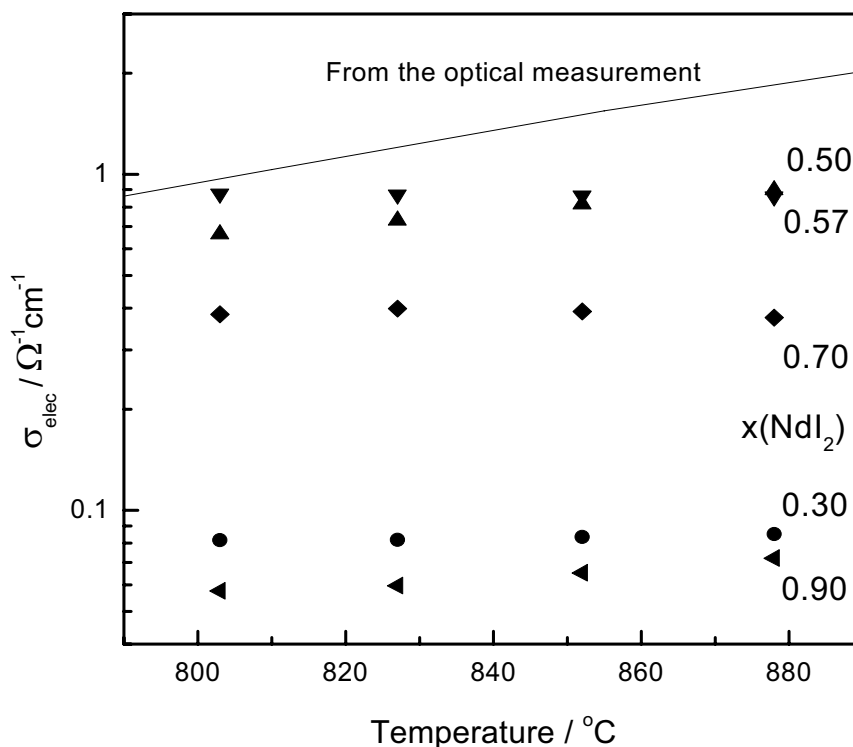


Fig. 6.9 Temperature dependence of electronic conductivity of $(\text{NdI}_2)_x(\text{NdI}_3)_{1-x}$ melts with different NdI_2 compositions [Zein El Abedin02]. The line gives an estimate of the hopping conductivity as determined from the optical absorption measurements of this work.

$$u_h = \frac{ea^2 \pi}{\hbar} \frac{J^2}{2kT\sqrt{E_A kT}} \exp(-E_A/kT) \quad \text{for } \eta_2 \ll 1. \quad (6.13)$$

For this purpose it is necessary to estimate the resonance integral, J .

Since J plays a central role in the polaron theory or, in general, electron transfer theory, its determination is of great interest. Hush derived the following formula in the framework of the two-site model by evaluating the transition dipole moment of IVCT bands [Hush67, 85]:

$$J = \frac{2.05 \times 10^{-2} \sqrt{\tilde{\nu} \Delta \tilde{\nu}_{1/2} \epsilon_{\max}}}{R_{MM}}, \quad (6.14)$$

where J is given in cm^{-1} , $\tilde{\nu}$ is wave number at the maximum of the IVCT band, ϵ_{\max} is its molar absorptivity, $\Delta \tilde{\nu}_{1/2}$ is the width at half maximum of the polaron band in cm^{-1} , R_{MM} is the distance between two metal sites in \AA . Though a difficulty arises in estimating the proper

R_{MM}^7 , taking R_{MM} as 3 \AA ($\sim \sqrt{2} \times R_{+}$ from the hypothetic structure of the intermediate state – see 6.3.3.6), we obtain a value of $J \sim 0.1 \text{ eV}$ which is in reasonable agreement with the typical value of polaron systems, e.g. 0.2 eV for TiO_2 [Kudinov69]. Moreover, the small value of J is in accordance with the assumption of small polaron theory.

Thus, from eqn. (6.14) and the above estimated J , $u_h \sim 0.02 \text{ cm}^2 \text{ V}^{-1} \text{ s}^{-1}$ is obtained at $800 \text{ }^\circ\text{C}$. This value is in qualitative agreement with recent direct measurements of u_h by the Wagner-Hebb polarisation method [Hermas99]. It is of the same magnitude as the electronic mobility in dilute M-MX solution [Haarberg88] or for the Ta(IV)-Ta(V) redox couple in alkali halide melts, where a mobility of $\sim 10^{-2} \text{ cm}^2 \text{ V}^{-1} \text{ s}^{-1}$ is found at $\sim 700 \text{ }^\circ\text{C}$ [Stöhr97, 99].

Finally it is of special interest to evaluate the hopping probability, W , for electron transfer between donor (Ln^{2+}) and acceptor (Ln^{3+}) which in the high temperature limit is given by:

$$W = \frac{2\pi}{h} J^2 \left(\frac{\pi}{4k_B T E_A} \right)^{1/2} \exp\left(-\frac{E_A}{k_B T}\right). \quad (6.17)$$

It determines the rate constant of electron transfer which was derived in the framework of the transition state formalism - so called Hush-Marcus formula [Hush85].

From the estimated value of J the rate constant results in 10^{12} s^{-1} at $800 \text{ }^\circ\text{C}$. This result will be compared with the relaxation time of ESR in the next section.

6.4.2 ESR relaxation time in $(\text{NdCl}_2)_x(\text{NdCl}_3)_y - (\text{LiCl-KCl})_{\text{eut}, 1-x-y}$ melts

Rare earth metal ions are characterized by strong spin-orbit coupling ($600\text{-}3000 \text{ cm}^{-1}$) which leads to a strong coupling of the spins to the lattice and very small spin relaxation times [Carrington67]. As a consequence the ESR lines are extremely broadened and typically can only be detected at very low temperatures⁸.

The ESR spectra observed here for neodymium chloride melts at elevated temperatures (see section 5.5) have a band width of the order of 10^3 G which is reduced with increasing temperature. This is indicative of exchange or motional narrowing of the resonances and the interesting question is: what is the magnitude of the electronic correlation time τ_c and how

⁷ For generalisation of the Hush formula as well as the recent studies of site distance dependence of IVCT bands – see review articles, e.g. [Launay01]

⁸ This is not the case for the system with S configuration, e.g. Gd^{3+} where ESR signals are observed at room temperature [Ayscough67].

does it compare with the corresponding estimate from the optical spectra and electronic conductivities. For this aim the microcrystalline model of McConnell is used [McConnell56] where the ions and their ligands are treated as a unit in solution. Based on the Raman data of $\text{LnX}_3\text{-MX}$ melt [Photiadis98] this assumption should be allowed for the present systems with dilute rare earth halide concentrations. Within the model and with the assumption of exchange narrowing, i.e. $\omega \tau_c \ll 1$, the ESR line width at half maximum is given by [Ayscough67]:

$$\frac{1}{T_2} \approx \Delta\omega_{1/2} \approx \frac{8\pi^2 (\Delta g g \mu_B B_0 + \Delta A I_z) \tau_c}{15h^2}, \quad (6.17)$$

where $g = (1/3)g_{\parallel} + (2/3)g_{\perp}$, $\Delta g = g_{\parallel} - g_{\perp}$ and $\Delta A = A_{\parallel} - A_{\perp}$

with g = g-factor, A = Hyperfine coupling constant, ω_0 = resonance frequency, μ_B = Bohr magneton, h = Planck constant, I_z = z-component of nuclear spin, and the subscripts, \parallel and \perp , mean, respectively, the component parallel (z-direction) and vertical to the static magnetic field, B_0 .

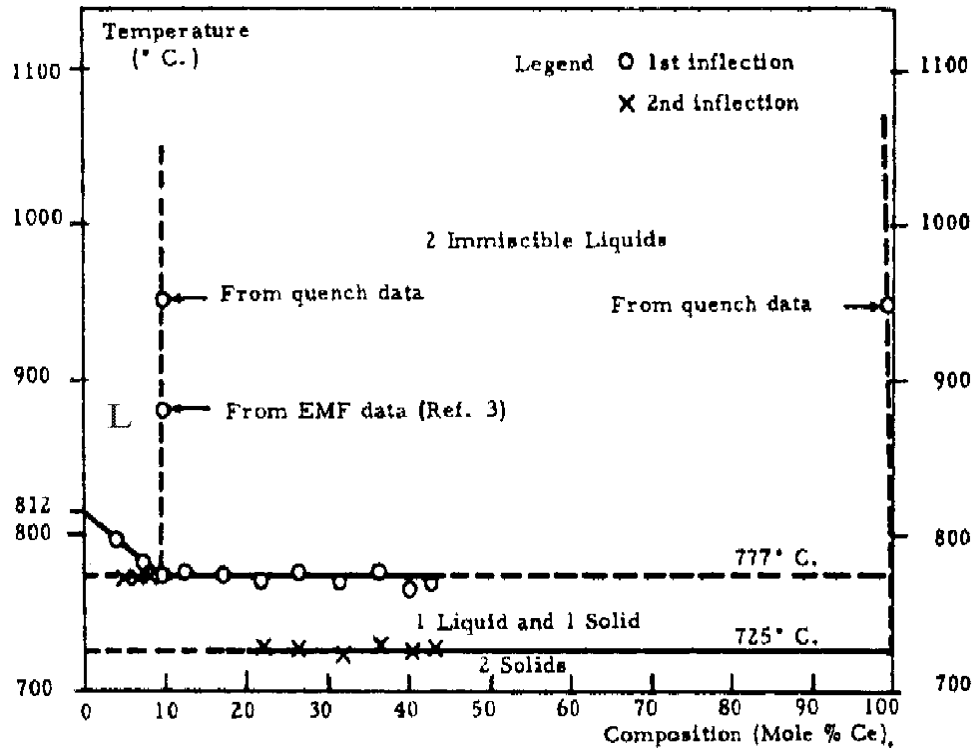
The values of Δg and ΔA can only be estimated from ESR data for Nd^{3+} ion in a LaCl_3 crystal at 4 K, see e.g. [Ayscough67]. This results in a value of $\tau_c \sim 10^{-12}$ s.

The value here is in good qualitative agreement with the electron transfer rate estimated from the optical data, i.e. $W \sim 10^{12}$ s $^{-1}$.

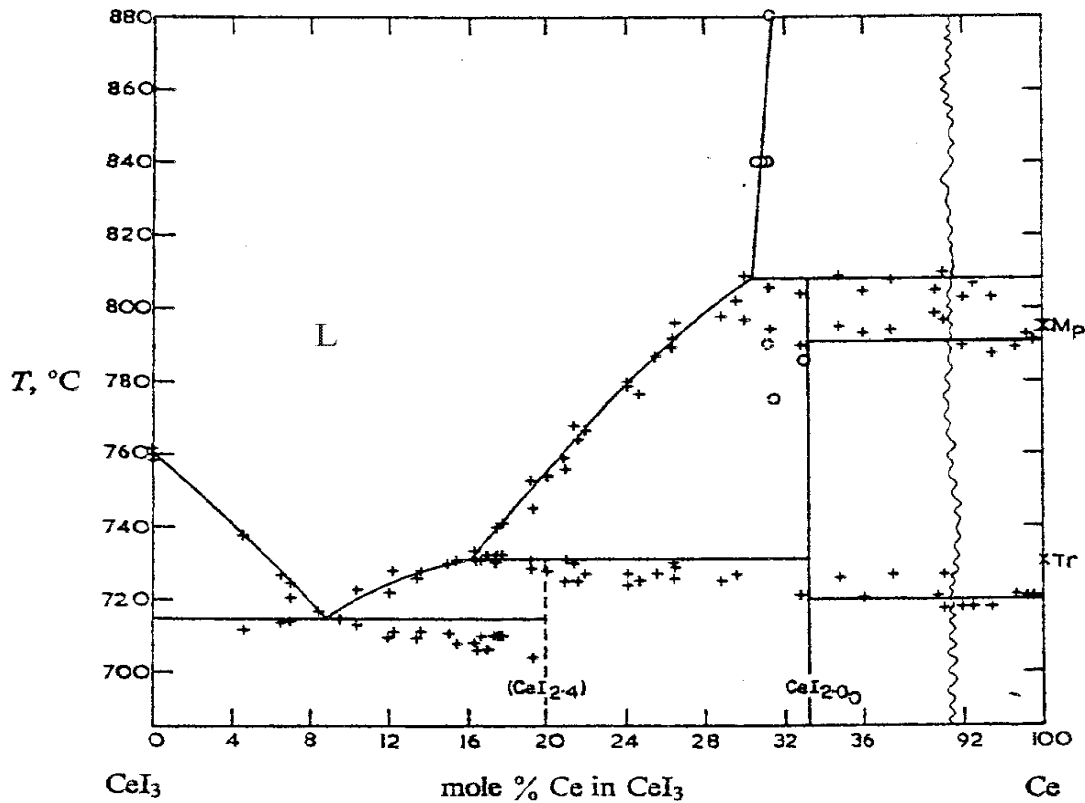
This discussion of the results of optical and ESR measurements for type 2 melts, together with the recent electrical conductivity measurements, support the interpretation of the experimental data by intervalence charge transfer between di- and trivalent rare earth ions occurring in the neodymium – neodymium halide systems. A simple two-site model can reasonably well describe the electronic charge transport properties of these melts. On the other hand, clear evidence for the europium melts has not been obtained in the present study because of difficulties with their corrosive properties as well as the instability of the trivalent halides. Crystalline mixed valent europium and ytterbium chlorides are well characterised by IVCT.

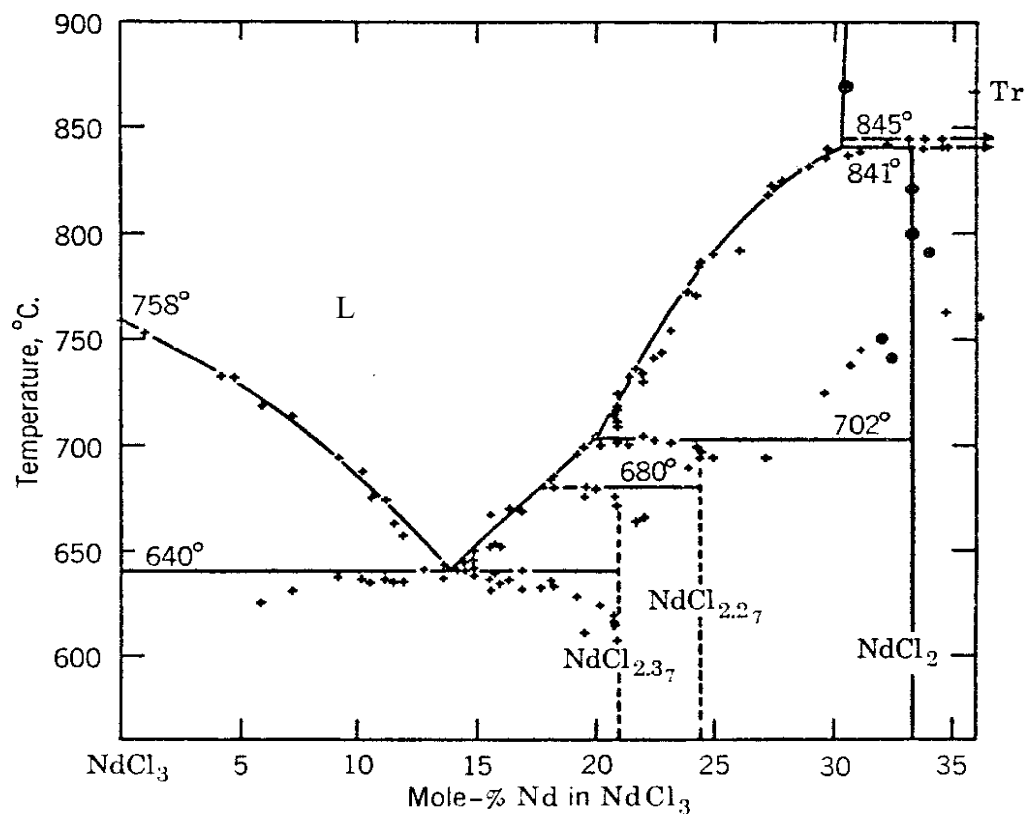
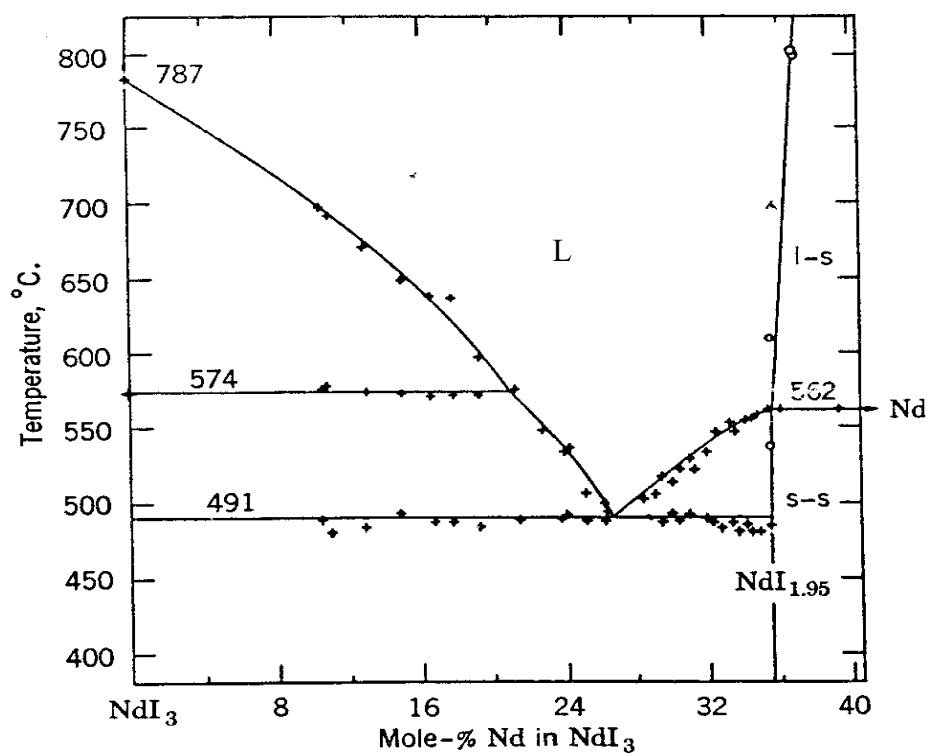
Appendix 1 Phase diagrams and literature data of selected compounds

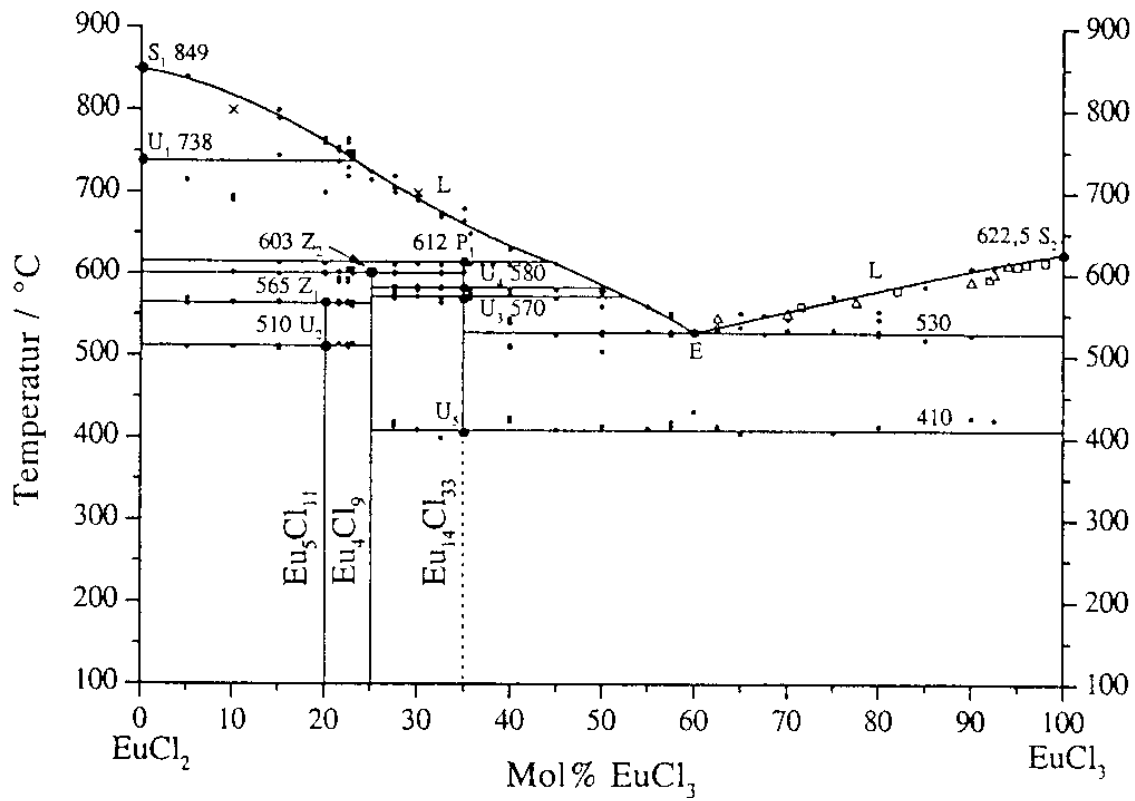
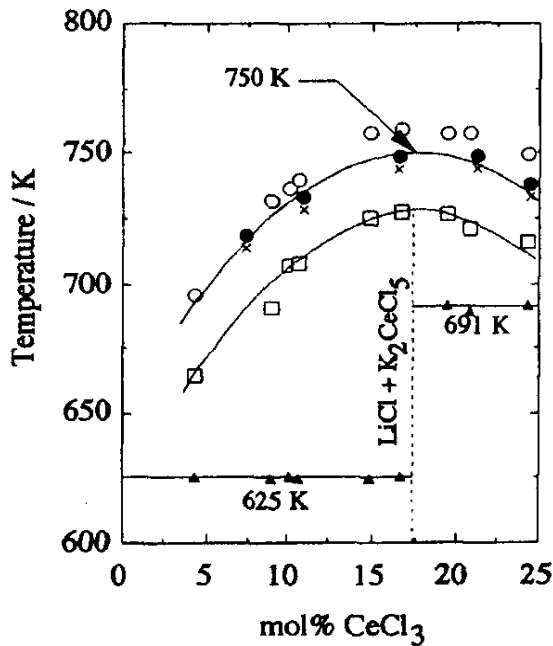
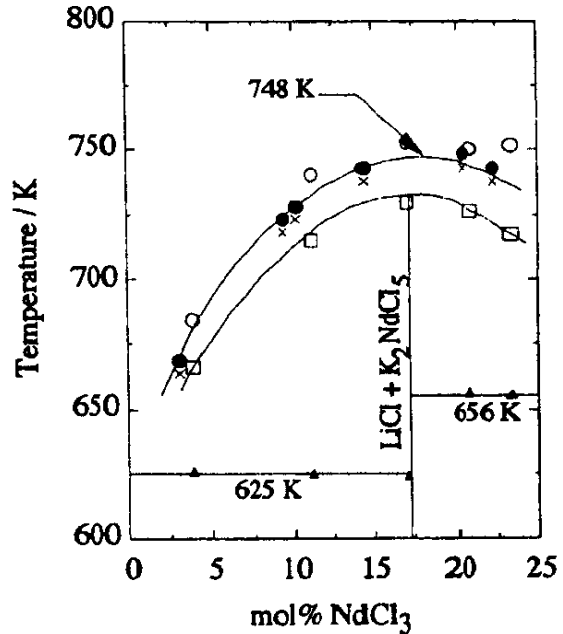
Ce - CeCl₃ [Mellors59]



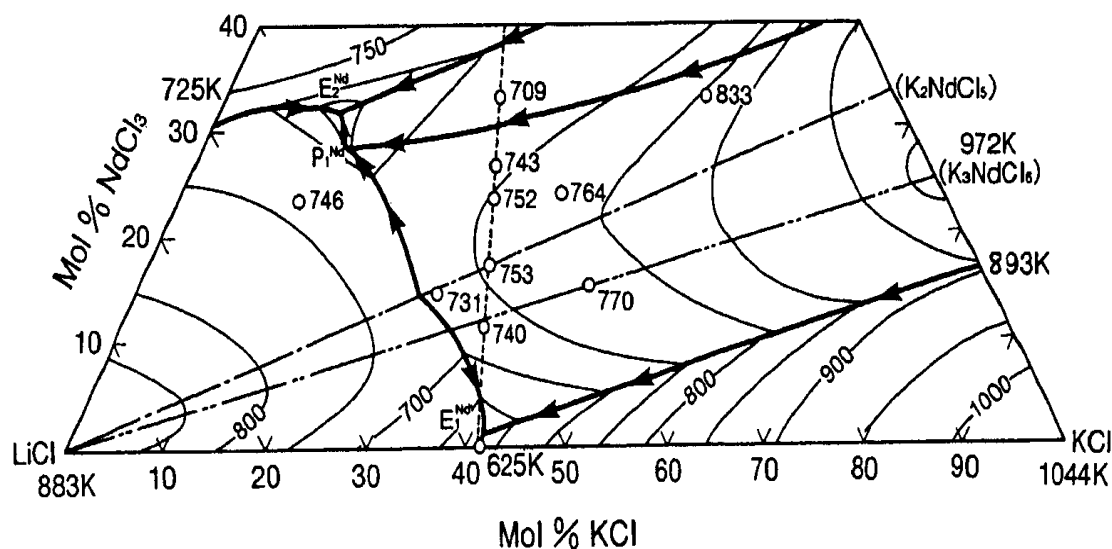
Ce - CeI₃ [Corbett61]



Nd – NdCl₃ [Bredig64, ref. therein]Nd – NdI₃ [Bredig64, ref. therein]

EuCl₂ - EuCl₃ [Oppermann00]CeCl₃ - (LiCl-KCl)_{eut}* [Nakamura97]NdCl₃ - (LiCl-KCl)_{eut}* [Nakamura97]

* The symbols \blacktriangle , \square and \circ indicate three types of transitions determined by thermal analysis and the symbols \bullet and \times indicate liquid and two-phase regions determined by visual observations.

NdCl₃ - LiCl - KCl [Nakamura97]**Density of melts**

Density, ρ , is given in (g cm^{-3}), T in ($^{\circ}\text{C}$).

LaCl ₃	$\rho = 4.0895 - 0.0007774 \cdot T$	[Janz67]
CeCl ₃	$\rho = 4.248 - 0.000925 \cdot T$	[Janz67]
NdCl ₃	$\rho = 3.751 - 0.000663 \cdot T$	[Gmelin82]

LaI ₃	$\rho = 5.1547 - 0.0011109 \cdot T$	[Kutscher74]
NdI ₃	$\rho = 5.1146 - 0.0010701 \cdot T$	[Kutscher74]

(LiCl-KCl) _{eut}	($x(\text{KCl}) = 0.415$)	$\rho = 1.8781 - 0.0005332 \cdot T$	[Smirnov82]
(LiI-KI) _{eut}	($x(\text{KI}) = 0.369$)	$\rho = 3.0951 - 0.000816 \cdot T$	[Janz77]

Electron affinity (eV) [CRC97]

Cl	3.61269
I	3.059038

Ionization energy E_i (eV) [CRC97]

	I	II	III
La	5.5770	11.060	19.1773
Ce	5.5387	10.85	20.198
Nd	5.5250	10.73	22.1
Eu	5.6704	11.241	24.92

Melting point of $(MX-M'X)_{eut}$ ($^{\circ}C$)

$(LiCl-KCl)_{eut}$ ($x(KCl) = 0.415$)	361	[Janz67]
$(LiI-KI)_{eut}$ ($x(KI) = 0.369$)	260	[Janz67]

For rare earth halides see the corresponding phase diagrams.

Standard enthalpy of formation, ΔH_f ($kJ\ mol^{-1}$) [Bratsch82, Cordfunke01, Kim79]

The values of dihalide were calculated from the corresponding Born-Haber cycles. See also [Johnson69b, Struck91].

Chlorides

$LaCl_3$	-1071.6 ± 1.5	$LaCl_2$	-493
$CeCl_3$	-1059.7 ± 1.5	$CeCl_2$	-555
$NdCl_3$	-1040.9 ± 1.0	$NdCl_2$	-693
$EuCl_3$	-935.4 ± 3.0	$EuCl_2$	-819

Iodides

LaI_3	-673.9 ± 2.0	LaI_2	-166
CeI_3	-666.8 ± 3.0	CeI_2	-294
NdI_3	-639.2 ± 4.0	NdI_2	-437
EuI_3	-538 ± 10	EuI_2	-578

Appendix 2 Optical absorption study of InCl_x melts

Mixed valence indium halides have been intensively studied over decades. Among the different mixed valent compounds of the In-X system (see phase diagram Fig. A2.1 for the In-Cl system) the “dihalide” does not form a stable compound with the divalent In ion, but is known to form the mixture of In(I) and In(III). Ichikawa and Warren and Warren *et al.* performed optical and NMR measurements of InX_x melts [Ichikawa79, Warren83]. They discussed the short-lived fluctuations to the paramagnetic In^{2+} state through single electron hopping from the diamagnetic $\text{In}^+ - \text{In}^{3+}$ configuration. An optical absorption band around 2.1 eV with an absorption constant of $\sim 5 \text{ cm}^{-1}$ ($\epsilon_{\text{max}} \sim 0.14 \text{ cm}^2 \text{ mol}^{-1}$ and the line width $\Delta_{1/2} \sim 0.2 \text{ eV}$) was assigned to the IVCT band in an InCl_2 melt. From the NMR data and Hush formula (eqn. 6.13) they estimated resonance integral of $J \sim 0.001 \text{ eV}$ and the correlation time of the order of $1 \mu\text{s}$, resulting in a considerably low electronic conductivity, i.e. $\sigma_e \sim 4 \times 10^{-8} \text{ S cm}^{-1}$, compared to the total conductivity $\sigma_{\text{total}} \sim 0.4 \text{ S cm}^{-1}$ of InI_2 at 500°C [Ichikawa79, 82 and references therein].

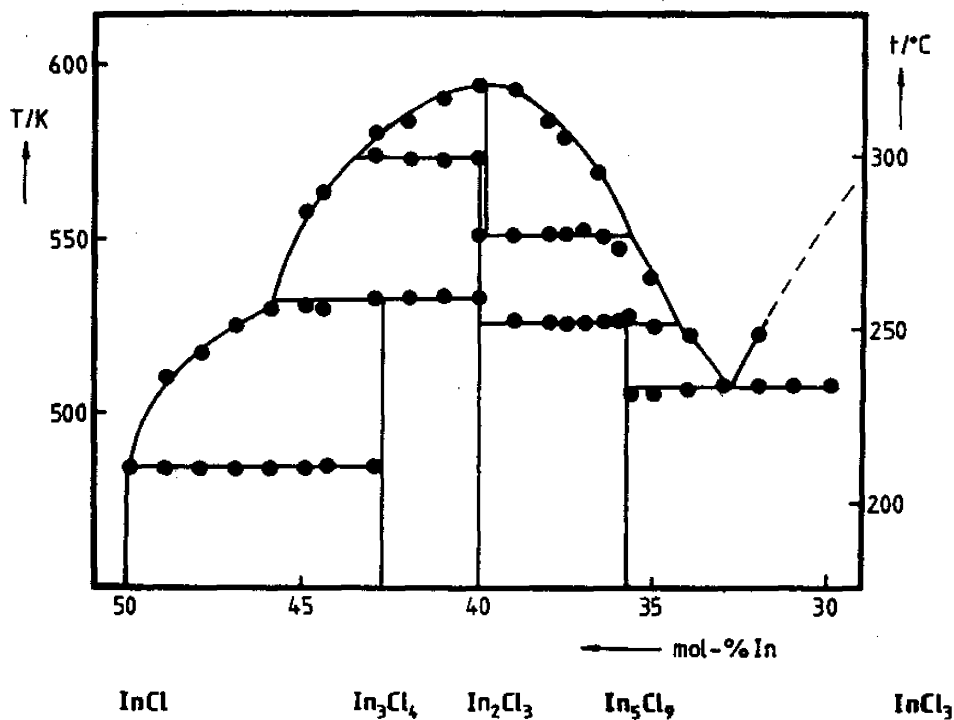


Fig. A2.1 Phase diagram of In-Cl system [Meyer83].

These values are considerably smaller than those of the neodymium system as discussed in chapter 6, reflecting the different behaviour of the electrical conductivity as a function of metal composition. While the Nd-NdI₃ melts show a parabolic concentration dependence, that of In-InI₃ melt shows a linear increase [Ichikawa82]. In order to get further insight to the transport properties of these systems, optical absorption measurements have been re-examined. In this appendix optical absorption spectra are reported.

Experiments

Samples of InCl_x have been prepared by reaction of the proper amount of In metal (Alfa) and InCl₃ (Alfa) in sealed quartz ampoules. The purifying of InCl₃ has been performed in the similar way as described in the literature [Warren83], namely the drying of salt at 200 °C and the double sublimation with the apparatus used for the rare earth halides. After the first sublimation candy floss like grey materials were separated.

Optical absorption measurements have been performed with the same vacuum chamber and spectrometer that have been used for the measurements of the rare earth halide systems.

The quartz cells consist of the optical transmission cell with path length of 1 mm (Hellma) and a side arm which serves as sample reservoir. The absorption of the optical cells has been calibrated prior to melting of the samples.

Results

Fig. A2.2 shows the absorption spectra of an InCl₂ melt. Spectra are characterised by a fundamental excitation, its absorption starting around 2.5 eV. As presented in Fig. A2.3, the absorption edge shifts to lower energies with increasing In concentration, which agrees with the results of Warren *et al* [Warren83]. However, no significant IVCT band around 2.1 eV is found within the experimental errors. On the other hand, a spectrum of InCl_{2.2} shows a very weak excitation around 2.1 eV as shown in the inset of Fig. A2.3. In this cell the black impurities are separated after the high temperature measurements. With increasing the amount of the impurities the background becomes higher and the peak more noticeable. It should be noted that Warren *et al*. performed the absorption measurement with quartz cells with the optical path length of 1-5 mm, so that the possibility of contamination may be higher.

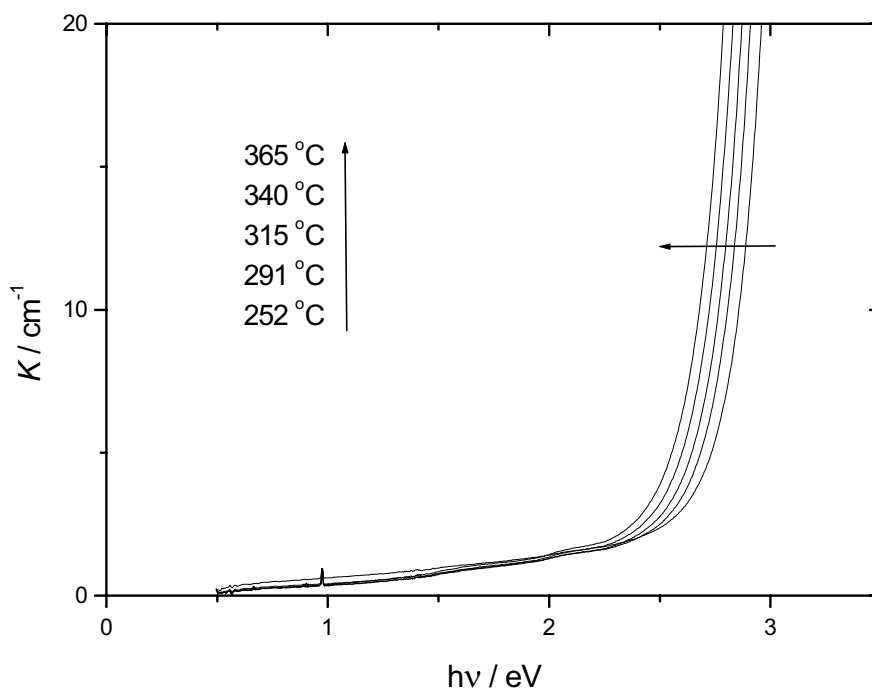


Fig. A2.2 Absorption spectra of InCl_2 melts. Temperature increases with the direction of arrow.

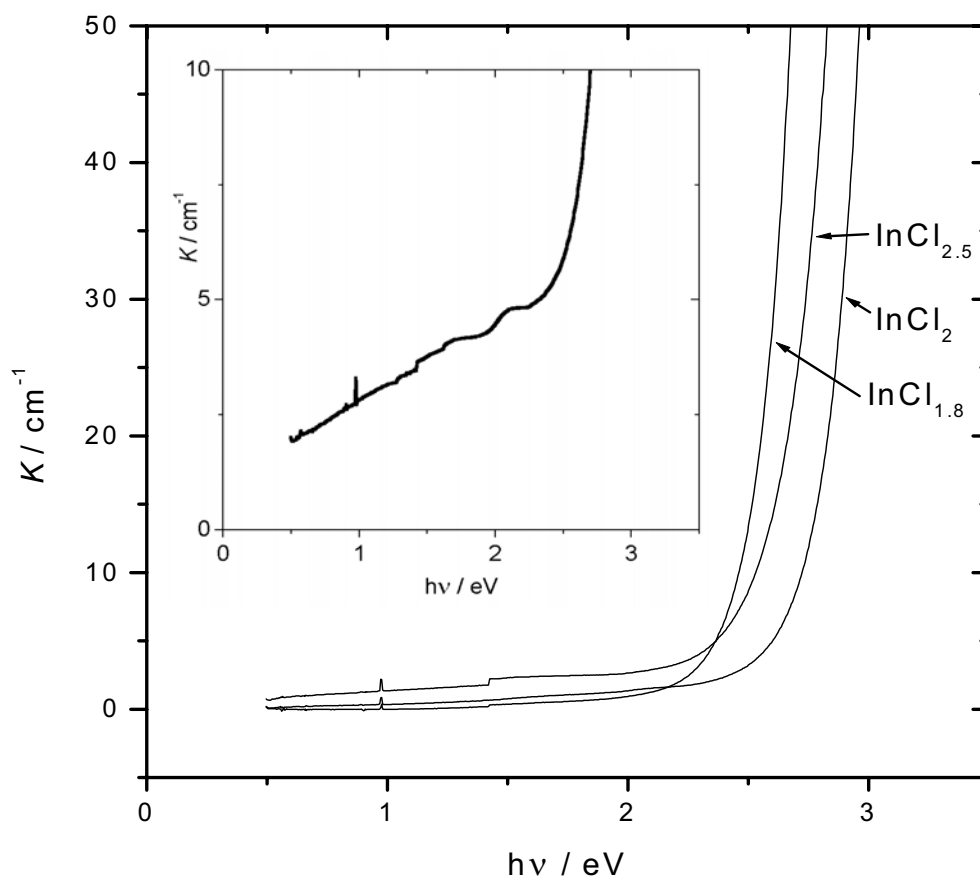


Fig. A2.3 Absorption spectra of InCl_x melts at 340 °C. Note that temperature is 445 °C for $\text{InCl}_{2.5}$ melt, so that the apparent absorption edge is lower than other samples. Inset: spectrum of $\text{InCl}_{2.2}$ melt containing impurities.

Table A2.1 Urbach parameters of InCl_x melts.

	$\text{InCl}_{1.8}$	InCl_2
K_0 / cm^{-1}	$(2.2 \pm 0.2) \times 10^8$	$(2.4 \pm 0.3) \times 10^7$
γ	0.36 ± 0.02	0.34 ± 0.02
E_0 / eV	4.8 ± 0.6	4.6 ± 0.6

In Table A2.1 the Urbach parameters are summarized. The difference of one order in K_0 may be due to the large optical path length (1 mm), leading to a large uncertainty. Moreover, the tendency of E_0 as a function of In composition is not specified through the fitting with Urbach formula (eqn. 6.1).

Manufacturer list

(Alfa) Alfa Chemikalien, Karlsruhe

(Aldrich) Aldrich Chemikalien, Steinheim

(AVIV) AVIV, Lakewood NJ, USA

(Braun) M.Braun GmbH, Garching

(Bruker) Bruker, Rheinstetten

(Carl Zeiss) Zeiss Oberkochen

(Deutsche Carbon) Deutsche Carbon AG, Frankfurt am Main

(Eurotherm) Eurotherm GmbH, Limburg

(Goodfellow) Goodfellow, Bad Nauheim

(Hellma) Hellma GmbH & Co. KG, Müllheim

(Hüttinger) Hüttinger, Freiburg

(Melles Griot) Melles Griot, Darmstadt

(Plansee) Metallwerke Plansee GmbH, Reute, Austria

(QGTH) Aachener Quarz-Glas Technologie Heinrich, Aachen

(TEW) Thyssen Edelstahlwerke AG, Krefeld

References

- [Ashcroft76] N.W. Ashcroft and N.D. Mermin, *Solid State Physics*, Saunders College Publishing, Philadelphia, (1976).
- [Atkin90] P.W. Atkins, *Molecular Quantum Mechanics*, Oxford University Press, Oxford, (1990).
- [Atherton93] N.M. Atherton, *Principles of Electron Magnetic Resonance*, Ellis Horwood, Chichester, (1993).
- [Ayscough67] P.B. Ayscough, *Electron Spin Resonance in Chemistry*, Methuen, London, (1967).
- [Bachtler89] M. Bachtler, *Diploma thesis*, University of Karlsruhe, (1989).
- [Bachtler94] M. Bachtler, J. Rockenberger, W. Freyland, Chr. Rosenkilde and T. Ostvold, *J. Phys. Chem.*, **98** (1994) 742.
- [Bachtler95] M. Bachtler, W. Freyland, G.A. Voyatzis and G. Papatheodorou, *Ber. Bunsenges. Phys. Chem.*, **99** (1995) 21.
- [Ballone84] P. Ballone, G. Pastore, and M.P. Tosi, *J. Chem. Phys.*, **81** (1984) 3174.
- [Beck76] H.P. Beck, *Z. Naturforsch.*, **B31** (1976) 1548.
- [Beck79] H.P. Beck and E. Gladrow, *Z. anorg. allg. Chem.*, **453** (1979) 79.
- [Beck92] H.P. Beck and M. Schuster, *J. Solid State Chem.*, **100** (1992) 301.
- [Blanckenhagen94] B. von Blanckenhagen, D. Nattland and W. Freyland, *J. Phys. Condens. Matter*, **6** (1994) L179.
- [Blanckenhagen97] B. von Blanckenhagen, *PhD Thesis*, University of Karlsruhe, (1997).
- [Bogacz99] A. Bogacz, L. Rycerz, S. Rumianowski, W. Szymanski and W. Szklarski, *High Temp. Material Processes*, **3** (1999) 461.
- [Boghosian96] S. Boghosian and G.N. Papatheodorou, in *Handbook on the Physics and Chemistry of Rare Earths* Vol. 23, ed. by K.A. Gschneider, Jr. and L. Eyring, Elsevier, (1996) p. 435.
- [Böttger85] H. Böttger and V.V. Bryksin, *Hopping Conduction in Solids*, VCH, Weinheim, (1985).
- [Bratsch82] S. Bratsch and H.B. Silber, *Rare Earths Mod. Sci. Technol.*, **3** (1982) 291.
- [Bredig64] M.A. Bredig, in *Molten Salt Chemistry*, ed. by M. Blander, Interscience, New York, (1964) p.367.
- [Burrow87] J.H. Burrow, C.H. Maule, P. Strange, J.N. Tothill and J.A. Wilson, *J. Phys. C: Solid State Phys.*, **20** (1987) 4115.
- [Carrington67] A. Carrington and A.D. McLachlan, *Introduction to magnetic resonance*, Harper and Row, New York, (1967).

- [Child83] W.C. Child, Jr. and G.N. Papatheodorou, *J. Phys. Chem.*, **87** (1983) 271.
- [Chrissanthopoulos00] A. Chrissanthopoulos and G.N. Papatheodorou, in *Progress in Molten Salt Chemistry I: Prof. N.J. Bjerrum Special Volume*, Elsevier, Paris, (2000) p. 167.
- [Corbett61] J.D. Corbett, L.F. Druding, W.J. Burkhard and C.B. Lindahl, *Discussions Faraday Soc.*, **32** (1961) 79.
- [Corbett67] J.D. Corbett, R.A. Sallach, and D.A. Lokken, *Adv. Chem. Ser.*, **71** (1967) 56.
- [Corbett83] J.D. Corbett, *Inorg. Synth.*, **22** (1983) 15.
- [Cordfunke01] E.H.P. Cordfunke and R.J.M. Konings, *Thermochim. Acta*, **375** (2001) 17.
- [Cox87] P.A. Cox, *The Electronic Structure and Chemistry of Solids*, Oxford University Press, Oxford, (1987).
- [CRC97] *CRC Handbook of Chemistry and Physics*, CRC Press, New York, (1997).
- [Demadis01] K.D. Demadis, C.M. Hartshorn and T.J. Meyer, *Chem. Rev.*, **101** (2001) 2655.
- [Diehl95] K. Diehl, *PhD thesis*, University of Karlsruhe, (1995).
- [Druding61] L.F. Druding and J.D. Corbett, *J. Am. Chem. Soc.*, **83** (1961) 2462.
- [Dworkin63] A.S. Dworkin, H.R. Bronstein and M.A. Bredig, *J. Phys. Chem.*, **67** (1963) 2715; A.S. Dworkin, R.A. Sallach, H.R. Bronstein, M.A. Bredig and J.D. Corbett, *ibid.*, **67** (1963) 1145.
- [Emin93] D. Emin, *Phys. Rev.*, **B48** (1993) 13691.
- [Ephraim] F. Ephraim and R. Bloch, *Chem. Ber.*, **59** (1926) 2692 and **61** (1928) 65.
- [Fowler68] W.B. Fowler, *Physics of Color Centers*, ed. W.B. Fowler, Academic Press, New York, (1968).
- [Freyland84] W. Freyland, K. Garbade, H. Heyer and E. Pfeiffer, *J. Phys. Chem.*, **88** (1984) 3745.
- [Freyland94] W. Freyland, *Z. Phys. Chem. NF*, **184** (1994) 139.
- [Freyland95] W. Freyland, in *Metal-Insulator Transitions Revisited*, ed. by P.P. Edwards and C.N.R. Rao, Taylor and Francis, London, (1995).
- [Fukushima96] K. Fukushima and Y. Iwodate, *J. Alloys Comp.*, **238** (1996) L1.
- [Gaune-Escard94] M. Gaune-Escard, A. Bogacz, L. Rycerz and W. Szczepaniak, *Thermochim. Acta*, **236** (1994) 67.
- [Gaune-Escard99] M. Gaune-Escard, Y. Koyama, R. Takagi, K. Fukushima and Y. Iwodate, *J. Mol. Liq.*, **83** (1999) 105.
- [Gmelin82] *Gmelin - Handbuch der Anorganischen Chemie, Seltenerdelemente*, System Nr. 39, Teil C4a (Chloride) (1982).

- [Grosse79] P. Grosse, *Freie Elektronen in Festkörpern*, Springer, Berlin, (1979).
- [Gruen65] D.M. Gruen, *Quart. Rev.*, **19** (1965) 349.
- [Gruen66] D.M. Gruen and C.W. Dekock, *J. Chem. Phys.*, **45** (1966) 455.
- [Haarberg88] G.M. Haarberg, K.S. Osen, J.J. Egan H. Heyer and W. Freyland, *Ber. Bunsenges. Phys. Chem.*, **92** (1988) 193.
- [Haire80] R.G. Haire, J.P. Young and J.Y. Bourges, in *The Rare Earths in Modern Science and Technology vol. 2*, ed by G.J. McCarthy, J.J. Rhyne and H.B. Silber, Plenum Press, New York, (1980).
- [Haschke79] J.M. Haschke, in *Handbook on the Physics and Chemistry of Rare Earths*, ed. by K.A. Gschneidner, Jr. and L. Eyring, North-Holland, (1979) p.89.
- [Haselhorst94] R.W. Haselhorst, *PhD thesis*, University of Karlsruhe, (1994).
- [Hayashi01] H. Hayashi (Japan Atomic Energy Research Institute), personal communication, (2001).
- [He95] T. He, *Phys. Rev.*, **B51** (1995) 16689.
- [Hecht87] E. Hecht, *Optics*, Addison-Wesley, Massachusetts, (1987).
- [Hensel90] F. Hensel, *J. Non-Cryst. Solids*, **117/118** (1990) 441.
- [Hermas99] A.A. Hermas, F. Endres, D. Nattland and W. Freyland, in *Wissenschaftliche Abschlussberichte 34. Internationales Seminar*, University of Karlsruhe, (1999) p. 23.
- [Hüfner78] S. Hüfner, *Optical Spectra of Transparent Rare Earth Compounds*, Academic Press, New York, (1978).
- [Hush67] N.S. Hush, *Prog. Inorg. Chem.*, **8** (1967) 391.
- [Hush85] N.S. Hush, *Coord. Chem. Rev.*, **64** (1985) 135.
- [Hutchinson99] F. Hutchinson, A.J. Rowley, M.K. Walter, M Wilson, P.A. Madden, J.C. Wasse and P.S. Salmon, *J. Chem. Phys.*, **111** (1999) 2028.
- [Ichikawa79] K. Ichikawa and W.W. Warren, Jr., *Phys. Rev.*, **B20** (1979) 900.
- [Ichikawa82] K. Ichikawa, *Prog. Theor. Phys. Suppl.(Kyoto)*, **72** (1982) 156.
- [Iizuka97] M. Iizuka, T. Koyama, N. Kondo, R. Fujita and H. Tanaka, *J. Nucl. Mater.*, **247** (1997) 183.
- [Iwadate81] Y. Iwadate, J. Mochinaga and K. Kawamura, *J. Phys. Chem.*, **85** (1981) 3708.
- [Iwadate95] Y. Iwadate, N. Okako, Y. Koyama, H. Kubo and K. Fukushima, *J. Mol. Liq.*, **65-66** (1995) 369 and references therein.
- [Iwadate98] Y. Iwadate, *Molten Salt and High Temp. Chem. (Tokyo)*, **41** (1998) 113 (in Japanese).

- [Janz67] G.J. Janz, *Molten Salt Handbook*, Academic Press, New York, (1967).
- [Janz77] G.J. Janz, R.P.T. Tomkins, C.B. Allen, J.R. Downey, Jr. and S.K. Singer, *J. Phys. Chem. Ref. Data*, **6** (1977) 409.
- [John88] S. John, M.Y. Chou, M.H. Cohen and C.M. Soukoulis, *Phys. Rev.*, **B37** (1988) 6963.
- [Johnson69a] K.E. Johnson and J.N. Sandoe, *J. Chem. Soc. A*, (1969) 1694.
- [Johnson69b] D.A. Johnson, *J. Chem. Soc. A*, (1969) 2578.
- [Jørgensen64] C.K. Jørgensen, R. Pappalardo and E. Rittershaus, *Z. Naturforsch.*, **19a** (1964) 424.
- [Jörger98] M. Jörger, *Diploma thesis*, University of Karlsruhe (1998).
- [Jortner99] *Electron Transfer – From Isolated Molecules to Biomolecules*, ed. by J. Jortner and M. Bixon, *Adv. Chem. Phys.*, **106** and **107**, (1999).
- [Judd62] B.R. Judd, *Phys. Rev.*, **127** (1962) 750.
- [Jungmann95] A. Jungmann, *PhD Thesis*, University of Saarland, (1995).
- [Kamenskaya83] A.N. Kamenskaya, N.B. Mikcheev and N.P. Kholmogorova, *Russ. J. Inorg. Chem.*, **28** (1983) 1420.
- [Keller76] B. Keller, K. Bukietyńska and B. Jeżowska-Trzebiatowska, *Bull. Acad. Pol. Sci. Serie Sci. Chim.*, **14** (1976) 763.
- [Kim79] Y.-C. Kim and J. Oishi, *J. Less-Common Met.*, **65** (1979) 199.
- [Kittel88] C. Kittel, *Introduction to Solid State Physics* 6th Ed., John Wiley & Sons, Inc., New York, (1988).
- [Koslowski96] T. Koslowski, *Ber. Bunsenges. Phys. Chem.*, **100** (1996) 95.
- [Koslowski97] T. Koslowski, *J. Chem. Phys.*, **106** (1997) 7241.
- [Koyama97] Y. Koyama, R. Takagi, Y. Iwadate and K. Fukushima, *J. Alloys. Comp.*, **260** (1997) 75.
- [Kudinov69] E.K. Kudinov, D.H. Mirlin and Yu.A. Firsov, *Fis. Tverd. Tela*, **11** (1969) 2789., *Sov. Phys. Solid State*, **11** (1970) 2257.
- [Kutscher74] J. Kutscher and A. Schneider, *Z. anorg. allg. Chem.*, **408** (1974) 121.
- [Kuznetsov99] A.M. Kuznetsov and J. Ulstrup, *Electron Transfer in Chemistry and Biology: an introduction to the theory*, Wiley, New York, (1999).
- [Kvam98] K.R. Kvam, D. Bratland and H. A. Øye, in *Proceedings of the international Terje Østvold Symposium*, (1998), p.97.
- [Lange92] F.T. Lange, *PhD thesis*, University of Karlsruhe, (1992).

- [Laptev86] D.M. Laptev, T.V. Kiseleva, N.M. Kulagin, V.F. Goryushkin and E.S. Voronkov, *Russ. J. Inorg. Chem.*, **31** (1986) 84.
- [Launay01] J.-P. Launay, *Chem. Soc. Rev.*, **30** (2001) 386.
- [Logan92] D.E. Logan and F. Siringo, *J. Phys. Condens. Matter*, **4** (1992) 3695.
- [Madden00] P.A. Madden and M. Wilson, *J. Phys. Condens. Matter*, **12** (2000) A95.
- [Mallitson62] I.M. Mallitson, *J. Opt. Soc. Am.*, **52** (1962) 1377.
- [Marcus77] Y. Marcus, *Introduction to Liquid State Chemistry*, John Wiley, London, (1977).
- [McClure63] D.S. McClure and Z. Kiss, *J. Chem. Phys.*, **39** (1963) 3251.
- [McConnell56] H.M. McConnell, *J. Chem. Phys.*, **25** (1956) 709.
- [Mellors59] G.W. Mellors and S. Senderoff, *J. Phys. Chem.*, **63** (1959) 1110.
- [Meyer83] G. Meyer and R. Blachnik, *Z. anorg. allg. Chem.*, **503** (1983) 126.
- [Meyer88] G. Meyer, *Chem. Rev.*, **88** (1988) 93.
- [Micklitz85] H. Micklitz, in *Localization and Metal-Insulator Transition: N.F. Mott Festschrift*, Vol. 3, ed. by H. Fritzsche and D. Adler, Plenum Press, New York and London, p.89. Citation from [Mott90].
- [Misra93] S.N. Misra and K. John, *Appl. Spectrosc. Rev.*, **28** (1993) 285.
- [Mochinaga78] J. Mochinaga, K. Igarashi, T. Aoki and Y. Iwadate, *Bull. Chem. Soc. Jpn.*, **51** (1978) 3107.
- [Mott71] N.F. Mott and E.A. Davis, *Electronic Processes in Non-crystalline Materials*, Clarendon Press, Oxford, (1971).
- [Mott90] N.F. Mott, *Metal Insulator Transitions*, Taylor and Francis, London, (1990).
- [Nakamura97] K. Nakamura and M. Kurata, *J. Nucl. Mat.*, **247** (1997) 309.
- [Nakowsky84] B. Nakowsky, N. Nicoloso and W. Freyland, *Ber. Bunsenges. Phys. Chem.*, **88** (1984) 297.
- [Nattland86] D. Nattland, H. Heyer and W. Freyland, *Z. Phys. Chem. NF*, **149** (1986) 1.
- [Nattland93] D. Nattland, T. Rauch and W. Freyland, *J. Chem. Phys.*, **98** (1993) 4429.
- [Nattland95] D. Nattland, *Habilitationsschrift*, University of Karlsruhe, (1995).
- [Ofelt62] G.S. Ofelt, *J. Chem. Phys.*, **37** (1962) 511.
- [Oppermann00] H. Oppermann and C. Hennig, *Z. anorg. allg. Chem.*, **626** (2000) 450.
- [Palik85] *Handbook of Optical Constants of Solids*, ed. by E.D. Palik, Academic Press, New York, (1985).

- [Papatheodorou00] G.N. Papatheodorou, in *Progress in Molten Salt Chemistry 1*, ed. by R.W. Berg and H.A. Hjuler, Elsevier, Paris, (2000) p. 65.
- [Photiadis98] G.M. Photiadis, B. Borresen and G.N. Papatheodorou, *J. Chem. Soc. Faraday Trans.*, **94** (1998) 2605 and references therein.
- [Poh01] P.D. Poh, *PhD Thesis*, University of Karlsruhe, (2001).
- [Potapov98] A.M. Potapov and O. Terakado, unpublished work, (1998).
- [Potapov00] A.M. Potapov and A.B. Salyulev, in *Progress in Molten Salt Chemistry 1*, ed. by R.W. Berg and H.A. Hjuler, Elsevier, Paris, (2000) p. 429.
- [Press89] W.H. Press, B.P. Flannery, S.A. Teukolsky and W.T. Vetterling, *Numerical recipes, the art of scientific computing*, Cambridge University Press, Cambridge, (1989).
- [Robin67] M.B. Robin and P. Day, *Adv. Inorg. Chem. Radiochem.*, **10** (1967) 247.
- [Rodriguez B. 00] V.M. Rodriguez B., personal communication, (2000).
- [Rodriugez B. 01] V.M. Rodriugez B., unpublished work, (2001).
- [Rodriugez B. 02] V.M. Rodriugez B., *PhD thesis*, University of Karlsruhe, (2002).
- [Ryan66] J.D. Ryan and C.K. Jørgensen, *J. Phys. Chem.*, **70** (1966) 2845.
- [Rycerz02] L. Rycerz and M. Gaune-Escard, *Z.Naturforsch.*, (2002) in preparation.
- [Schindelbeck95] T. Schindelbeck, *PhD Thesis*, University of Karlsruhe, (1995).
- [Schindelbeck96] T. Schindelbeck and W. Freyland, *J. Chem. Phys.*, **105** (1996) 4448.
- [Schmitt77] W. Schmitt and U. Schindewolf, *Ber. Bunsenges. Phys. Chem.*, **81** (1977) 584.
- [Selloni87] A. Selloni, P. Carnevali, R. Car and M. Parrinello, *Phys. Rev. Lett.*, **59** (1987) 823.
- [Senatore80] G. Senatore, Parrinello and M.P. Tosi, *Philos. Mag.*, **52** (1980) 173.
- [Senatore84] G. Senatore, M.P. Tosi and T.O. Woodruff, *Solid State Commun.*, **52** (1984) 173.
- [Silvestrelli96] P. Silvestrelli, A. Alavi, M. Parrinello and D. Frenkel, *Phys. Rev.*, **B53** (1996) 12750.
- [Sinha66a] S.P. Sinha, *Complexes of the rare earths*, Pergamon Press, London, (1966).
- [Sinha66b] S.P. Sinha, *Spectrochim. Acta*, **22** (1966) 57.
- [Slichter90] C.P. Slichter, *Principles of Magnetic Resonance*, Springer, Heidelberg, (1990).
- [Smirnov82] M.V. Smirnov and V.P. Stepanov, *Electrochim. Acta*, **27** (1982) 1551.

- [Smith64] P. Smith, in *Molten Salt Chemistry*, ed. by M. Blander, Wiley, New York, (1964) p.427.
- [Sopra] Database of optical constants, SOPRA sa, Bois-Colombes, France, Available in internet under <http://www.sopra-sa.com>
- [Stöhr97] U. Stöhr, *PhD Thesis*, University of Karlsruhe, (1997).
- [Stöhr98] U. Stöhr, P.R. Bandi, F. Matthiesen and W. Freyland, *Electrochim. Acta*, **43** (1998) 569.
- [Stöhr99] U. Stöhr and W. Freyland, *Phys. Chem. Chem. Phys.*, **1** (1999) 4383.
- [Stöwe97] K. Stöwe, S. Tratzky, H.P. Beck, A. Jungmann, R. Classen, R. Zimmermann, G. Meng, P. Steiner and S. Hüfner, *J. Alloys Compounds.*, **246** (1997) 101.
- [Struck91] C.W. Struck and J.A. Baglio, *High Temp. Sci.*, **31** (1991) 1 and 209.
- [Tatlipinar92] H. Tatlipinar, Z. Akdeniz, G. Pastore and M.P. Tosi, *J. Phys. Condens. Matter*, **4** (1992) 8933.
- [Thompson76] J.C. Thompson, *Electrons in Liquid Ammonia*, Clarendon, (1976).
- [Warren83] W.W. Warren, Jr., G. Schönherr and F. Hensel, *Chem. Phys. Lett.*, **96** (1983) 505.
- [Warren84] W.W. Warren, Jr., S. Sotier and G.F. Brennert, *Phys. Rev.*, **B30** (1984) 65.
- [Warren85] W.W. Warren, Jr., in *The Metallic and Nonmetallic State of Matters*, ed. by P.P. Edwards and C.N.R. Rao, Taylor and Francis, London, (1985).
- [Wasse98] J.C. Wasse and P.S. Salmon, *Physica B*, **241-243** (1999) 967.
- [Wasse99] J.C. Wasse and P.S. Salmon, *J. Phys. Condens. Matter*, **11** (1999) 1381 and 9293.
- [Wooten72] F. Wooten, *Optical Properties of Solids*, Academic Press, London, (1972).
- [Xie93] G. Xie, K. Ema, Y. Ito and Z.M. Shou, *J. Appl. Electrochem.*, **23** (1993) 753.
- [Yamamura98] Y. Yamamura, I. Wu, H. Zhu, M. Endo, N. Akao, M. Mohamedi and Y. Sato, *Molten Salt Chem. Technol.*, **5** (1998) 355.
- [Zein El Abedin00] S. Zein El Abedin, personal communication, (2000).
- [Zein El Abedin02] S. Zein El Abedin, O. Terakado, F. Endres, D. Natland and W. Freyland, *Phys. Chem. Chem. Phys.*, (2002) in press.

Lebenslauf

Zur Person

Name	Osamu Terakado
Geburtsdatum	25.11.1973
Geburtsort	Ibaraki, Japan
Familienstand	ledig

Schulbildung

Elementary school	1980-1986, Hatori, Fujisawa
Junior high school	1986-1989, Hatori, Fujisawa
High school	1989-1992, Shonan, Kanagawa

Hochschulausbildung

Hokkaido University	1992-1996
Department of Chemistry	March 1996 Bachelor
Faculty of Science	Thema: „Low-field ESR study of Metal - Nonmetal transitions of Na-NH ₃ solutions“
Lab. Prof. Dr. Y. Nakamura	

Hokkaido University	1996-1998
Division of Chemistry	March 1998 Master of Science
Graduate school of Science	Thema: „Metal-Nonmetal Transitions of Metal - Ammonia (amine) solutions“
Lab. Prof. Dr. Y. Nakamura	

Dissertation

Universität Karlsruhe (TH), Institut für Physikalische Chemie Lehrstuhl Prof. Dr. W. Freyland	April 1998 bis Juli 2002 verbunden mit einer Tätigkeit als wissenschaftlicher Mitarbeiter
---	---

Abschließend möchte ich allen danken, die zum Gelingen dieser Arbeit beitragen haben:

Herrn Prof. Dr. W. Freyland für die interessante Themenstellung, seine ständige Diskussionsbereitschaft und daily lecture on „sophiscated German“,

Herrn Prof. Dr. M. Kappes für die freundliche Übernahme des Korreferats,

Herrn PD Dr. D. Nattland für die Einführung in das Arbeitsgebiet und die hervorragende Zusammenarbeit mit vielen Tricks sowie eine Vielzahl von Deutschunterricht,

Herrn Dr. P. Poh für die professionelle Einweisung in die spezielle ESR Anlage,

Herrn D. Waltz und Herrn W. Baltz, sowie allen Mitgliedern der Institutswerkstatt, ohne deren Hilfe, Rat und Unterstützung diese Arbeit nicht hätte realisiert werden können.

Herrn H. Ernesti ebenfalls für sehr schnelle und präzise feinmechanische Arbeiten sowie monatliche Fahrradreparatur,

Herrn Glasbläsermeister G. Rotter für die Geduld beim Anfertigen zahlreicher Quarz- und Glasarbeit,

Herrn S. Szepessy für die Hilfe der Rechner- und Softwareprobleme,

Frau G. Ritter für die Unterstützung beim Vorbereiten der Messungen sowie die Urlaubtipps (Schwerpunkt: Schweiz),

allen Mitgliedern der Arbeitsgruppe für das gute Arbeitsklima,

den mit Seltenerdmetallhalogenid Schmelzen arbeitenden internationalen visiting scientists für die Betreuung eines oft depressiven Japaners,

dem Stockwerksraucherkamerad Herrn M.Sc. A. Ayyad für seine stete Diskussionsbereitschaft über die Alltagsprobleme eines Doktoranden.